Lawrence Berkeley National Laboratory
Recent Work

Title
Production of low axial energy spread ion beams with multicusp sources

Permalink
https://escholarship.org/uc/item/5z8795ds

Author
Lee, Yung-Hee Yvette

Publication Date
1998-05-01

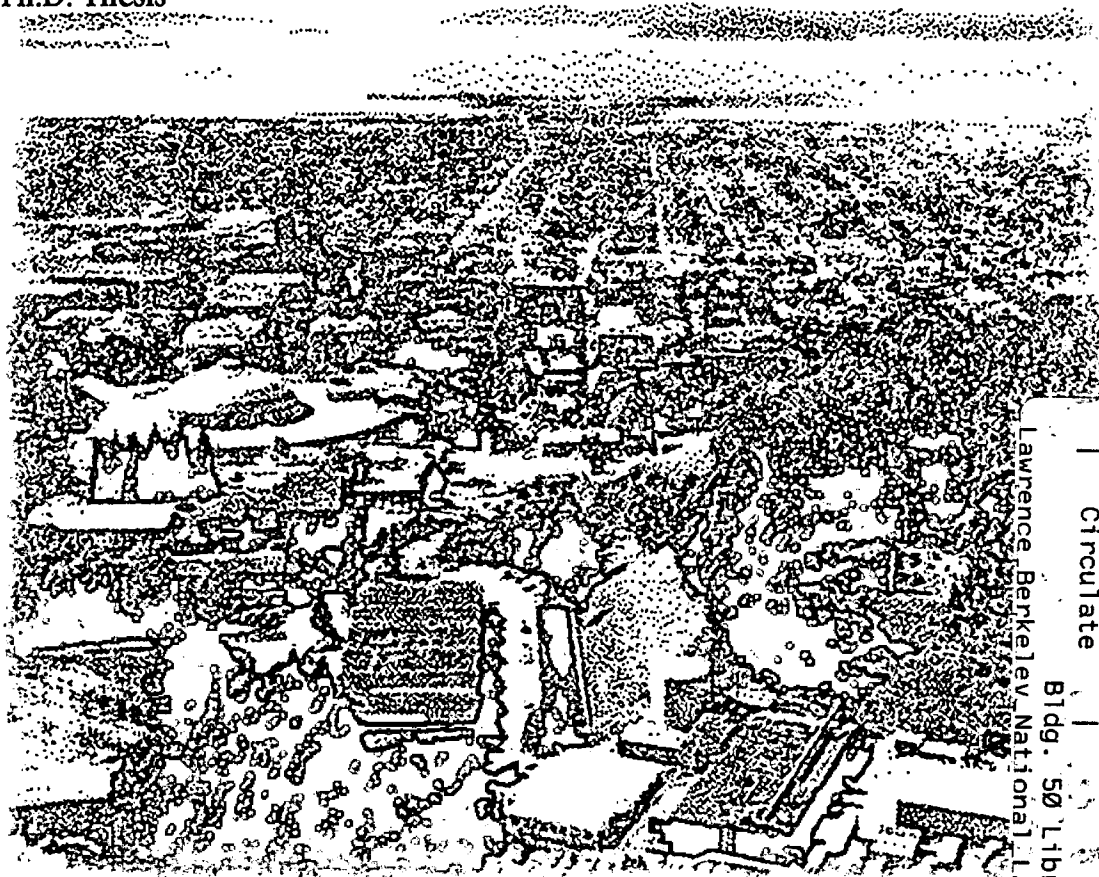# ERNEST ORLANDO LAWRENCE
BERKELEY NATIONAL LABORATORY

Production of Low Axial Energy Spread Ion Beams with Multicusp Sources

Yung-Hee Y. Lee

Accelerator and Fusion Research Division

May 1998

Ph.D. Thesis

DISCLAIMER

Production of Low Axial Energy Spread Ion Beams with Multicusp Sources

by

Yung-Hee Yvette Lee

B.S. (University of California, Berkeley) 1994

M.S. (University of California, Berkeley) 1996

A dissertation submitted in partial satisfaction of the

requirements for the degree of

Doctor of Philosophy

in

Engineering

Nuclear Engineering

in the

GRADUATE DIVISION

of the

UNIVERSITY OF CALIFORNIA, BERKELEY

Committee in charge:

Professor Jasmina Vujic, Chair

Professor Wulf B. Kunkel

Dr. Ka-Ngo Leung

Professor Edward C. Morse

1998

Abstract

Production of Low Axial Energy Spread Ion Beams with Multicusp Sources

by

Yung-Hee Yvette Lee

Doctor of Philosophy in Nuclear Engineering

University of California, Berkeley

Professor Jasmina Vujic, Chair

Multicusp ion sources are capable of producing ions with low axial energy spread which are necessary in applications such as: ion projection lithography (IPL) and focused ion beams for the next generation lithographic tools and nuclear science experiments such as radioactive ion beam production.

The axial ion energy spread for multicusp source is approximately 6 eV which is too large for IPL and radioactive ion beam applications. The addition of a magnetic filter which consists of a pair of permanent magnets to the multicusp source reduces the energy spread considerably. The reduction is due to the improvement in the uniformity of the axial plasma potential distribution in the discharge region.
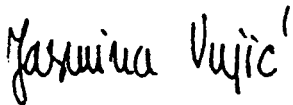
Axial ion energy spread of the filament driven ion source has been measured using three different techniques. In all cases, it was found to be less than 2 eV. Energy spread of the radio frequency (RF) driven source has also been explored, and it was found to be less than 3 eV with the proper RF-shielding.

A new multicusp source configuration has been designed and constructed to further reduce the energy spread. To achieve a more uniform axial plasma potential

distribution, a cylindrical magnetic filter has been designed and constructed for a 20-cm-diameter source.

This new source configuration, the co-axial source, is new in its kind. The energy spread in this source has been measured to be a record low of 0.6 eV. Because of the novelty of this device, some plasma parameters inside the source have been studied. Langmuir probe has been used to measure the plasma potential, the electron temperature and the density distribution.

Unlike any other source in existence, the co-axial source has been designed to have a capability in adjusting the radial plasma potential distribution and therefore the transverse ion temperature (or beam emittance). The effect on the beam emittance has been verified by using a triode accelerator assembly and a Allison type parallel-plate emittance scanner.

Jasmina Vujic

Prof. Jasmina Vujic, Chair
Nuclear Engineering Department
University of California, Berkeley

TABLE OF CONTENTS

LIST OF FIGURES

ACKNOWLEGMENTS

I want to thank all the people who helped me throughout the years. Most thanks to my parents whose constant support and understanding allowed me to stay on with my plans, even though they changed constantly.

To Dr. Ka-Ngo Leung, thanks for sharing your expertise on ion sources with me. Your guidance and the teachings will be the basis of my career as an ion sorceress.

To Professor Jasmina Vujic who has always been my role-model.

To Professor Wulf Kunkel for all the suggestions on experiments and papers.

To Professor Edward Morse for accepting to read my dissertation and teaching the plasma courses which have helped me in many, many ways.

To Lee Sun, for coming to my rescue when I had problems with the computers and the system. Thanks, the system worked, and this dissertation proves it.

To Dan Pickard, I appreciate your helpful suggestions on experiments as well as your thoughts about the future.

To Rodrich Keller, thank you for always taking time to help us, students. Your helpful suggestions made our jobs easier. I hope some day I will be as good in ion transport systems as you.

To Nastaran Zahir, Qing Ji, Faye Yang and Vinh-Van Ngo for helping me get such good results on experiments.

To Don Williams, I thank you for being so good in what you do. You are always an important part of the IBT group.

To Daniela Wutte and Mattheaus Leitner, thanks.

To Steve Wilde, for being so good in making ion source and accelerator parts. Although, I was usually the lowest in priority, you always managed to finish it before it was too late. Also to Larry Mills, thanks.

To Tom McVeigh, Mark Rickard and Pete Rosado, for helping me find the so coveted power supplies to run my experiments.

To Luke Perkins, thanks for your help and suggestions.

To Margit Sarstead, thanks for accepting to train me even though I knew nothing about anything at the beginning.

To the members of the Ion Beam Technology Program, the head of the program Rick Gough, the AFRD and the rest of the members of Plasma and Ion Source Technology Group past and present, I owe you my sincere thanks.

CHAPTER 1

MULTICUSP ION SOURCES

1.1   INTRODUCTION

An ion source is a plasma generator from which beams of ions can be extracted. One type of ion source used in many applications is the multicusp ion source, named this way for the arrangement of the magnets that form magnetic cusp fields to contain the plasma.[1] The multicusp source is capable of producing large volumes of uniform, quiescent and high density plasmas with high gas and electrical efficiencies. They are now being used in neutral beam injectors for fusion devices, particle accelerators, ion implantation systems, neutron tubes for oil well logging and proton therapy machines. The same kind of source can also be used for the accelerator-based boron neutron capture therapy (BNCT) projects.

The multicusp ion source vary in size according to the need of the application. It can be as small as 2.5 cm in diameter to as large as 100 cm. The small size sources are used for applications such as neutron tube, while the larger sources can be used for other applications such as ion doping in large flat panel manufacturing processes.

The source is surrounded by columns of permanent magnets. The magnets are placed around the cylindrical wall as well the end flange since in most cases an extraction system has to be placed on the open end. Such magnet placement results in an asymmetric

distribution of the plasma potential inside the source which is crucial in understanding the axial or longitudinal energy spread.

The multicusp source can provide a low longitudinal or axial energy spread which is required in many applications. This is especially true when ion beams must be transported, manipulated, analyzed and applied in very low energy applications.[2] For instance, in Ion Projection Lithography (IPL), projection of sub-0.13 μm patterns from a stencil mask onto a wafer substrate is required for semiconductor fabrications. In order to maintain the chromatic aberrations below 25 nm, an ion source which delivers a beam with an energy spread of less than 3 eV is required.[3]

In the production of radioactive ion beams for nuclear physics experiments, an ion source with axial energy spread less than 1 eV is needed to perform isobaric separation with a magnetic deflection spectrometer.[4] In low energy (<100 eV) ion beam deposition processes, very low energy spread is required to separate and focus the ions properly.[5]

Low energy (<500 eV) mass spectrometers have been proposed for analyzing nuclear and chemical wastes. In order to achieve good mass resolution, an ion source that has low longitudinal energy spread is needed. Low axial ion energy spread is needed for time-of-flight experiments where the dense packet of deuterium ions impinging on the tritium target produces a short burst of neutrons by the D-T reaction which has a width less than a few ns.[6]

In this dissertation, the axial ion energy spread of the multicusp ion source is analyzed. Different methods of reducing the energy spread have been examined. It is demonstrated that energy spread lower than 2 eV can be achieved with a magnetic filter arrangement. Further ion source development has led to less than 1 eV energy spreads.

The design, construction and characterization of this new generation of sub-eV energy spread ion sources are described in this dissertation.

1.2   GENERAL CONFIGURATION

The ions and electrons in a plasma are charged particles in motion and experience an interaction with a magnetic field. The ions and electrons move in orbits around the magnetic field lines and, apart from collisions with other plasma particles, act as though they are tied to the field lines. The behavior of a plasma in a magnetic field can be profoundly different from a plasma in the absence of a magnetic field.

The fact that the ions and electrons can change the direction of their motion in the presence of a magnetic field provides a means of confining the plasma, at least in the direction transverse to the field. Plasma loss along the field can be reduced by increasing the field strength at the ends of the confinement region. The multicusp ion source uses this principle to successfully generate and confine the plasma.

Multicusp ion sources use permanent-magnets to confine the primary ionizing electrons and the plasma. The magnets are arranged in such a way as to generate line-cusp magnetic fields, as shown in Fig. 1.1 The magnetic field strength B is a maximum near the magnets and decays with distance into the chamber. Most of the plasma volume can be virtually magnetic-field free, while a strong field can exist near the discharge chamber wall, inhibiting plasma loss and leading to an increase in plasma density and uniformity.
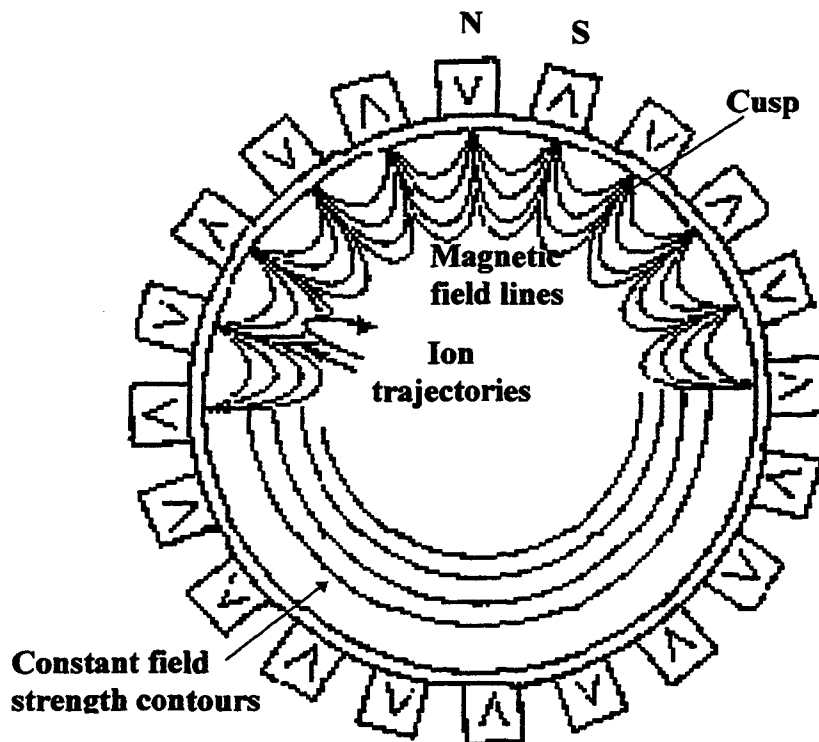
FIGURE 1.1 Magnetic multicusp confinement in cylindrical geometry, illustrating the magnetic field lines and the constant **B** surfaces near the circumferential walls.

Multicusp fields have been found to have three important effects on low-pressure plasma discharges:

1. High energy electrons can be efficiently confined. These electrons can be the ionization source for a discharge.

2. Significant improvements can be obtained in the confinement of the bulk plasma in a discharge.

3. Significant improvements in radial plasma density and potential uniformity can be achieved.

Plasma can be generated in a multicusp ion source by dc discharge or rf induction discharge. The surface magnetic field generated by rows of permanent magnets, typically of samarium-cobalt, can confine the primary ionizing electrons very efficiently. As a

result, the ionization efficiency of this type of plasma generator is high. A more detailed

explanation of these two different types of discharges is presented in the following

chapters.

A schematic diagram of a filament discharge multicusp source is shown in Fig.

1.2. The permanent magnets can be arranged in rows parallel to the beam axis.

Alternatively, they can be arranged in the form of rings perpendicular to the beam axis.

The back plate also contains rows of the same permanent magnets.
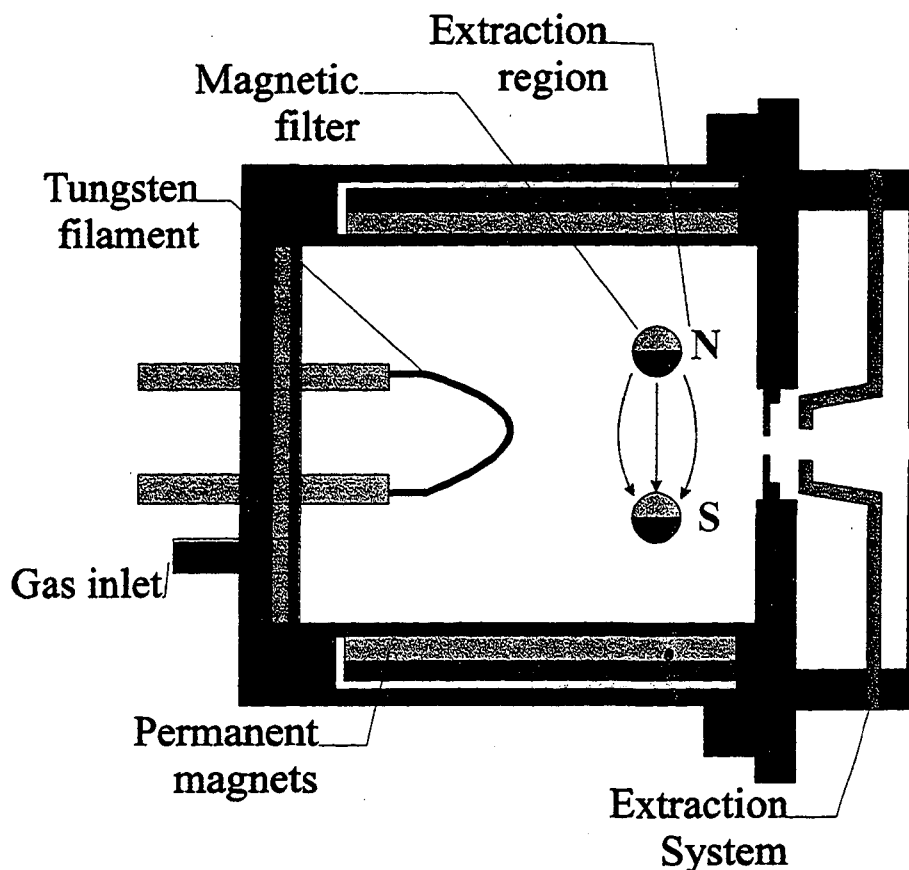
FIGURE 1.2 Multicusp ion source for dc discharge (hot tungsten
filament cathode) operation. It also shows the magnetic
filters installed in the source.

The open end of the source chamber is closed by a set of extraction electrodes. The source can be operated with the first electrode electrically floating or connected to the negative terminal of the cathode. The plasma density in the source, and therefore the extracted beam current depends on the magnet geometry, the discharge voltage and current, the biasing voltage on the first extraction electrode, and the size of the source chamber.

The multicusp source is generally used to produce positive or negative hydrogen/deuterium ion beams for particle accelerators and for neutral beam heating of tokamak plasmas. It can also be used to generate positive ion beams of the inert gases, He, Ne, Ar, Kr, and Xe.

A permanent-magnet "filter" shown schematically in Fig. 1.2 can be installed in a multicusp ion source. The filter improves the atomic hydrogen or nitrogen ion fraction, the source operability, the plasma density profile at the extraction plane, and the uniformity of the plasma potential along the axis. Atomic ion species >90% can be obtained for the diatomic gases such as hydrogen and nitrogen by the use of the magnetic filter.[7]

This filter, generated either by inserting small magnets into the source chamber or by installing a pair of dipole magnets on the external surface of the source chamber, provides a narrow region of transverse B-field that is strong enough to prevent the energetic ionizing electrons from reaching the extraction region, but is weak enough to allow the plasma to leak through. The absence of energetic electrons will prevent the formation of molecular ions in the extraction region, but dissociation of the molecular ions can still occur. As a result, the atomic ion species percentage in the extracted beam is enhanced.

Recently, it is demonstrated that the filter can also be used to improve the axial energy spread of the ions generated in a multicusp source.[8] The following chapters of this dissertation describe the principle and the development of the ion source configuration and magnetic-filter for the production of low axial energy spread ion beams.

CHAPTER 2

APPLICATIONS OF LOW AXIAL ENERGY SPREAD SOURCES

The plasma particles have kinetic energy of motion. The energy distribution of the particles can be measured by recording the ion distribution in terms of ion current versus voltage. The V-I characteristic curve is differentiated to obtain the Full Width at Half Maxima (FWHM) or axial energy spread. The axial energy spread of ions is defined in detailed in Chapter 3 of this dissertation.

Ion beams with low axial energy spread are required in quite a number of applications for different reasons. For instance, in lithography and nanotechnology applications, low axial energy spread ions are needed to minimize the chromatic aberration; in the production of radioactive ion beams for nuclear physics experiments, an ion source with axial energy spread less than 1 eV is needed to perform isobaric separation with a magnetic deflection spectrometer. A brief description of these applications is presented in this chapter.

2.1 NANOTECHNOLOGY APPLICATIONS

Optical lithography has been the technology of the semiconductor industry for more than 30 years. This technology is expected to take the semiconductor feature sizes down to 0.18 micron and less in the future. To achieve smaller feature sizes, the semiconductor industry will need other imaging technologies.

The lithography equipment market is at present dominated by foreign firms. To establish themselves as market leaders for lithography equipment for the next generation and beyond, U.S. companies have to dominate in the post-deep UV lithography technologies.

In order to meet the needs of the industry, research on new imaging technologies is under way in several laboratories around the world. The technologies include X-ray Lithography, Extreme Ultraviolet Lithography, Electron Beam Lithography, and Ion Beam Lithography. A preferred technology area may not emerge until late 1999.

Each of these alternative technologies, however, needs several common technologies that will support future semiconductor lithography. These include mask technologies, resist technologies, optical element fabrication technologies, metrology, alignment systems, safety, etc.

The remarkable progress in the miniaturization of electronic devices over the past four decades promises to continue for many years. At the heart of this revolution is the silicon integrated circuit (IC) whose complexity and performance continue to increase, paving the way for continuous innovation in solid-state devices. The improvements in IC performance stem primarily from an ability to internally interconnect more and more active components on a single chip of silicon.[9] In 1965, 250 devices could be interconnected in the "monolithic integrated circuit", in 1983 more than 1,000,000 devices were routinely connected in a single device, and in 1993, 256,000,000 interconnection devices are common. This improvement has come about largely through a decrease in the size of the circuit elements. The size of the chips has increased slowly over the years, whereas the size of each element decreased from >20µm in 1963 to <2.0µm in 1983, 0.5µm in 1993,

<2.0µm in 1983, 0.5µm in 1993, and continues to decrease. Sophisticated technologies are being developed to accommodate these small features. In some of these techniques, multicusp ion sources are being used because of the low axial energy spread ions.

2.1.1 PROJECTION LITHOGRAPHY PRINTING
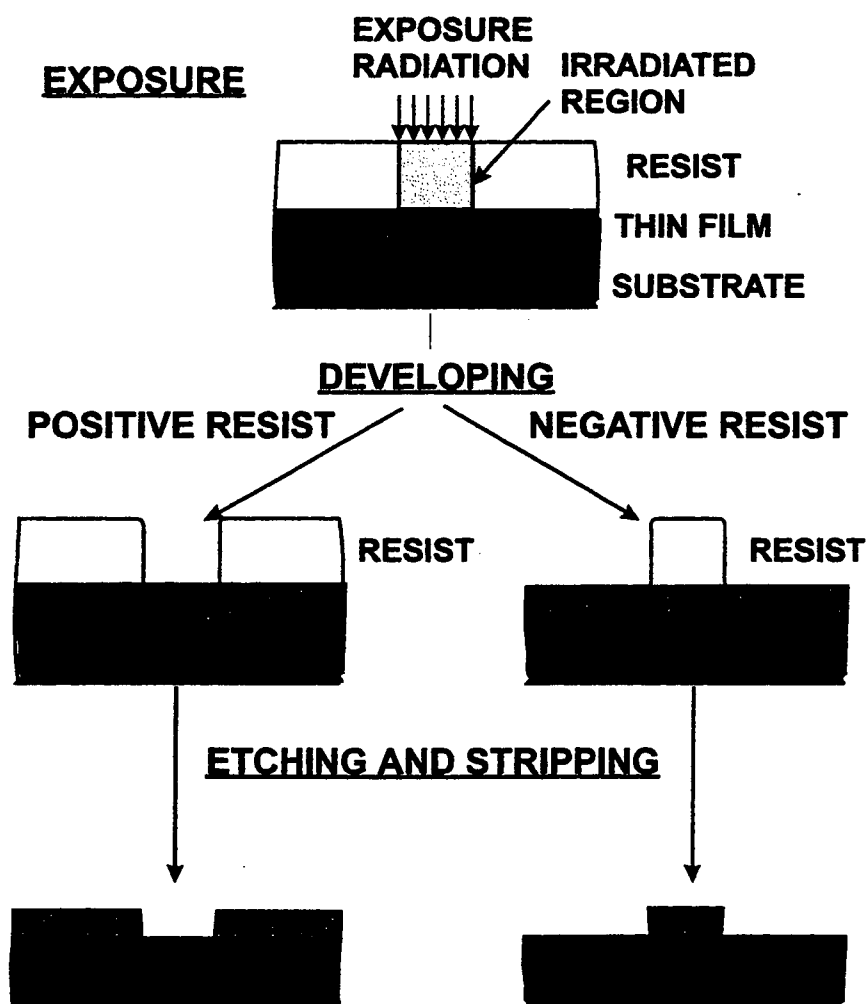
FIGURE 2.1 Diagram showing the formation of a polymeric relief image by lithography. The resist pattern is used to subsequently modify the underlying substrate.

The fabrication of an integrated circuit requires a technique that enables the

various thin-film materials used to build up the device on a semiconductor substrate to be

patterned. That technique is the lithographic process.

The goal of the lithographic process is the accurate and precise definition of three-

dimensional patterns on the semiconductor substrate. The lithographic process involves

transferring a circuit pattern into a polymer film (termed a resist) and subsequently

replicating that pattern in an underlying thin conductor or dielectric film. This process is

shown in Fig. 2.1.

The flexibility and effectiveness of ions in modifying the properties of solids make

them attractive tools for lithography. A focused beam of ions can be formed and deflected

in much the same way as an electron beam and can be used in a wide range of

applications, including lithography, (Fig. 2.2a), ion implantation and ion milling.[10]
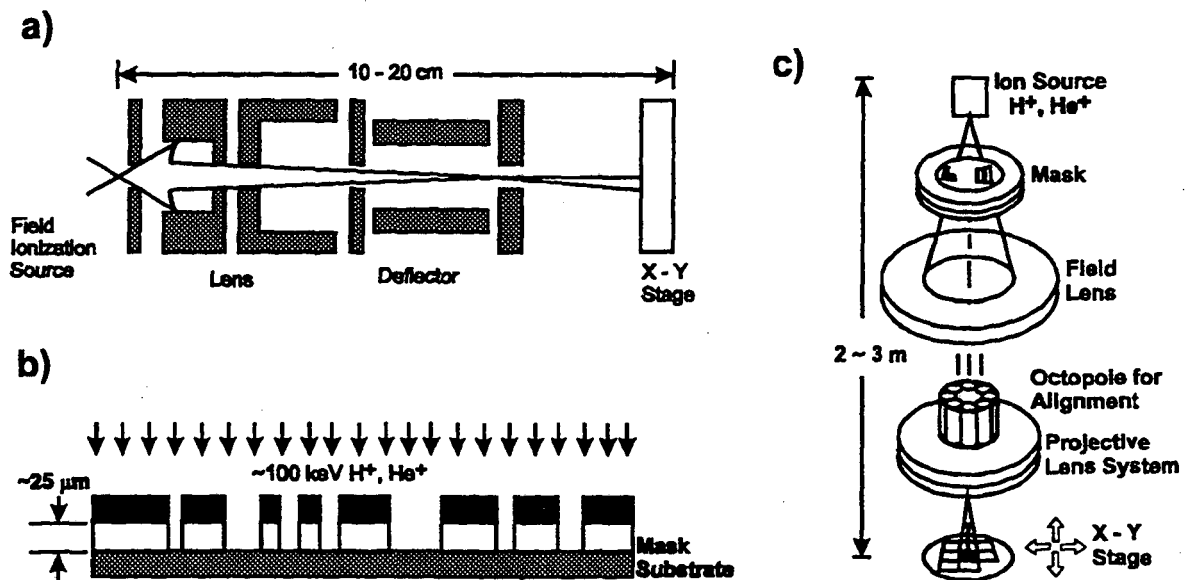
FIGURE 2.2 Ion beam lithographic strategies: (a) scanning focused
beam, (b) proximity printing, and (c) projection printing.

Considerable effort has been devoted to ion projection techniques which offer the advantage of parallel exposure. Two types of ion beam projection strategies have been explored: the 1:1 shadow or direct mask printing[11] and the reduction projection printing[12]. The fundamental concept of masked ion beam one to one lithography is shown in Fig. 2.2b. The collimated ion beam floods a large-area lithography mask that is in close proximity to the resist-coated wafer.

The basic features of ion beam reduction projection systems (Fig. 2.2c) are similar to their electron-beam counterparts. Systems have been developed that utilize open transmission "stencil" masks and 5 - 10 times reducing ion optics. Resolution of 0.15 μm has been demonstrated with an Alpha Ion Projector equipped with 5x ion-optical resolution over an exposure field 8 mm x 8 mm with a nickel open stencil mask[13,14].
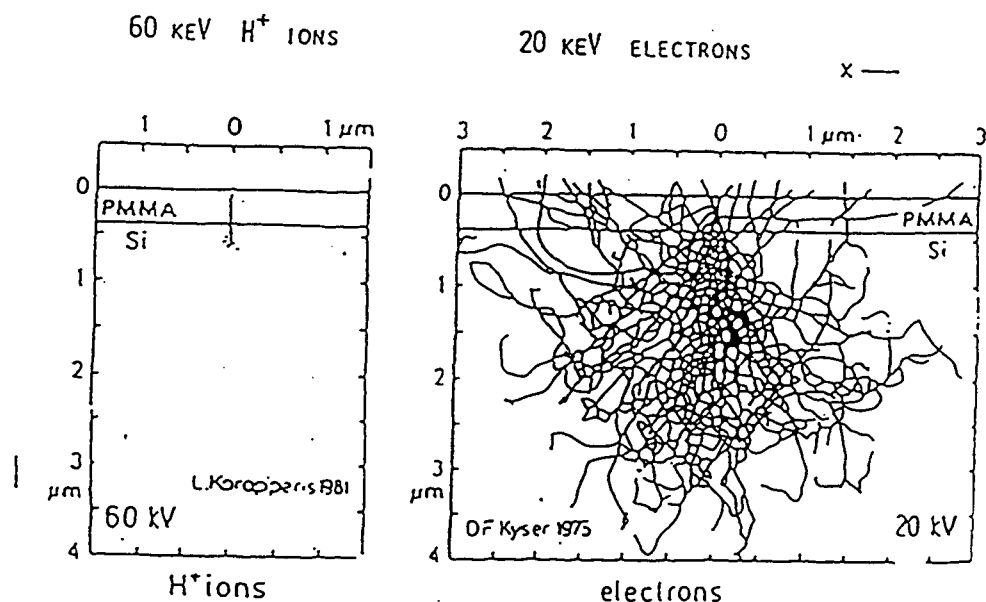
FIGURE 2.3 Comparison between e-beam and ion beam.

The chief advantage of ion beams in lithography is their negligible scattering, which is the primary factor limiting resolution in electron beam lithography, as shown in Fig. 2.3. The large effective mass of an ion compared with that of an electron, and greater cross-section of interaction with atoms of the resist result in energy being deposited in a much smaller volume. Penetration is more limited and takes place over a well-defined range. Thus, resolution is primarily limited by the range of the secondary electrons produced as the ion loses energy in the resist, whereas in electron-beam lithography, it is scattering of the much more energetic primary electrons that limits resolution. Fig. 2.4 shows the principles of ion projection lithography (IPL) which require an ion source that can provide low axial energy spread ion beams.

When using ions, lower doses are needed to have the same effect as with electrons because each ion deposits more energy into the resist than electrons. If the energy spread of the ion beam is significant, chromatic aberrations play a dominant role in limiting performance.
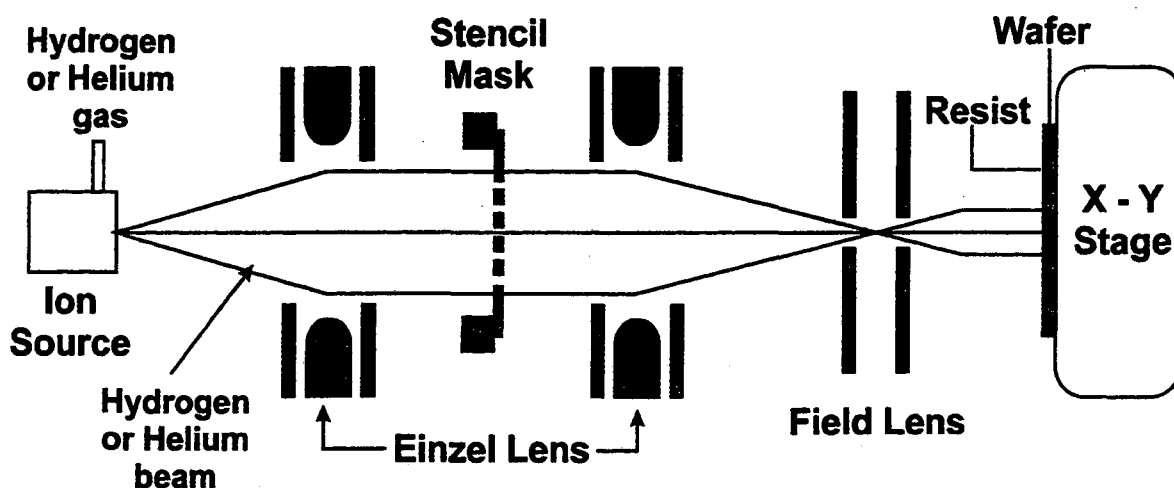
FIGURE 2.4 Principles of ion projection lithography.

a)

mask

800012 25KV X6.00K 5.0um

b)

2UM   24.7KV 25KU 80 17nn 8 00838 F 00003

wafer

80nm spaces   120nm spaces
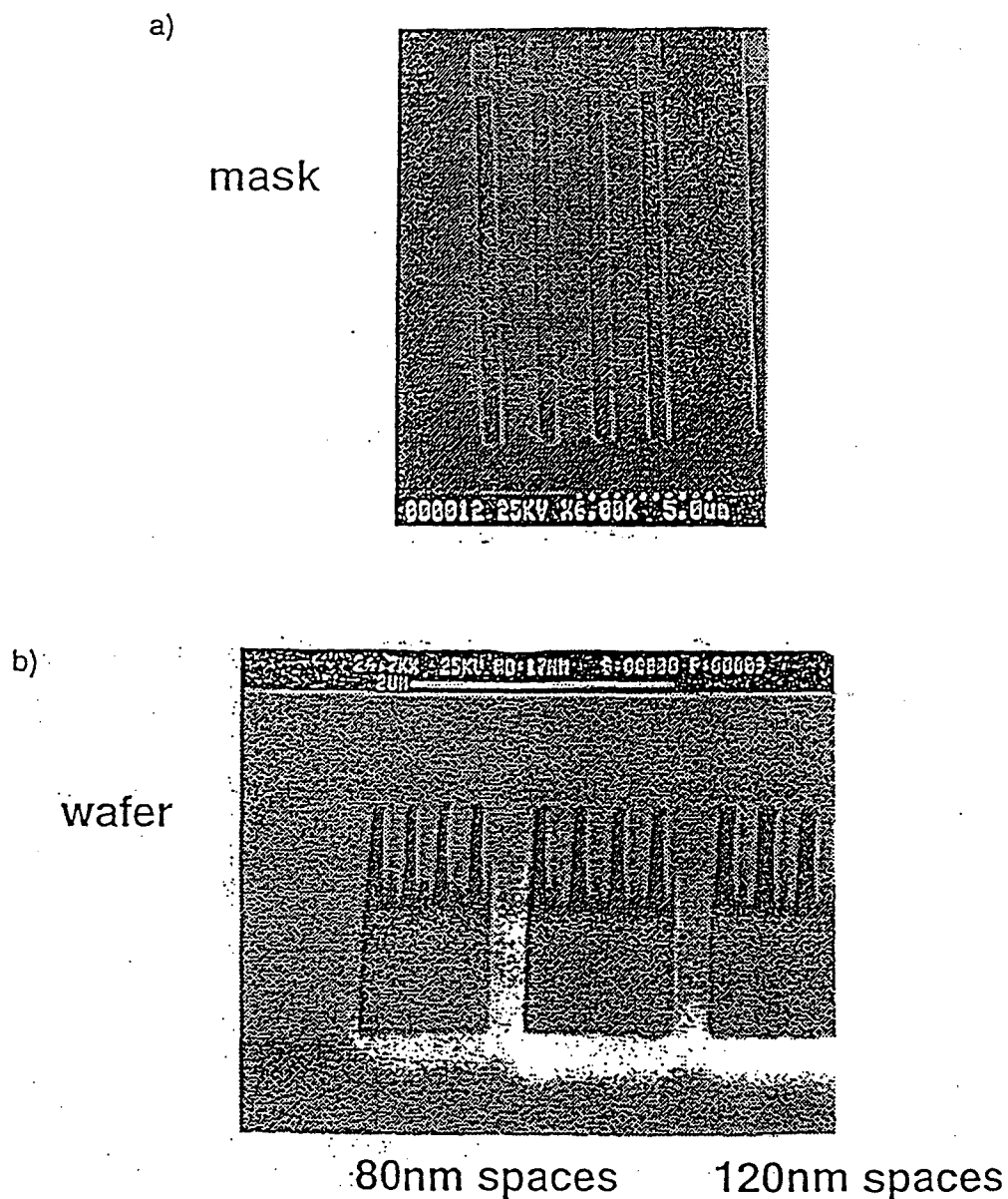
FIGURE 2.5 Image transfer in ion projector IPLM-02 onto UV II HS-0.6 resist. a) Mask pattern openings are 660 nm wide. b) The pattern on the substrate is demagnified by a factor of 8.4.

Resist exposures with an existing ion projector IPLM-02 (manufactured by Ion Microfabrication System (IMS), Vienna) have already been performed at the Fraunhofer Institute in Berlin.[15] H^+ and He^+ ions from a duoplasmatron source pass an open stencil

mask at a beam energy of 3.5 keV and are accelerated behind the mask to 75 keV. Structures on the open stencil mask are demagnified by a factor of 8.4 onto the wafer in this system. Features as small as 80 nm were achieved (Fig. 2.5). Duoplasmatron sources have an energy spread of approximately 10 eV. With the use of a source capable of producing ions with energy spreads less than 3 eV should allow the features sizes to be smaller.

2.1.2   FOCUSED ION BEAMS

Highly focused ion beams are needed for surface analysis, precision machining and deposition. Low ion axial energy spread source is necessary to minimize chromatic aberrations in focused ion beam systems, described in section 2.1.4.

The process of micro-machining relies upon one of the best known ionic impact phenomena, sputtering. This is an atomic cascade process, in which energy transferred to the surface of a solid by an energetic ion causes the ejection of surface atoms and ions.

One category of system is the ion beam mill, in which a broad area beam of inert gas ions, normally argon, is generated from a plasma source and used for sputtering. The process is entirely physical, with ion energies typically in the range 500 eV to 2 keV. The machining process is inherently slow and the use of chemically active ion beam species and background pressures of non-ionized reactive gas in the vicinity of the target is often employed to improve target removal rates.

2.1.3 ABERRATION

Because ions are so much heavier than electrons, the use of magnetic lenses to focus ion beams are not feasible. Electrostatic lenses have to be used instead. Fig. 2.6 illustrates the simplest case of a single lens, with the beam defining aperture subtending a half-angle α_o to the source.[16] The diameter of the ion beam at the target will be determined by a number of contributions as follows:
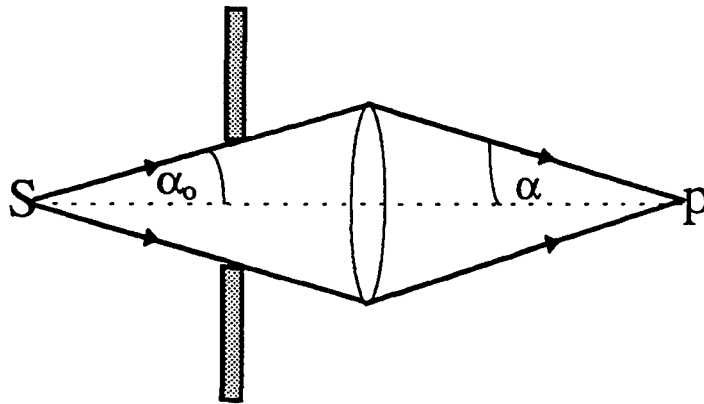
FIGURE 2.6 Schematic diagram of beam formation and single electrostatic lens.

i) *Spherical aberration d_s*

Spherical aberration produces a disc of least confusion with diameter strongly dependent upon the convergence half-angle α.

$$d_s = \tfrac{1}{2}\, \alpha^3\, C_s \qquad\qquad \text{(Eq. 2.1)}$$

Where C_s is the spherical aberration coefficient of the lens referred to the image side.

ii)   *Chromatic aberration d_c*

The diameter of the disc of least confusion, due to the energy spread ΔE of ions, having final energy E, is

$$d_s = \alpha \, (\Delta E/E) \, C_c \qquad \text{(Eq. 2.2)}$$

for chromatic aberration coefficient C_c referred to the image side. ΔE refers to the full width at half maximum (FWHM) axial energy spread of ions.

iii)   *Source limit d_o*

The finite size of the source will determine the ultimate limit on the probe size. Thus, if a lens with small aberration coefficients C_s and C_c is operated at vanishingly small values of α, so that the aberration discs vanish, the final probe will have a finite size determined by the magnification of the lens system and the virtual source size. For an ion optical system of magnification M, the contribution this makes to the final probe diameter is

$$d_o = M \, d_t \qquad \text{(Eq. 2.3)}$$

where the magnification M of the lens depends upon the ratio of voltages V_o and V_i in the image and object spaces, according to the Helmholtz-Lagrange relationship

$$M = (\alpha/\alpha_o) \, (V_o/V_i)^{1/2} \qquad \text{(Eq. 2.3)}$$

For the simple case represented in Fig. 2.6, as for many practical lenses, it can be assumed that $V_o = V_i$ in Eq. 2.3. Thus the small lens effect due to the extractor and earthed beam defining aperture is ignored in the analysis.

iv)   *Diffraction d_f*

The diameter of the final probe can be estimated by adding the contributions (i) - (iii) above. Since this is an area sum, the addition is performed in quadrature, to give

$$d_f^2 = d_o^2 + d_c^2 + d_s^2 \qquad\qquad \text{(Eq. 2.4)}$$

In a more complex lens systems, spherical aberration is relatively unimportant in the submicron regime, while finite source effects do not become significant until diameters below ~ 0.1 μm are sought. The dominance of chromatic aberration on the projected image is clear.

2.2   ISOBARIC SEPARATION IN RADIOACTIVE ION BEAM PRODUCTION

Radioactive beams were mentioned, for the first time, during the concluding discussion of the Symposium on Nuclides of Stability in Lysekil in 1966 where J.P. Bondorf pointed out the rich field of information that would be opened by a future use of unstable targets and projectiles in nuclear reaction studies.[17] The first radioactive beams were produced in 1969 by a group from LRL (later LBNL), Berkeley, that accelerated fission fragments from a ^{252}Cf source placed in the MIT MP Van De Graaff[18] accelerator.

There are two methods of producing high intensity Radioactive Nuclear Beams (RNB): projectile fragmentation and the on-line isotope separator (ISOL) method.

Projectile Fragmentation was pioneered in the beginning of the eighties at the Berkeley Bevalac. In this method, as illustrated in Fig. 2.7, an energetic ion beam is fragmented while passing through a target, and the reaction products are subsequently

transported to a secondary target after mass, charge and momentum selection in a fragment separator. Since the reaction products are produced in flight, no post acceleration is required. Fission in flight of very heavy beams, but also charge exchange and transfer reactions, have been used as an alternative to projectile fragmentation.

In addition to the high energy that the fragments automatically carry over from the primary beam in this production method and that is key to certain classes of experiments, the in-flight production also means that the subsequent experiments with the exotic fragments as a secondary beam can be done promptly. That is, they are only delayed by the flight time through the separator and beam line system to the reaction target, typically of the order of microseconds.
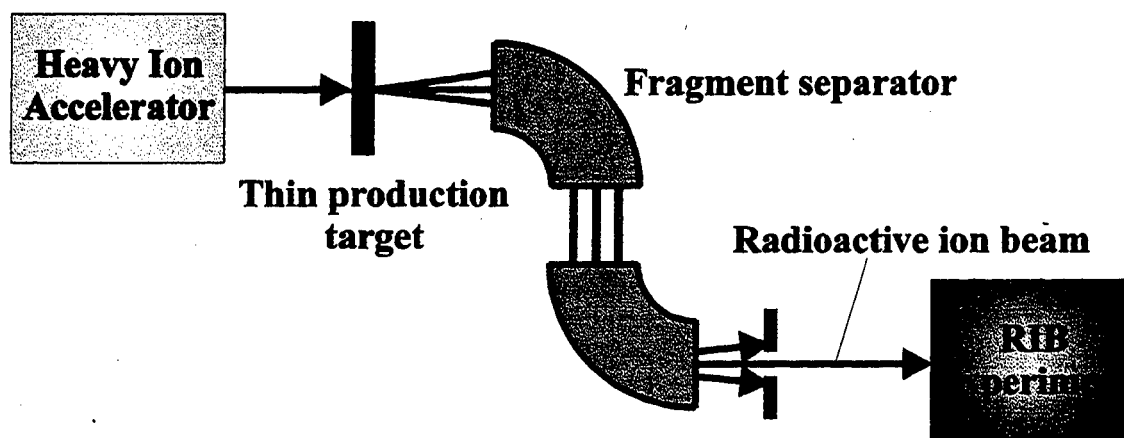
FIGURE 2.7 Schematic diagram of a projectile fragmentation facility. The primary accelerator directs a beam of heavy ions on a thin production target where the primary beam particles are fragmented into a variety of nuclear species. The radioactive nuclei of interest to the experiment are collected and selected out of the other species produced in the target in the fragment separator.

In an ISOL-type facility the radioactive nuclei are produced essentially at rest in a thick target by bombardment with particles from a primary source or driver (Fig. 2.8). After ionization and selection of a specific mass by electromagnetic devices, these nuclei are accelerated in a post-accelerator.[19]

Transfer tube — Ion Source — Isotope / Isobar Separator — Driver Accelerator — Thick, hot target — Driver beam — Postaccelerator — Radioactive ion beam (RIB)
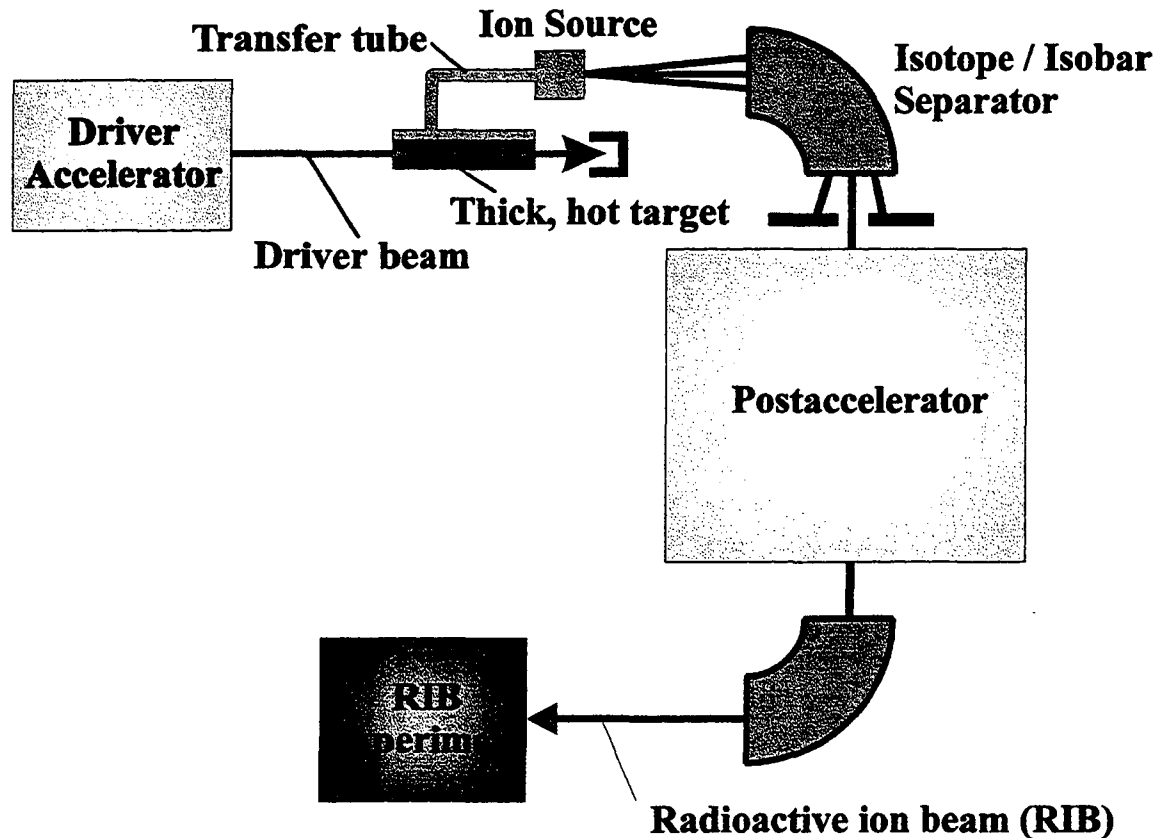
FIGURE 2.8 Schematic of a facility based on the Isotope Separator On Line (ISOL) method.

The radioactivity is introduced into an ion source in gaseous form and singly or multiply charged ions are produced. They are accelerated to energies of a few tens of keV and mass-analyzed by an isotope separator. The function of the separator is to provide beams for post-acceleration that are free of unwanted isotopes, isobars, ionic charges, and

molecular ions. For mass analysis of the isotopes, it is imperative to have a low axial energy spread ions in order to separate the different masses properly.

RNBs can be used in a wide range for experiments in the nuclear, astrophysical, atomic, and material sciences. In astrophysics, stellar phenomena such as the big bang, etc. can be better understood through RNB experiments. In materials research, RNBs is used for material radiation damage studies.[20]

CHAPTER 3

AXIAL ENERGY SPREAD OF THE FILAMENT-DISCHARGE

MULTICUSP ION SOURCE

3.1   DC FILAMENT GENERATED MULTICUSP PLASMA

Plasma can be generated in a multicusp ion source by dc discharge. In this case, the primary ionizing electrons are normally emitted from hot tungsten-filament cathodes. The source chamber walls form the anode for the discharge. The surface magnetic field generated by rows of permanent magnets, typically of samarium-cobalt, can confine the primary ionizing electrons efficiently. There are three main components in the source: the cathode, the anode, and the first or plasma electrode. The primary ionizing electrons are normally emitted from tungsten-filament cathodes. The source chamber walls form the anode for the discharge.

Two dc power supplies are needed to produce plasma by means of a dc filament discharge. One is for filament heating (the heater power supply) and the other is for the discharge (the discharge power supply). Fig. 3.1 shows the general schematic diagram of the discharge. The discharge or arc voltage usually ranges from 40 to 100 V. A filament driven multicusp ion source is shown in Fig. 3.2.
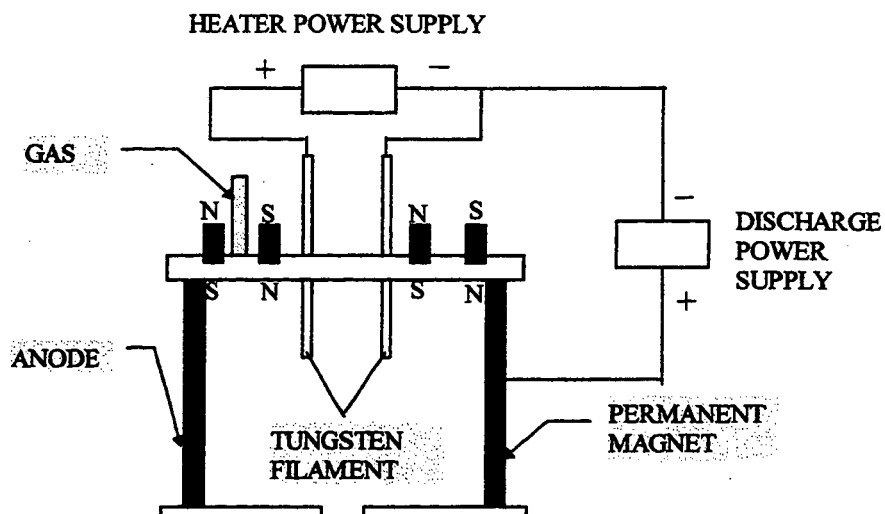
FIGURE 3.1 Filament discharge ion source and power supply set-up.
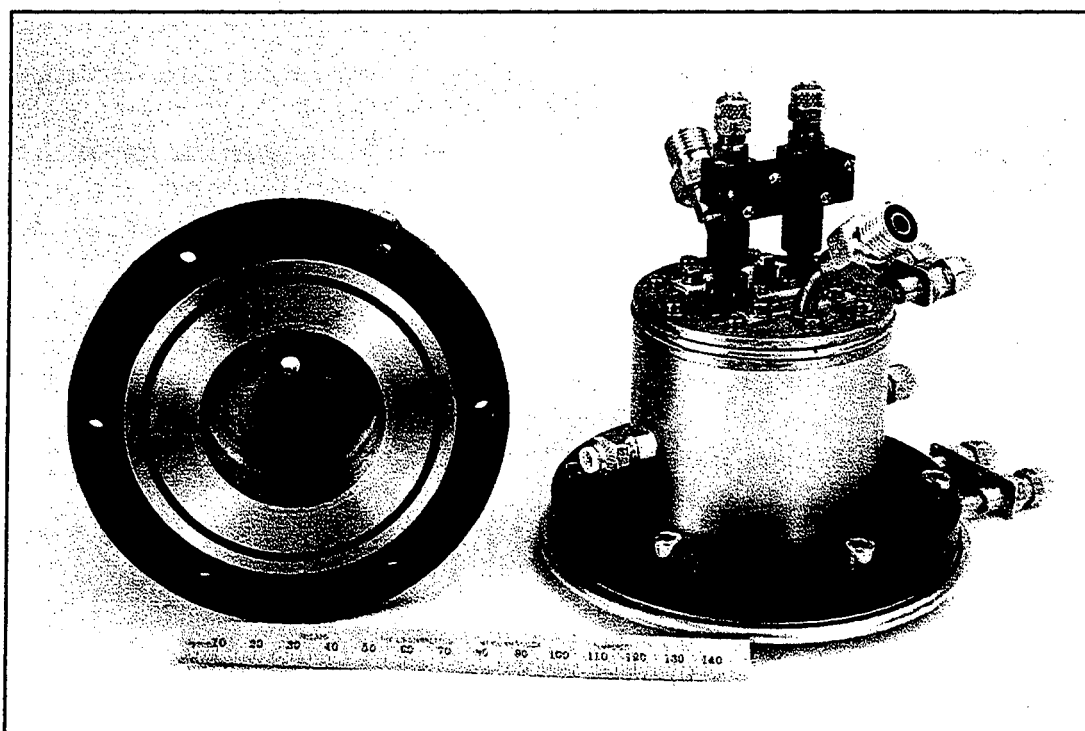
FIGURE 3.2 Picture of a multicusp ion source. The extraction system is attached to the open end of the source which is installed in the vacuum chamber.

3.2   PLASMA POTENTIAL DISTRIBUTION

A schematic diagram of a filament discharge multicusp source is shown in Fig. 3.3. The permanent magnets surrounding the chamber body can be arranged in rows parallel to the beam axis. Alternatively, they can be arranged in the form of rings perpendicular to the beam axis. The back plate also contains rows of the same permanent magnets.

In a plasma source, the ions are generated in a discharge chamber. From that point of generation they drift until a fraction of them reaches the extraction region. An overview of the extraction system is presented in Chapter 6.

If needed, a magnetic filter system can be installed in the source chamber as shown in Fig. 3.3. This filter then divides the chamber into two regions: (1) the discharge or source chamber, where the plasma is formed and contains the energetic ionizing electrons, and (2) the extraction chamber where a plasma with colder electrons is found. The filter provides a limited region of transverse magnetic field, which is made strong enough to prevent the energetic electrons in the discharge chamber from crossing over into the extraction chamber. This filter arrangement has been used to produce beams with high concentration of atomic ions. It has also been employed to provide high quality volume-produced H⁻ ion beams.[21]
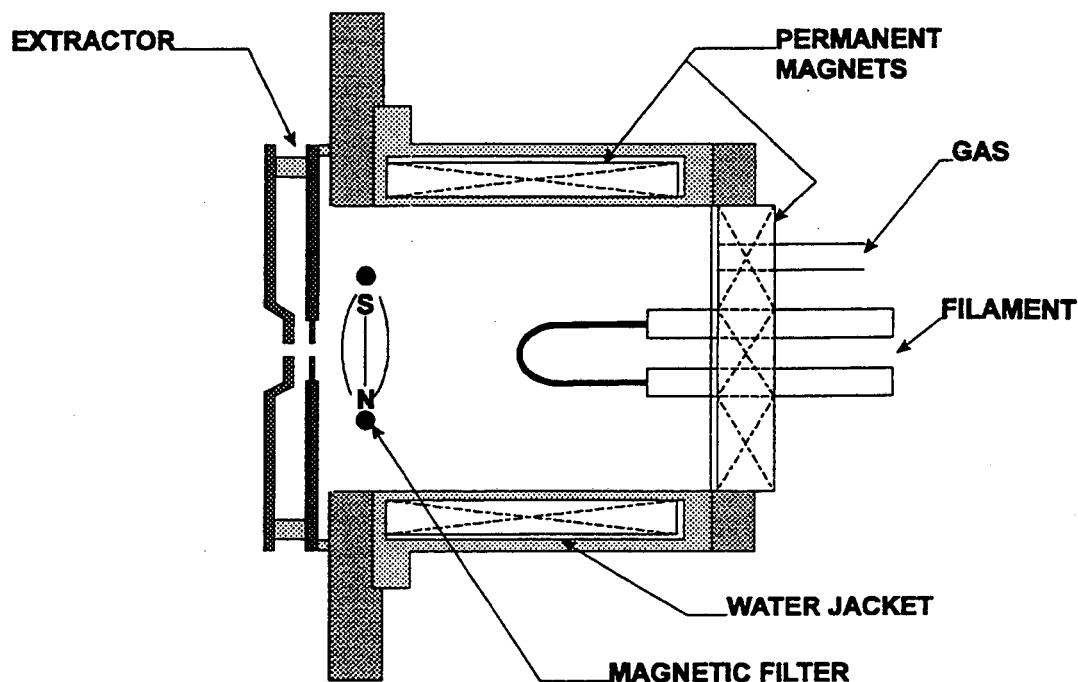
FIGURE 3.3 Multicusp ion source for dc discharge (hot tungsten filament cathode) operation. It also shows the magnetic filters installed in the source.

Fig. 3.4 shows a schematic diagram of an ion source and the plasma potential distribution along the axial direction.[22] In this figure, the source plasma is produced by a low pressure discharge with a hot tungsten filament cathode. The extraction electrode system in the figure shows the plasma, suppression, and ground electrodes, respectively. The electrodes have different applied voltages: acceleration voltage V_{acc}, deceleration voltage V_{dec}, and ground potential, respectively.
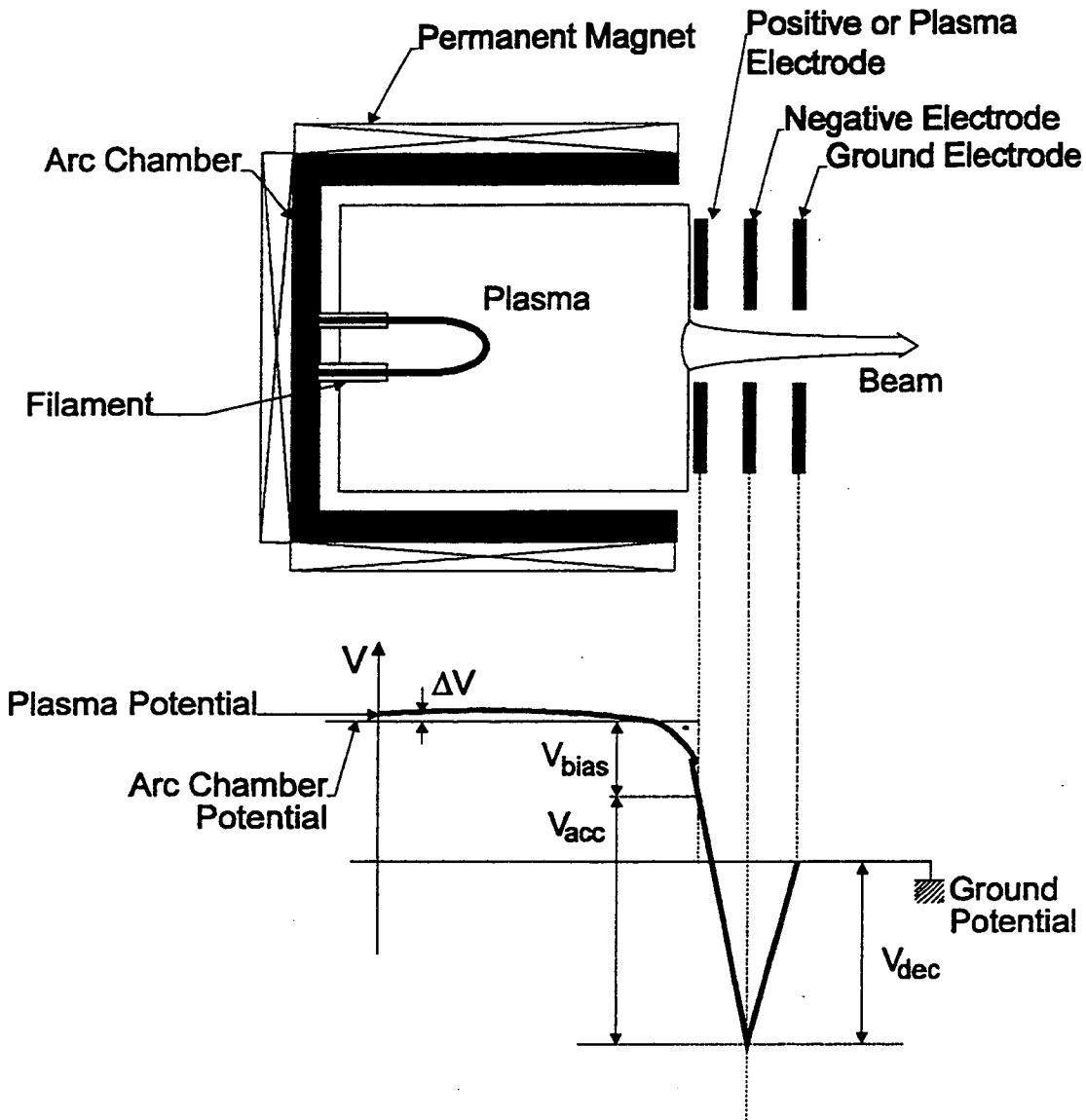
FIGURE 3.4 Sketch of the ion beam source and potential distribution on axis. ΔV denotes the potential difference between the discharge chamber and source plasma.

A plasma sheath voltage V_{sh} is controlled by applying a bias voltage V_{bias} between the discharge chamber and the plasma electrode. The difference of the potential ΔV between the discharge chamber and the plasma does not change by the application of the bias voltage.
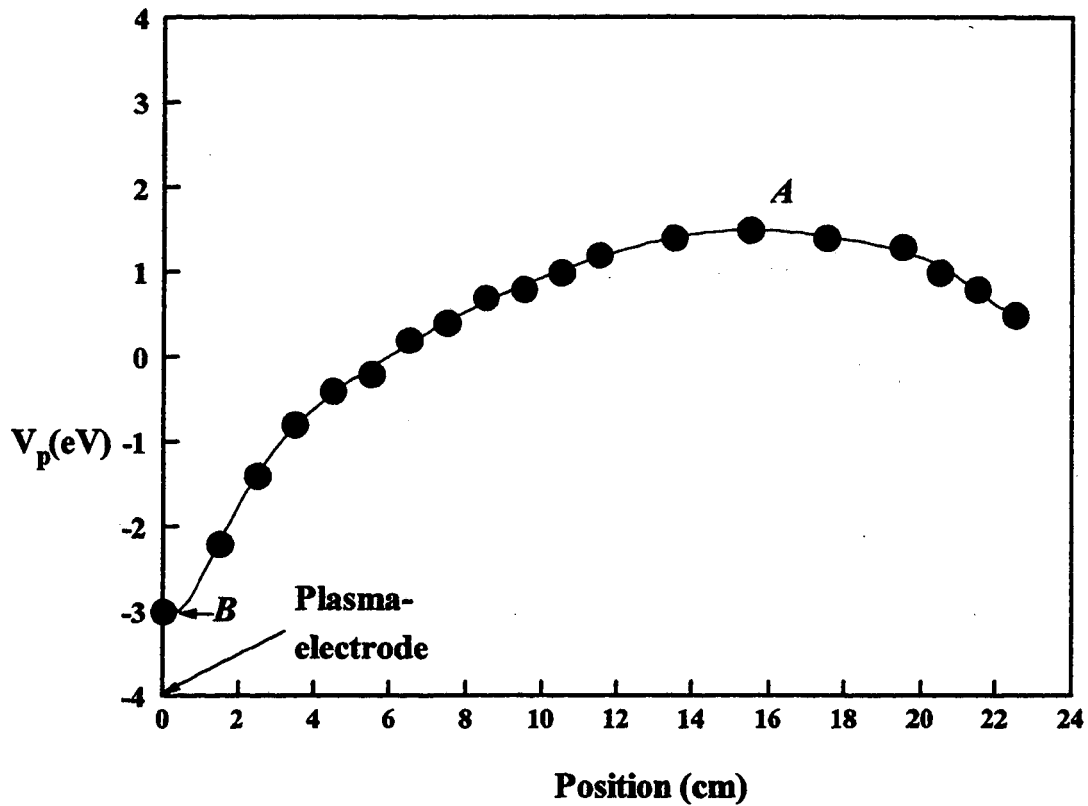
FIGURE 3.5 Axial plasma potential profile inside the source in the
absence of a magnetic filter.

The axial plasma potential (V_p) profile has been previously measured for a

multicusp source.[23] Fig. 3.5 shows the plasma potential distribution inside the source on

axis as a function of the axial position. The plasma potential decreases monotonically

towards the plasma electrode. *A* and *B* are the maximum and minimum plasma potential

values, where ions can be born, i.e. ionization takes place. Ions formed at position *A* have

more potential energy than ions generated in position *B*, given by the difference in

potential between the two points. Positive ions generated at high V_p will reach the extractor as well as the ions created at lower potentials. Since the ions are generated at positions with different plasma potential, they will have a spread in axial energy when they arrive at the extraction aperture.

One way to level the plasma potential is by introducing a pair of filter magnets inside the source chamber. Such arrangement can be seen in Fig. 3.3. The filter creates a region with a relatively uniform V_p profile in the discharge chamber region, as shown in Fig. 3.6.
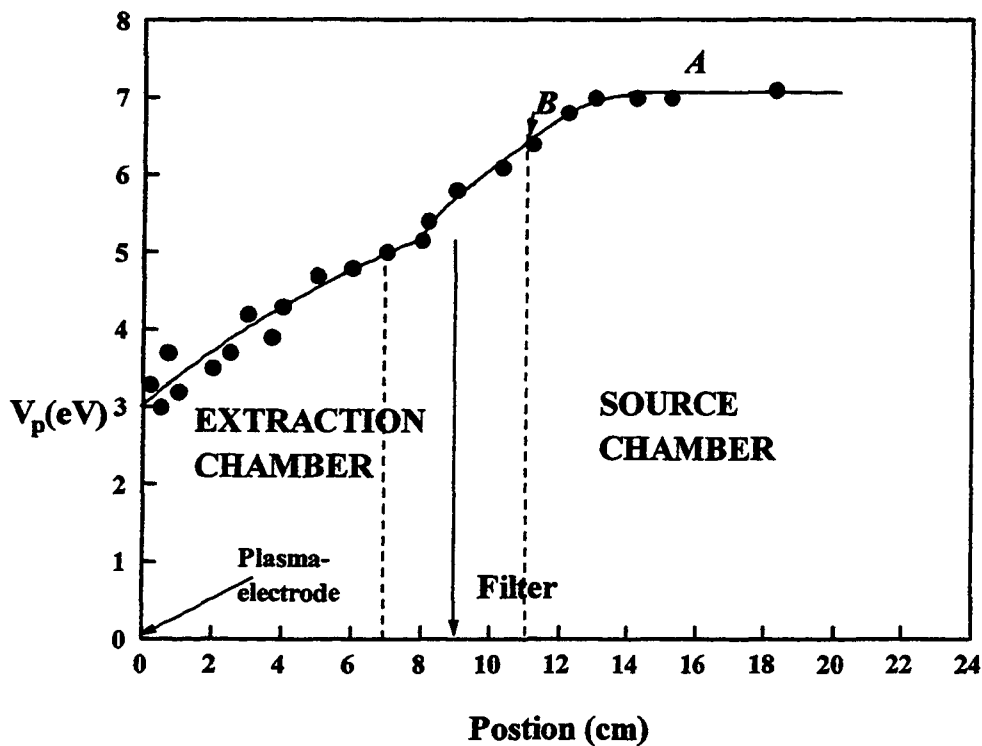
FIGURE 3.6 Axial plasma potential profile inside the source in the presence of filters.

Primary electrons emitted from the filament cathode are confined in the source chamber by the filter's magnetic fields as well as the multicusp fields on the chamber walls. The potential gradient in the extraction region produces no effect on the energy spread. Since all the positive ions are produced within the source chamber region, they arrive at the plasma electrode with about the same energy due to the uniform V_p distribution. However, there is still a small potential gradient, given by the potential difference between point A and B (in Fig. 3.5, less than 1V), between the center and the filter (~80 gauss) region that causes a small spread.

3.3 AXIAL ION ENERGY SPREAD MEASURED AT THE SOURCE EXIT

3.3.1 AXIAL ION ENERGY SPREAD SETUP AND ANALYSIS

A simple biased grid analyzer has a useful place in plasma diagnostics. The energy analyzer shown in Fig. 3.7 uses a fine mesh grid which is biased negatively with respect to the plasma to screen away the electrons. However, positive ions will pass through the screen unhindered.[24] A collector plate located downstream from the grid is used to measure the ion current. The plate is connected to a variable power supply. Only ions with energies greater than the applied voltage to the plate will be collected in the cup. At negative collector bias, all the ions which passed through the negatively biased grid will be collected. As the bias voltage becomes more positive the low energy ions will be repelled and will not be collected. As a result the plate current decreases. At sufficient positive collector bias, no ion current reading is observed.
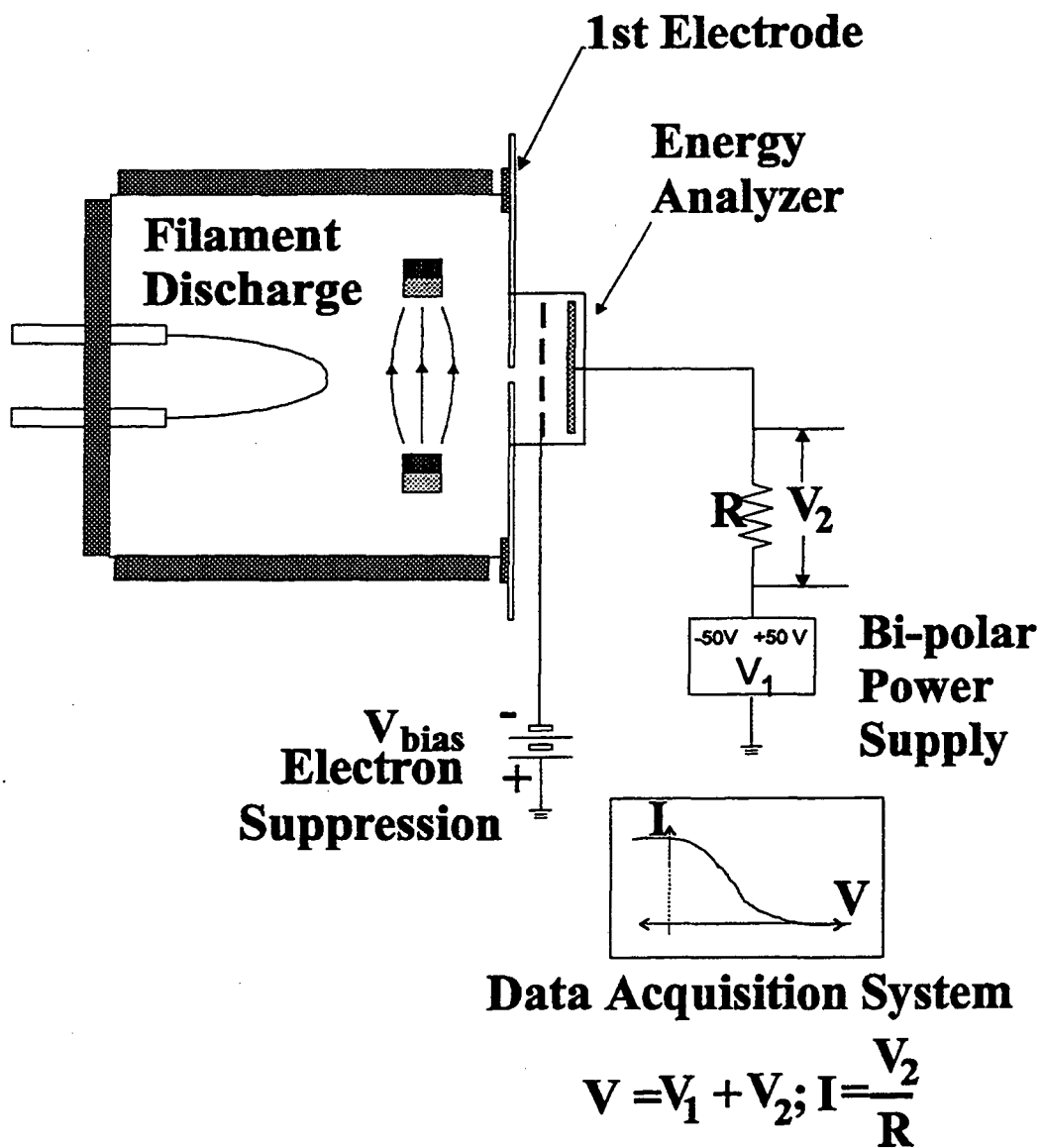
FIGURE 3.7 Schematic diagram of the ion source and energy analyzer assembly.

The plasma particles have kinetic energy of motion. The energy distribution of the

particles can be measured with the energy analyzer, which records the distribution in terms

of ion current (measured in a collector electrode) versus voltage (collector electrode is

biased with respect to the source anode). At voltages less than the ion energy, ions are collected and a positive current is read. As the applied voltage becomes more positive than the ion energy, the collector current gradually decreases. If the voltage is sufficiently positive, the collector current becomes zero.

Plasma density and potential are obtained with Langmuir probes. The gridded retarding field energy analyzer is used to study the axial or longitudinal energy spread of the positive ion species at the exit aperture of the ion source. The analyzer is connected to a computerized data acquisition system, consisting of a computer program, two multimeters and RS232 interfaces that can measure energy spreads with a resolution of about 0.01eV.[25] The entire assembly is illustrated in the schematic diagram in Fig. 3.7.

The energy analyzer has a grid which is biased for electron suppression and a collector for energy distribution measurement. The beam current can be determined by the voltage drop across a resistor. As shown in Fig. 3.7, the collector voltage V is equal to V_1 + V_2, and the beam current is determined by V_1. In most cases, the internal resistance of the multimeter is used, which was found to be exactly 10.03 MΩ and which remains constant over the range of the measured voltages. For low current measurements no extra resistors are needed because the internal resistance of the multimeters is high enough. An additional resistors can be used in parallel for higher beam currents. The current versus voltage curve is displayed in the computer monitor.

Fig. 3.8a shows a representative V-I characteristic curve. In Fig. 3.8b, the curve is differentiated. The Full Width at Half Maximum (FWHM) of the differentiated curve is defined as the energy spread, ΔE, of the ions. The voltage of the maximum dI/dV curve is

the average energy of the beam. In Fig. 3.8b the curve is shown to be Gaussian, in reality it could be other.
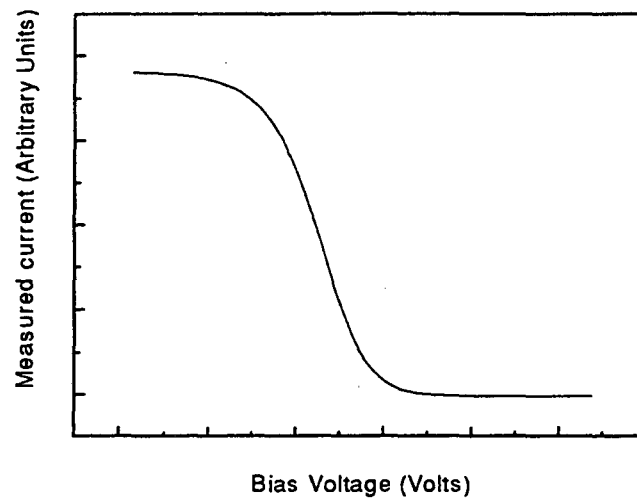
FIGURE 3.8a   A representative sketch of ion current distribution.
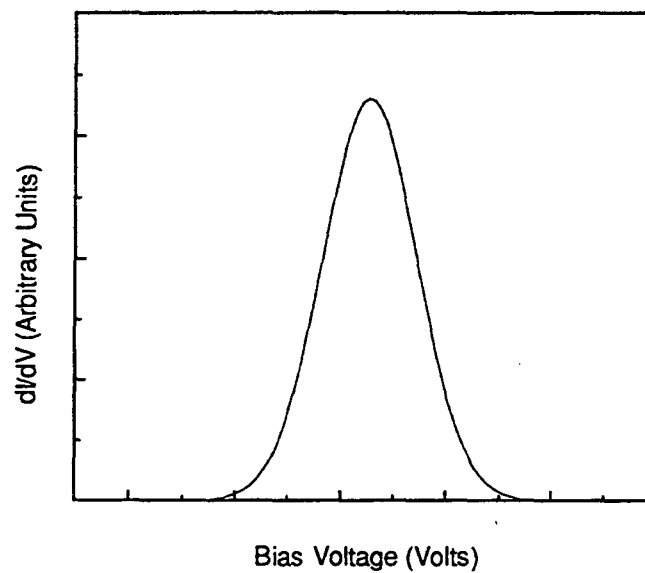
FIGURE 3.8b   V-I curve differentiated. Energy spread is defined as the full width half maximum (fwhm) and the peak of the curve occurs at the average energy of the ion beam.

3.3.2 AXIAL ION ENERGY SPREAD WITHOUT FILTER

Experimental study of axial ion energy spread was performed on two different multicusp ion sources, one is 24 cm diameter by 25 cm long and the other is 10 cm diameter by 10 cm long.

The energy spread of the 24-cm-diameter source as well as the 10-cm-diameter source operated without the filter is larger than in the case with filters. This is largely due to the axial plasma potential distribution inside the source chamber described in the previous section. Furthermore, the large energy spread may also be due to ionization taking place in the plasma sheath of the extraction aperture. Fig. 3.9 shows an ion optics simulation of an extraction system operating at an "underdense" condition. In this particular case, some equipotential lines penetrate far into the source chamber. Energetic electrons that arrive at this boundary may still have energies to produce ionization, causing an energy spread of the ions in the accelerated beam.
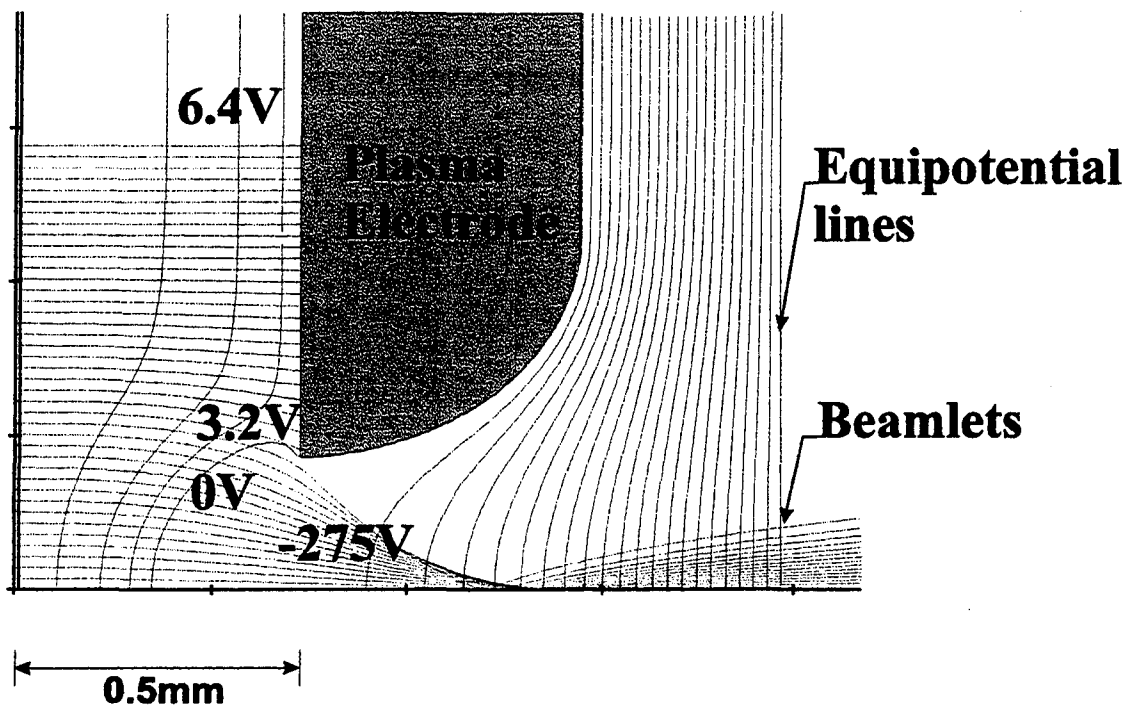
FIGURE 3.9   Equipotential boundaries at the extraction aperture.

Charge exchange (He^+ + He --> He + He^+) can take place if the corresponding

mean free path ($\lambda = (n_0\sigma)^{-1}$) is not large compared to the length of the source. Here, n_0 is

the neutral atom density, and σ is the cross-section for charge exchange process.

For the 24-cm-diameter source with filament discharge, the ΔE was found to be

approximately 6.5 eV. The experimental data and the differentiated curve are shown in

Fig. 3.10a and 3.10b, respectively.
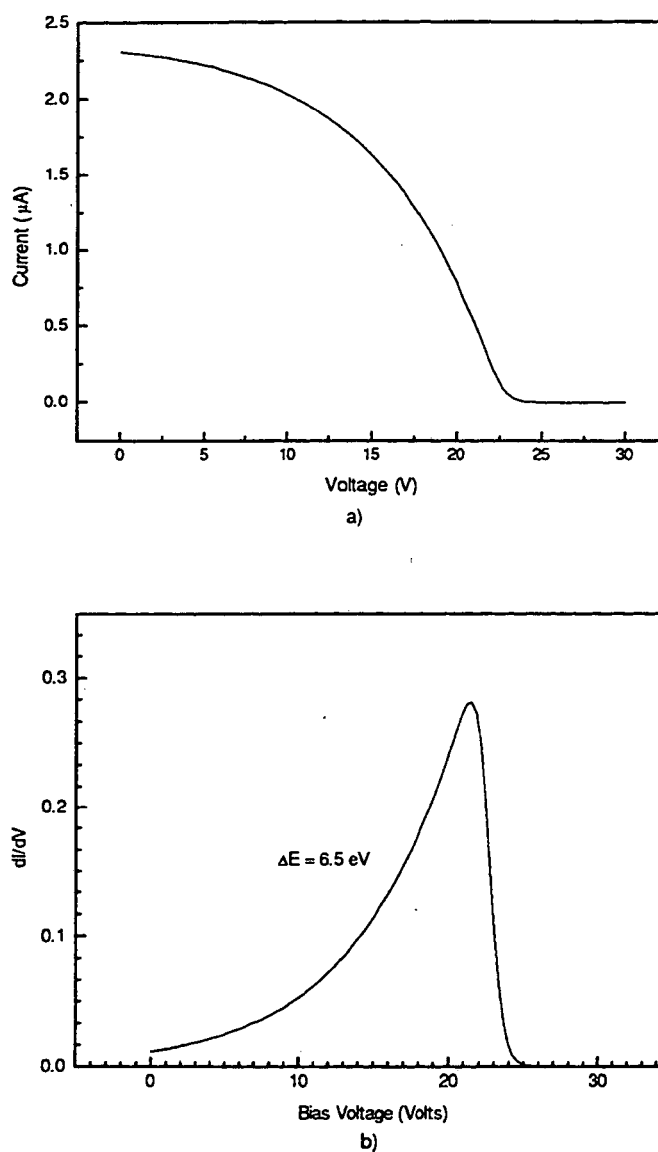
FIGURE 3.10 a) The experimental data for a 24-cm-diameter source under filament discharge operation without filter. b) The experimental data of a) was differentiated and the ΔE found is approximately 6.5 eV.

In an attempt to reduce the energy spread, low energy electrons were injected in the 24-cm-diameter source in order to reduce the entire V_p.[26] The injection of low energy electrons lowers the plasma potential as shown by the probe traces in Fig. 3.11. The injection of low energy electrons was achieved by a second set of filaments with the

corresponding two power supplies; one to provide heating of the filament and the second for the discharge. The discharge voltage was set at a value lower than the ionization potential of the gas.
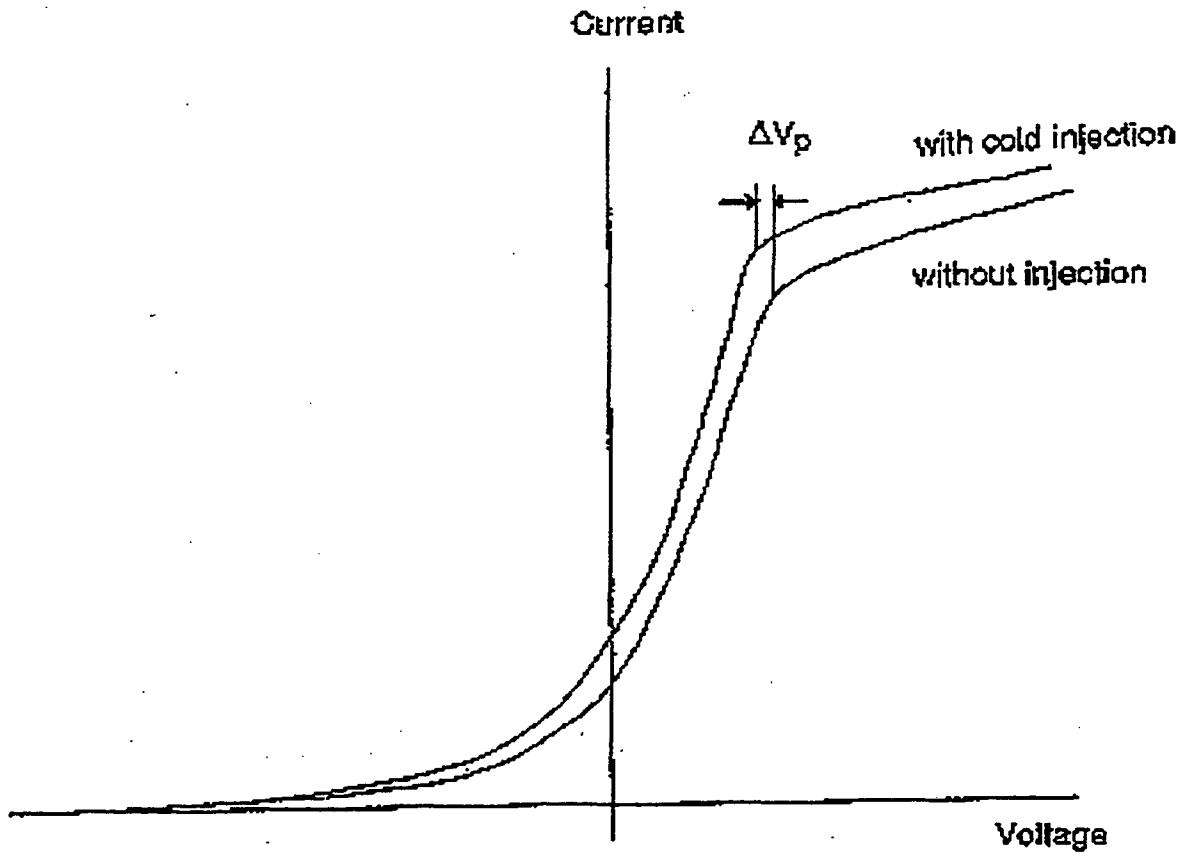
FIGURE 3.11 Injection of low energy electrons. The figure shows the Langmuir probe trace before and after the cold electron injection, V_p is lowered after injecting the cold electrons.
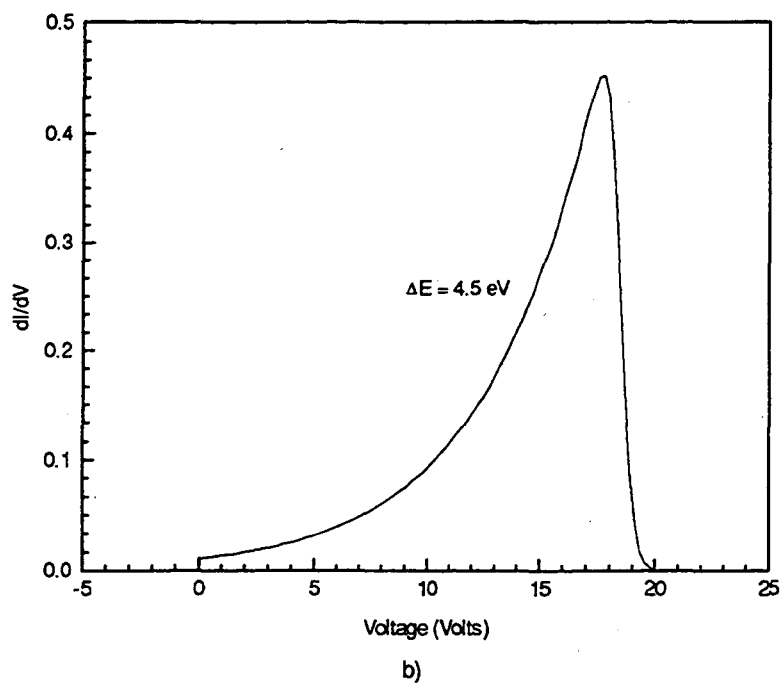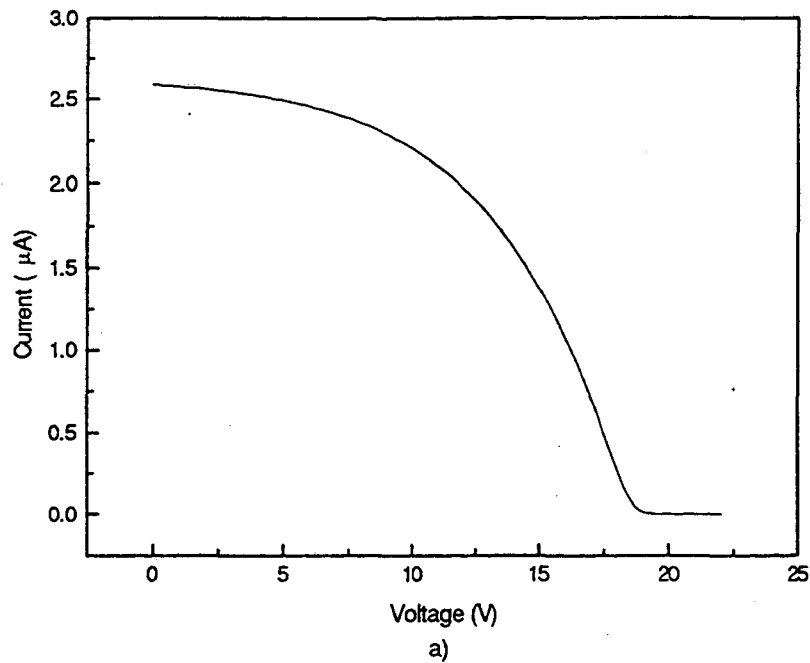
FIGURE 3.12   Energy spread after the cold electron injection in the 24-cm-diameter source without filter. The ΔE found is approximately 4.5 eV.

It is observed that the energy spread is reduced from the 6.5 eV (Fig. 3.10) without the cold injection, to approximately 4.5 eV (Fig. 3.12) with cold electron injection. Lower energy spread was expected since with the presence of the cold electrons, the difference between the maximum V_p and the minimum V_p where ionization would take place decreases, and this difference is the principal cause of the longitudinal energy spread. However, the results are different when a "magnetic filter" is present.

The 10-cm-diameter source under filament discharge operation, without filter, was operated under various pressures, discharge currents and different configurations (first electrode floating or connected to the anode). Similar to the 24-cm-diameter source, this source was operated with helium gas, with a discharge voltage of 70 V and a discharge current ranging from 1 to 4 A.

ΔE was observed to range from approximately 3 to 7 eV under different conditions of discharge current, pressure and plasma electrode arrangement. Fig. 3.13 shows one measurement with its corresponding differentiated curve for this source.
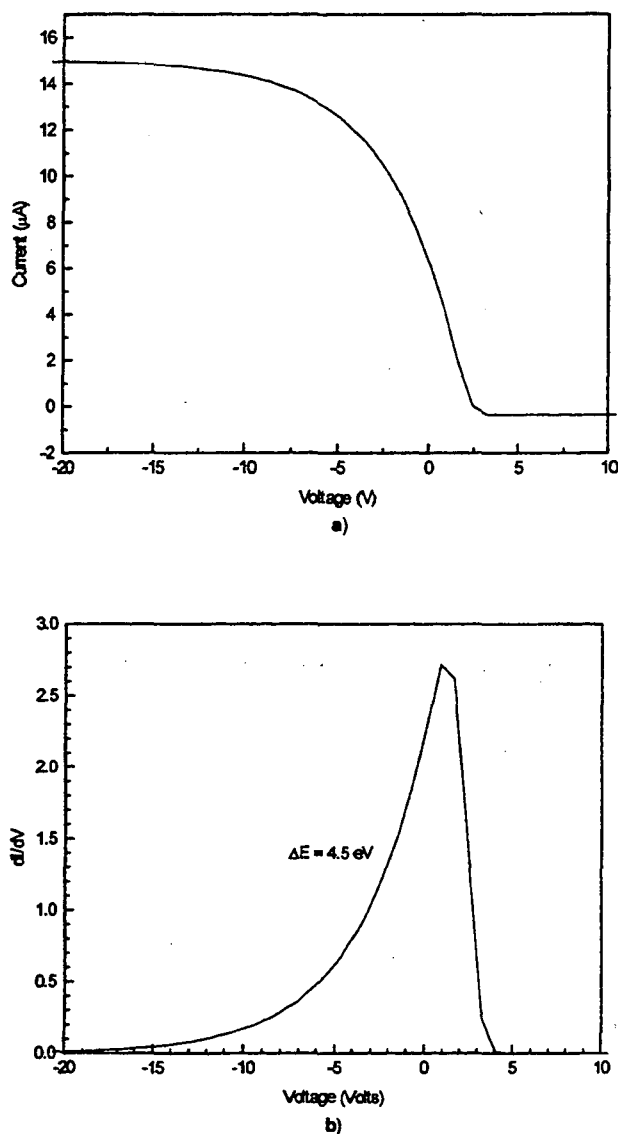
FIGURE 3.13 a) The experimental data for a 10-cm-diameter source under filament discharge operation without filter is shown. b) The experimental data of a) was differentiated and the ΔE found is approximately 4.5 eV.

The electrode arrangement study was performed on this 10-cm-diameter source and the result is shown in Fig. 3.14 and Fig. 3.15. The two figures summarize the pressure and discharge current dependence of the two arrangements. The energy spread

changes noticeably when the parameters (plasma electrode arrangement, discharge current and pressure) are changed.
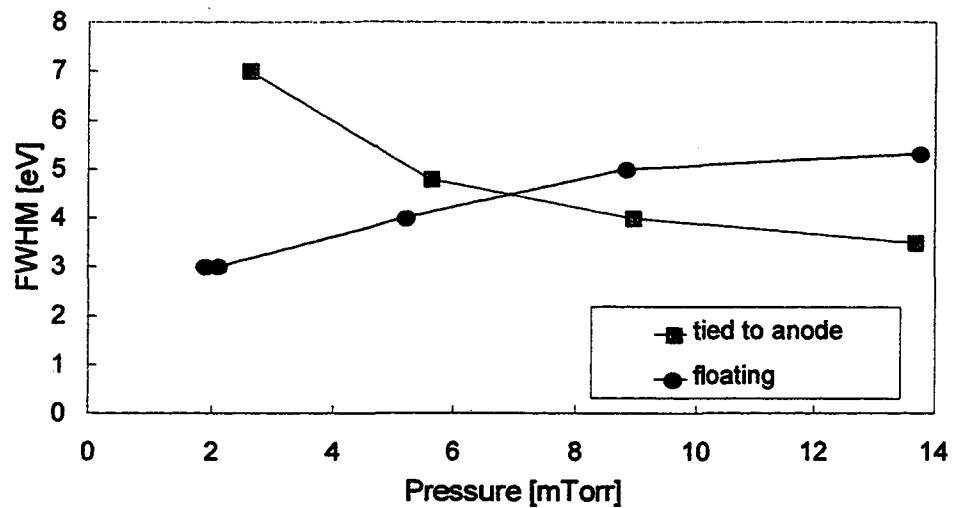
FIGURE 3.14 Energy spread versus pressure for a 10 cm diameter source, filament operation, without filter. Results of the two plasma electrode arrangements are shown.
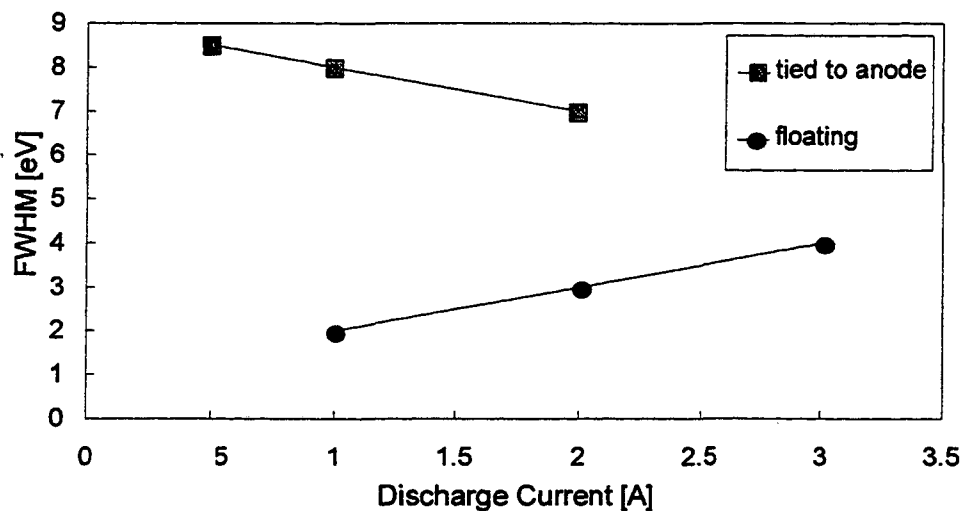
FIGURE 3.15 Energy spread versus discharge current for a 10-cm-diameter source, filament operation, without filter. Results of the two plasma electrode arrangements are shown.

In Fig. 3.14, the ΔE measurement shows that the energy spread decreases with increasing pressure when the plasma electrode is connected to the anode. At high pressures, ionization takes place close to the filament cathode. Primary electrons have difficulties in reaching the extraction region where V_p is decreasing rapidly. Secondary emission electrons originated from the plasma electrode will not have enough energy to ionize the neutral particles. As seen in Fig. 3.15, energy spread difference between the two arrangement is large. With the first electrode floating the energy spread is smaller than with the electrode electrically connected to the anode. This is because when the electrode is floating, more primary electrons are reflected to perform ionization generating ions at non-uniform plasma potential regions. Thus, a larger ion energy spread is observed.

3.3.2 AXIAL ION ENERGY SPREAD WITH FILTER

The 24-cm-diameter source was operated with a filter installed, and the energy spread measurement was performed. In this case ΔE was found to be approximately 2.3 eV as shown in Fig. 3.16 which is clearly lower than the case without filter.

The reduction of energy spread with the filter can be easily explained from the V_p distribution measurement in Fig. 3.5. The presence of a filter created a region with a relatively uniform V_p profile in the discharge chamber region. Primary electrons emitted from the filament cathode are confined in the source chamber by the filter magnetic fields as well as the mullticusp fields on the chamber walls.
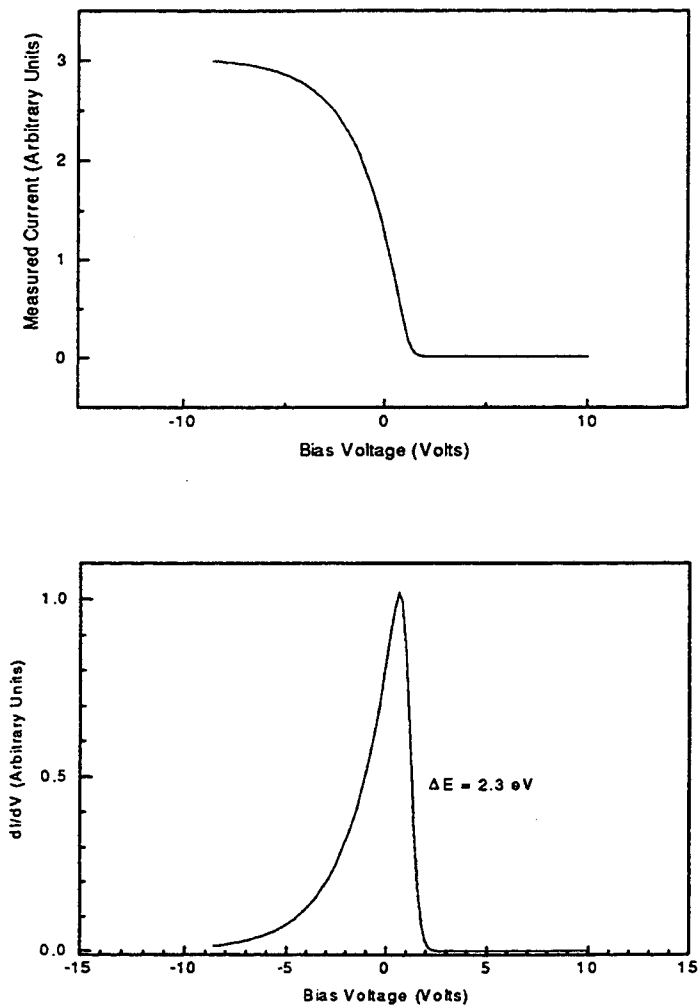
FIGURE 3.16 a) The experimental data for a 24-cm-diameter source under filament discharge operation with filter is shown. b) The experimental data of a) was differentiated and the ΔE found is approximately 2.3 eV.

The potential gradient in the extraction region produces no effect on the energy spread. Since all the positive ions are generated within the source chamber region, they arrive at the plasma electrode with about the same energy due to the uniform plasma potential distribution. Although, there remains a small potential gradient, given by the

potential difference described in Fig. 3.6, the longitudinal energy spread of the ions are reduced considerably from the case without filter.

In the presence of a filter, the equipotential surfaces that penetrate into the extraction chamber of Fig. 3.10 have a negligible effect on the energy spread since the absence of energetic electrons on the extraction side prevents ion production in that region.

Fig. 3.17 shows Langmuir probe traces obtained in the discharge chamber and the extraction chamber. The electron temperature of the extraction side is 0.25 eV, much lower than the discharge side, 1.5 eV. Only cold plasma electrons are present in the extraction chamber. As a result, almost no positive ions are expected to be formed inside the extraction chamber.

Moreover, operating pressures for the case with filter are lower than without filter. Therefore, the mean free path for charge exchange is longer, reducing the possibility of ion formation due to charge exchange in the ionization region.

Unlike the case without filter, the injection of low energy electrons does not affect the energy spread for this case. The plasma potential distribution remains uniform in the discharge chamber. The overall plasma potential decreases, but the cause of the energy spread is not affected by the decrease since it is given by the smaller potential drop between the center and the filter region, which remains almost unchanged.
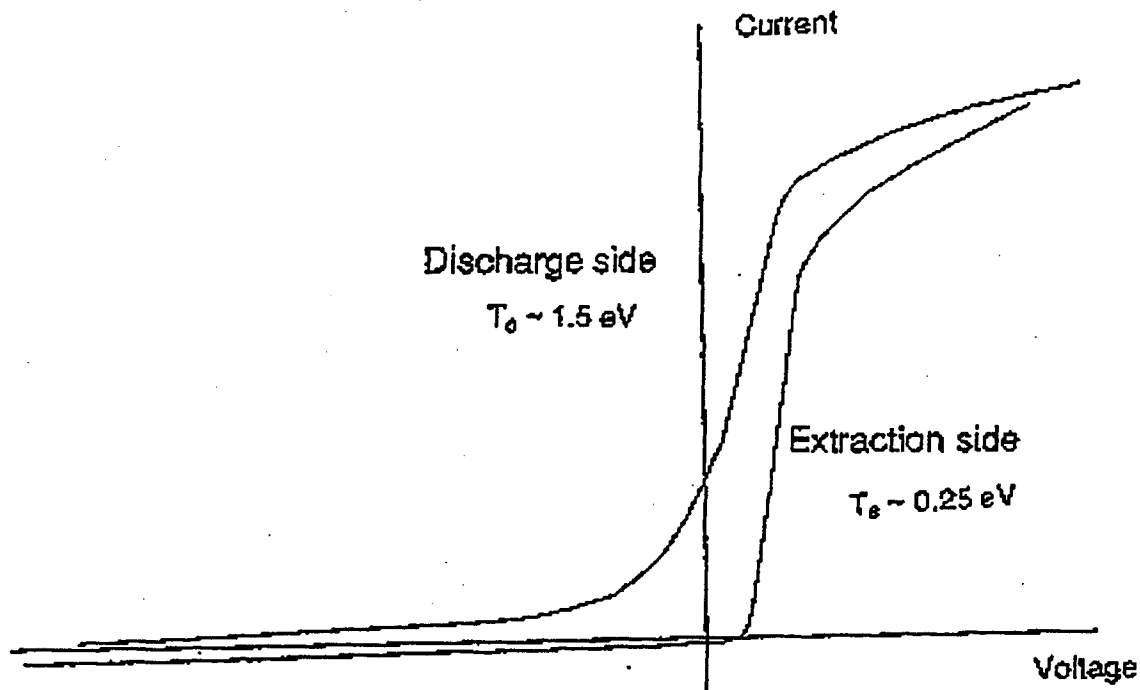
FIGURE 3.17 Langmuir probe trace in the discharge chamber and the extraction chamber in a multicusp ion source with the presence of a filter.

The effect of a magnetic filter on the energy spread for the 10-cm-diameter source was also investigated. Fig. 3.18 shows the measured data and its corresponding differentiated curve. The lowest energy spread for this source was found to be approximately 1.2 eV. These results are similar to those observed in the larger 24-cm source.
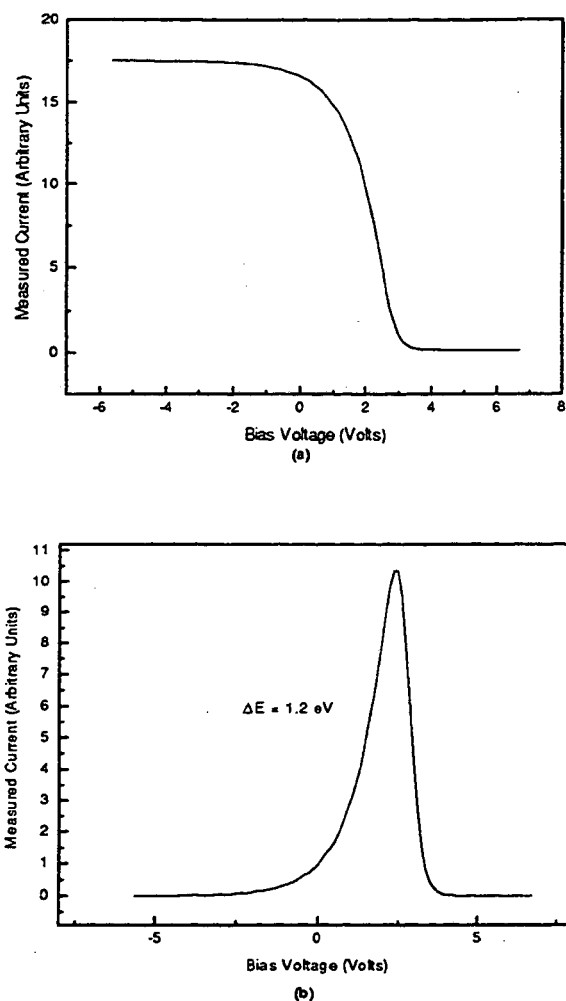
FIGURE 3.18 a) The experimental data for a 10-cm-diameter source under filament discharge operation with filter is shown. b) The experimental data of a) was differentiated and the ΔE found is approximately 1.2 eV.

Thus, it was proven that the multicusp ion source can provide ions with low axial energy spreads. Two different techniques were also used to confirm the results that have been found in this Chapter, and are presented in chapters 5 and 6.

CHAPTER 4

THE RF-DRIVEN MULTICUSP ION SOURCE

4.1   RF-SOURCE DESCRIPTION

There are two ways in which a low pressure gas can be excited by RF voltages: (1) a discharge between two parallel plates across which an alternating potential is applied (capacitively coupled discharge), and (2) a discharge generated by an induction coil (inductively coupled discharge). Most RF-driven ion sources are operated with the second type of discharge. A few hundred watts of RF power is typically required to establish a suitable discharge. The RF frequency can vary from a megahertz to tens of megahertz.

Fig. 4.1 and 4.2 show a schematic diagram of an RF-driven ion source and a picture of an RF-source with a porcelain-coated antenna, respectively. An RF discharge is generated by placing an induction-coil antenna inside the source. An azimuthal electric field is generated by the alternating magnetic field in the discharge region. Electrons present in the gas volume are accelerated by the induced electric field. They quickly acquire enough kinetic energy to form a plasma by ionizing the background gas particles. The ions are then extracted from the source chamber in a manner similar to a dc discharge source.
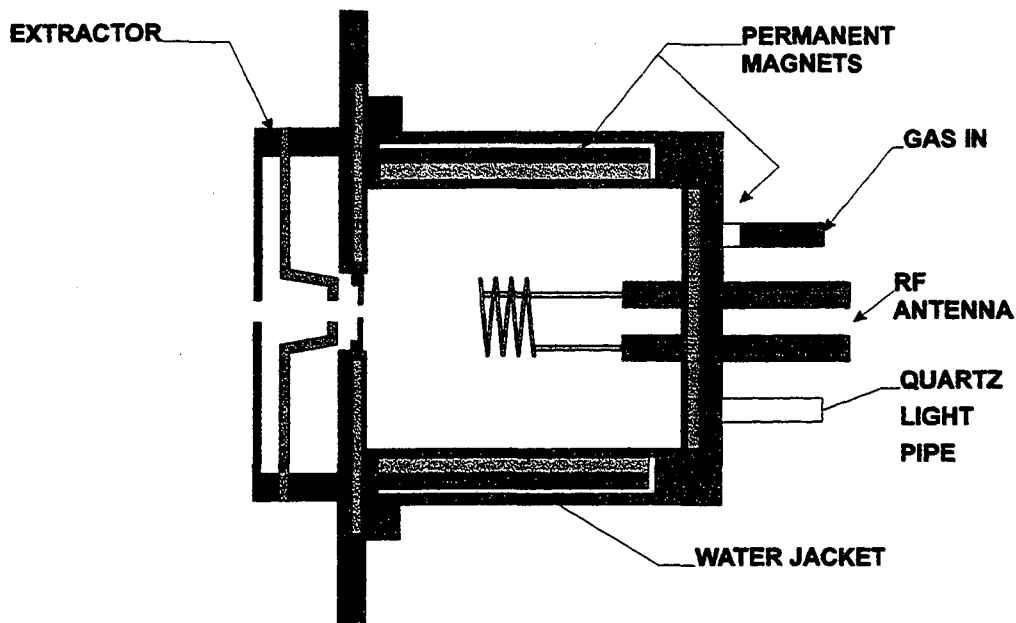
FIGURE 4.1   A schematic diagram of a multicusp ion source with an RF- antenna is shown above.
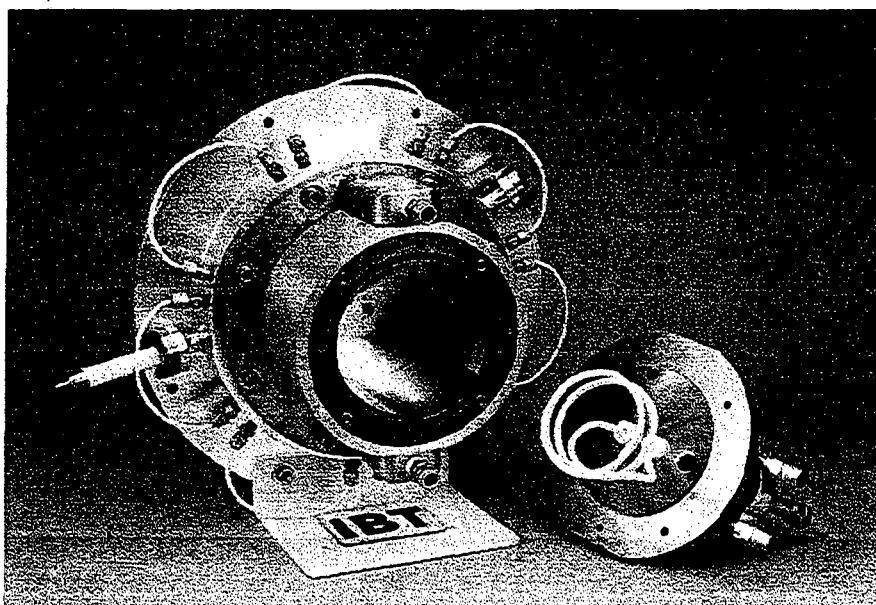
FIGURE 4.2   A picture of a multicusp ion source with an RF-antenna is shown above. The antenna shown can be exchanged with another antenna of different size and/or geometry.

The antenna coil is connected to a matching network and isolation transformer, matching the 50 Ω impedance of the amplifier with the impedance of the plasma.

4.2   RF IMPEDANCE MATCHING NETWORK

For maximum power transfer, the RF impedance, $Z = R \pm jX$, of the load must equal the complex conjugate of the source impedance. In the case of RF-driven ion sources, the RF power generator is the source with a nominal 50 Ω output impedance, and the plasma generator corresponds the load.
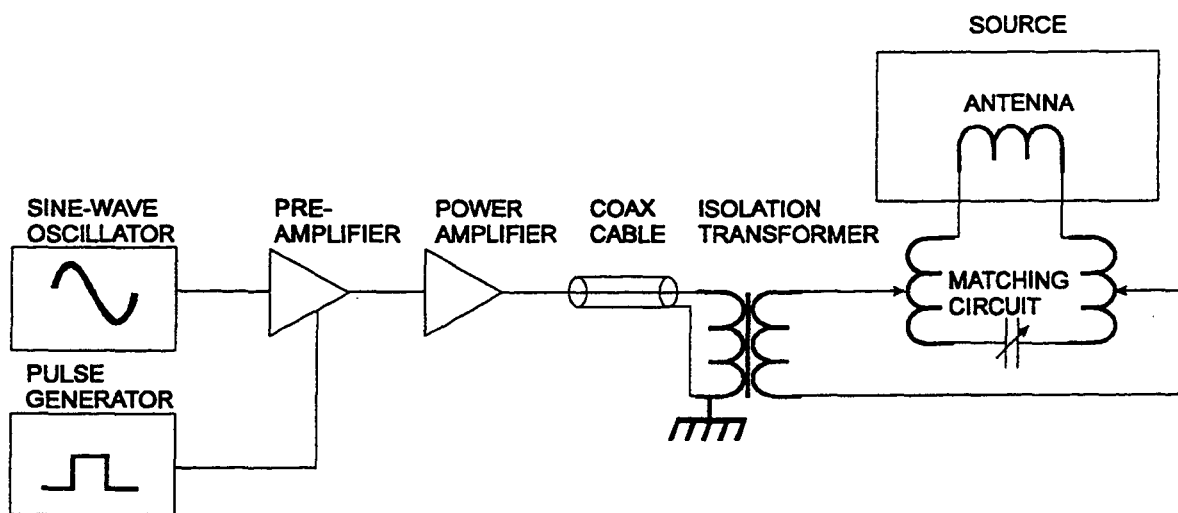
FIGURE 4.3 Schematic diagram of the complete RF power system.

Experimentally, inductively driven discharges have low impedance, on the order of ~ 1 Ω. The matching network is needed between the source and the load in order to match the output impedance of the RF power amplifier to the antenna-plasma load. In the absence of

this impedance match, RF power is reflected back from the load to the source which could cause damage to the RF system.

Fig. 4.3 shows a schematic diagram of the complete RF power system. The RF signal is generated by a digital synthesizer. The signal is sent to a preamplifier, and then to the RF amplifier. The RF power can be controlled by adjusting the amplitude and frequency of the synthesizer signal. This setup is not necessarily true for all RF power systems. Simplified systems which integrate the signal generator, pre-amplifier and amplifier can be found commercially for a 13.56 MHz RF-power supply (Fig. 4.4).

FIGURE 4.4 13.56 MHz RF-power supply used to generate plasma.

The advantages of the RF-driven multicusp source are that there is no cathode lifetime limitation and that the discharge is cleaner than most filament source discharges.

4.3 AXIAL ENERGY SPREAD RESULTS

The axial energy spread measurement for a RF-driven multicusp ion source was performed on a 24-cm-diameter chamber. The filter assembly was positioned at approximately 5 cm from the first electrode. Two antenna configurations (Fig. 4.5), and two different antenna loop diameters (3 cm and 6 cm) were used for the experiment.

a)

b)
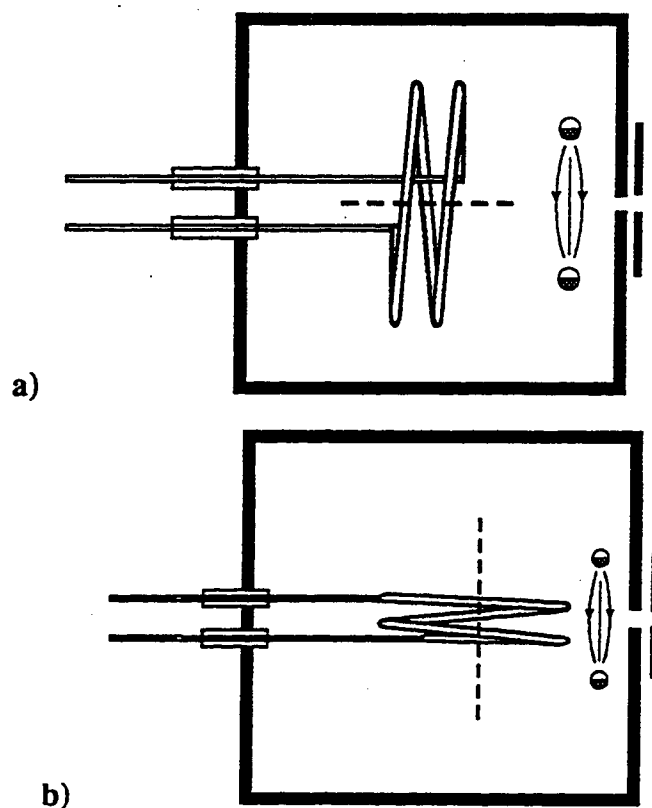
FIGURE 4.5   Antenna configurations are shown above. a) the axis
of the antenna is parallel to the axis of the source, b)
the axis of the antenna is perpendicular to the axis of
the source. The number of antenna loops can be varied
for both cases.
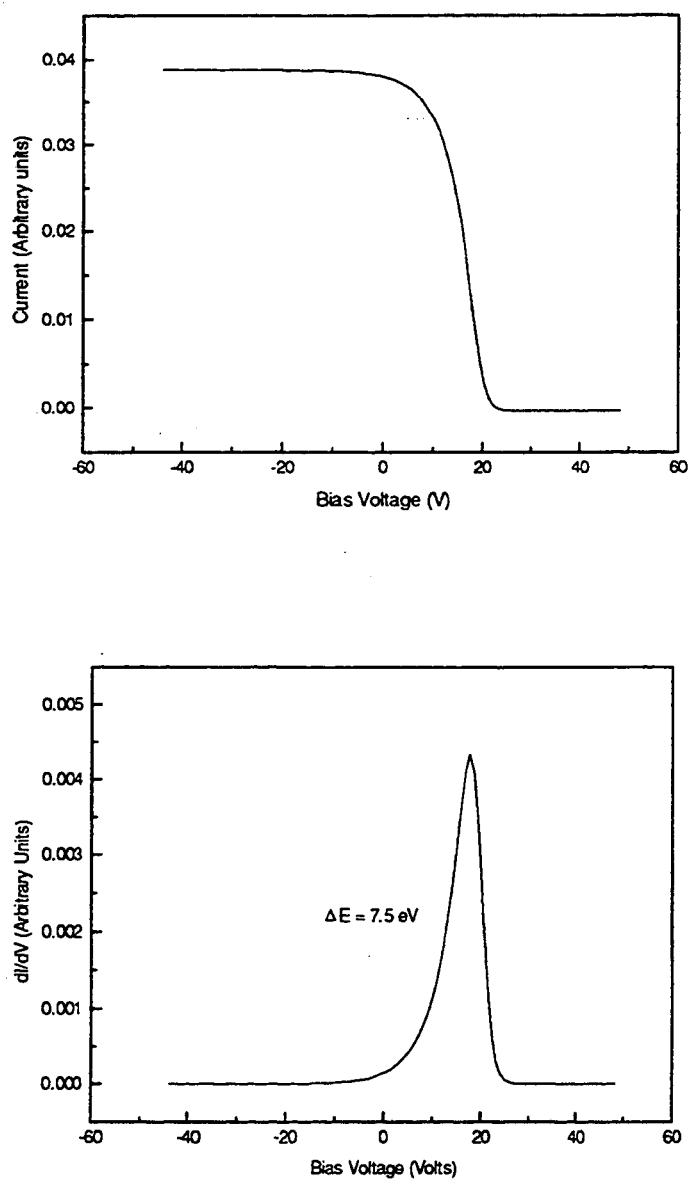
FIGURE 4.6   Two turn antenna (6 cm loop diameter), loop axis parallel to the source axis is shown above a) the measured data and b) the differentiated curve. ΔE is 7.5 eV.

Using a two-turn, 6 cm diameter antenna with the loop axis parallel to the source axis, an average axial energy spread of 7.5 eV was measured, as shown in Fig. 4.6. The

large axial energy spread is due to RF-coupling that causes ionization even in the extraction region. The magnetic filter becomes ineffective, and the energy spread obtained is comparable to the case without the filter for filament discharge operation ($\Delta E = 6.5$ eV, as shown Fig. 3.11).
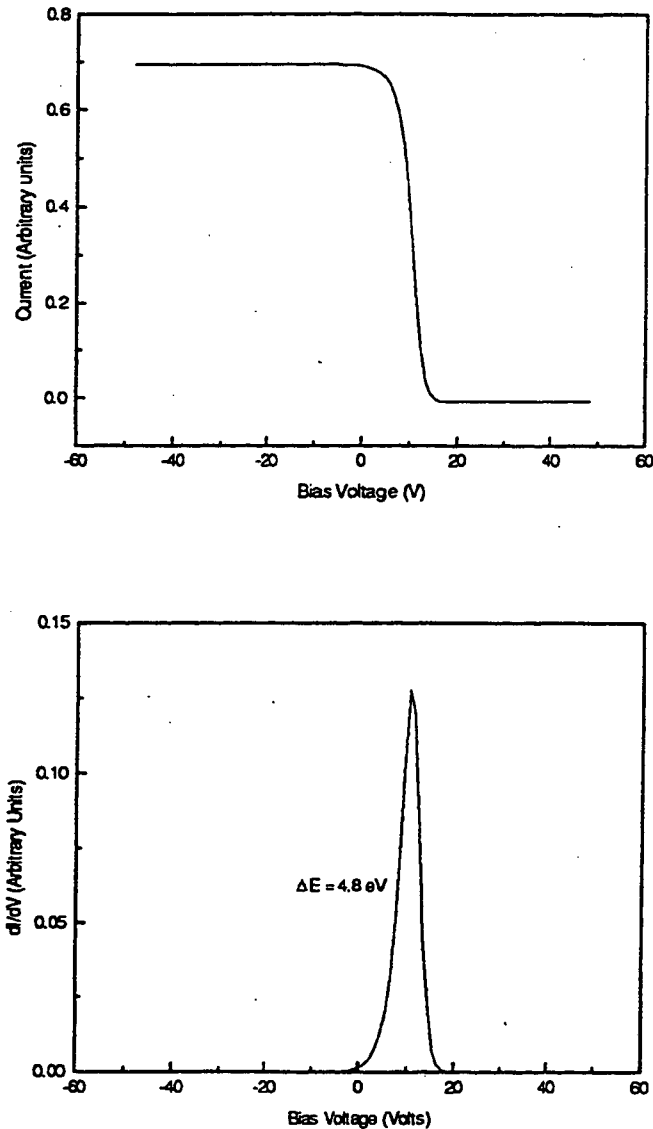
FIGURE 4.7 Two turn antenna (6 cm loop diameter), loop axis perpendicular to the source axis is shown above a) the measured data and b) the differentiated curve. The axial energy spread was found to be approximately 4.8 eV.

When a two-turn, 6 cm diameter antenna with loop axis perpendicular to the source axis was used, the RF-coupling effect was observed to be reduced. The axial energy spread was found to be approximately 4.8 eV, Fig. 4.7.

A single turn antenna with the same geometry as above was also used. The energy spread in this case was found to be approximately 4.7 eV, shown in Fig. 4.8.
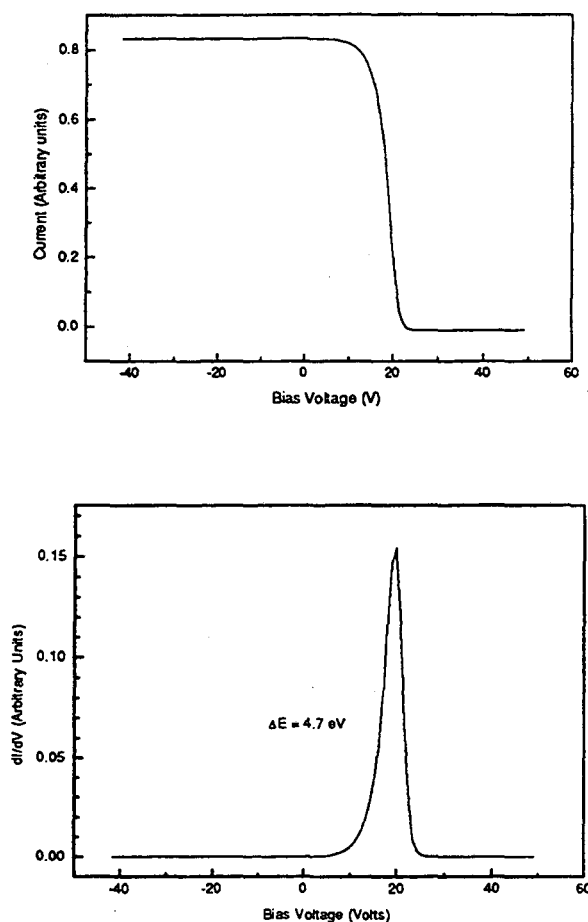
FIGURE 4.8   Single turn antenna (6 cm loop diameter), loop axis perpendicular to the source axis is shown above a) the measured data and b) the differentiated curve. The axial energy spread was found to be approximately 4.7 eV.

Finally, in an attempt to further reduce the RF induction field, the diameter of the single loop antenna was reduced to half, i.e. 3 cm, with the loop axis perpendicular to the source axis. Fig. 4.9 shows a 3.2 eV axial energy spread at 200 W of RF power for this one-turn antenna, showing that the RF induction field in the extraction chamber is indeed further reduced.
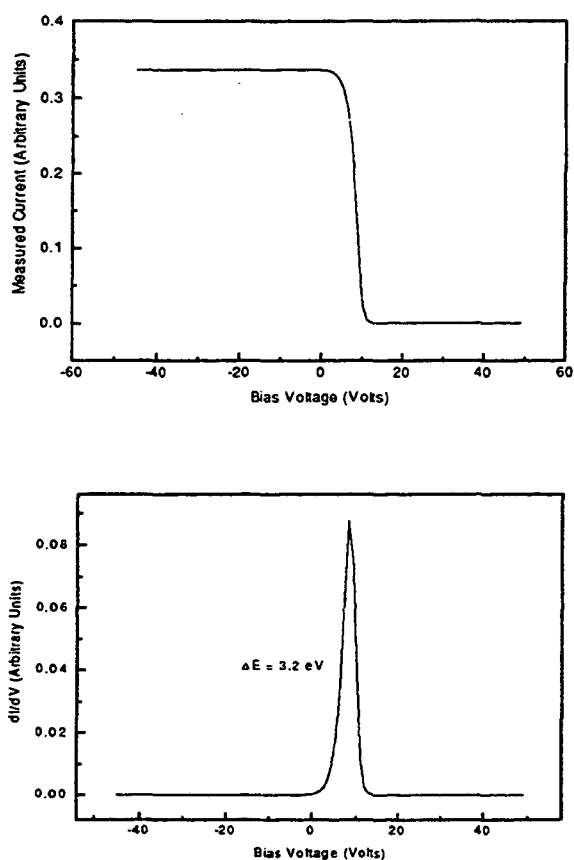
FIGURE 4.9   Single turn antenna (3 cm loop diameter), loop axis perpendicular to the source axis is shown above a) the measured data and b) the differentiated curve. The axial energy spread was found to be approximately 3.2 eV.

In conclusion, the RF-coupling can be reduced significantly by optimizing the orientation and the size of the antenna loop. Reduction in RF-coupling to the extraction region directly translates into a smaller energy spread.

4.4   RF-FIELD PENETRATION IN THE EXTRACTION SIDE OF THE SOURCE

Results of the previous section demonstrated that the axial ion energy spread depends on the antenna geometry which is closely related to RF-coupling. If the RF-induction field penetrates into the extraction chamber, the source behavior is similar to the case without magnetic filter. The presence of the magnetic filter provides a relatively uniform plasma potential distribution along the axis in the source chamber (Fig. 3.6) where ionization takes place. The RF-induction field in the extraction chamber allows ionization to occur, similar to the case without filter.

During ion species measurements for hydrogen, the effect of RF-field penetration into the extraction chamber could be observed from the change in H_2^+ ion concentration. The fraction of H_2^+ species increased with the presence of RF-coupling. The increase in the percentage of the diatomic hydrogen ion is due to a coupling of the RF-induction field beyond the filter plane. As a result electrons are accelerated to high energy which in turn leads to the ionization of the hydrogen atoms.

The B-field of the magnetic filter cannot prevent the generation of energetic electrons (ionizing electrons) in the extraction region where the plasma potential falls off

rapidly. Ions are produced in the source chamber where the V_p is uniform and also in the extraction chamber where the V_p has a larger gradient. As a result, the axial energy spread of the ions becomes large, and the source behavior is similar to the filament discharge operation without filter.

CHAPTER 5

RETARDING FIELD ENERGY ANALYZER FOR ACCELERATED

ION BEAM MEASUREMENT

5.1 ION BEAM GENERATION

In a plasma source, the ions are generated in a discharge chamber. From that point of generation they drift until a fraction of them reaches the extraction region. The extraction process basically consists of applying a high voltage between an ion reservoir and a perforated acceleration electrode.[27] The trajectories of the accelerated ions, which immediately determine the maximum beam quality, are influenced by several factors, such as the applied field strength, the shape of the emitting surface which may be solid (field and surface ionization sources) or flexible (plasma sources), and also on the space charge density of the resulting beam itself. In the case of plasma sources, the emitting surface is commonly termed the **meniscus**. Its detailed shape depends on the electric field distribution due to the applied boundary conditions and the local densities of plasma ions, electrons, and accelerated ions.

The meniscus acts as the boundary layer between the discharge plasma and the accelerated beam particles. The shape and position of this layer, with respect to the surrounding electrodes, depends on the densities of plasma electrons and ions and their mobility which can be expressed in terms of temperatures. Fig. 5.1 shows
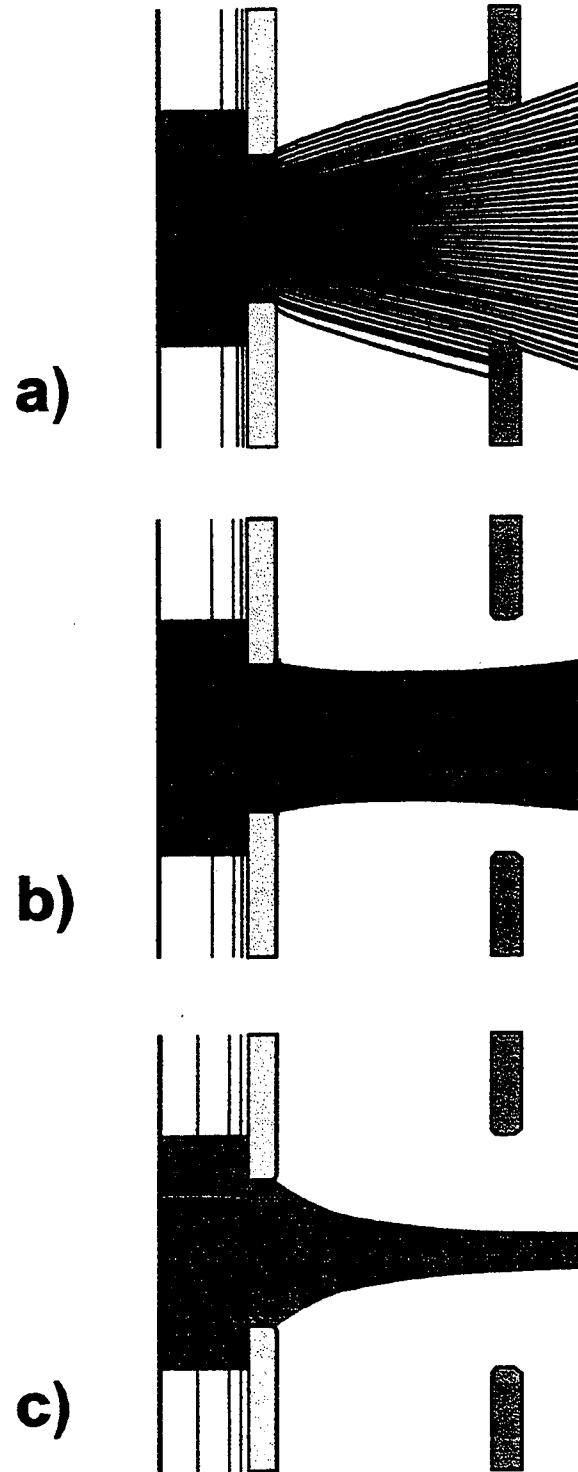
FIGURE 5.1 Three cases of ion extraction from plasma sources. (a) Overdense plasma, (b) intermediate density plasma, (c) underdense plasma.

three cases of ion extraction from plasma sources. The meniscus will be approximately spherical with its center of curvature inside the plasma when the plasma density is relatively high and/or the extraction field is low; nearly planar under optimum conditions; and spherical with the center of curvature outside the plasma when the plasma density is low or, correspondingly, higher extraction field.

Within the extraction gap, the accelerated beam is usually far from being neutral because any electrons that could compensate the positive space charge of the beam particles are accelerated backward by the extraction field to much higher velocities than the ions, thus, their own space charge is diluted. After an intense beam has passed the extraction electrode, its space charge has to be compensated; otherwise severe blowup of the beam envelope would occur.

In many cases some of the residual gas particles that are present in the accelerator will be ionized by impinging beam ions, and this process can generate a sufficient number of compensating electrons. However the electrons must be kept from being accelerated back into the source by the extraction field. This shielding can be achieved by means of a so-called accel-decel system where a screening, or suppresser electrode is introduced into the main extraction gap. The suppresser electrode is biased to a sufficiently low potential so as to create a negative potential well and thus form a backstreaming electron barrier. In Fig. 5.2, an example of an accel/decel system is shown. A more complicated accelerator system can be used for other applications. Fig. 5.3 shows the picture of a low energy beam transport (LEBT) system designed with the capability for beam steering.[28]
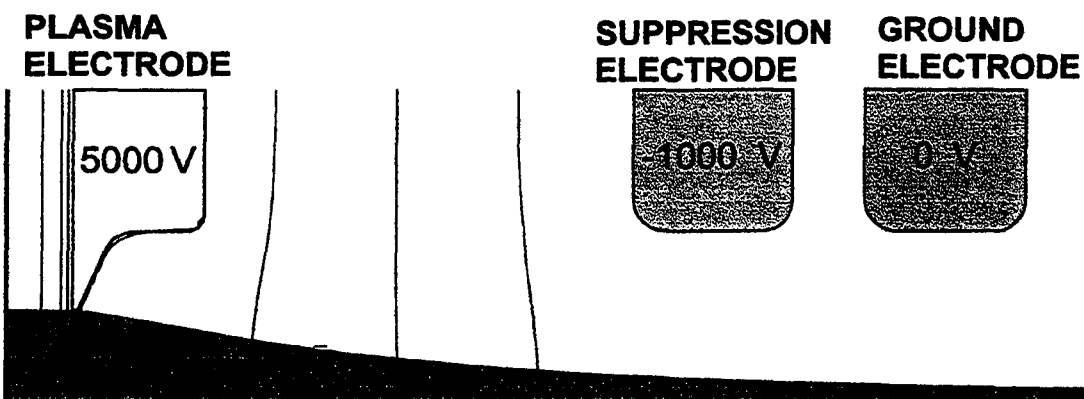
FIGURE 5.2 Example of an accel/decel extraction system with equipotentials and ion beam trajectories. Calculation was performed on IGUNE code. [29]
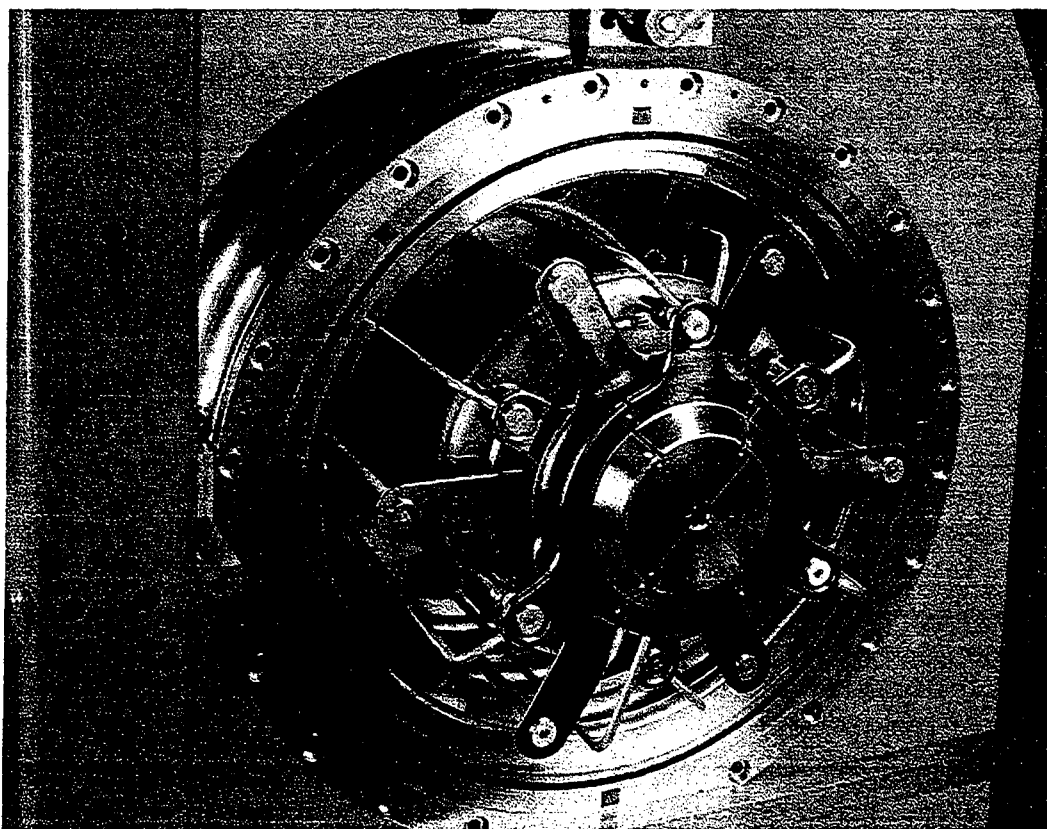
FIGURE 5.3 Low energy beam transport system with splitting electrodes for beam steering.

The maximum current density that can possibly be expected for any charged particle species accelerated by an electric field is obtained under space-charge limited conditions and follows the Child-Langmuir law,

$$j = \frac{4}{9}\varepsilon_0 (\frac{2q}{m_i})^{1/2} \frac{V^{3/2}}{d^2}$$

(Eq. 5.1)

where j is the ion current density, q is the ion charge, m_i is the ion mass, V is the applied voltage, and d is the extraction gap width, and ε_0 is the permissivity constant. This equation is valid under space-charge limited conditions, that is, when the plasma generator is producing more ions than are removed in any given time.

5.2   TRIODE SYSTEM FOR ION PROJECTION LITHOGRAPHY

A three-electrode extraction system was designed by Ion Microfabrication Systems (IMS, Vienna, Austria) to be used for the ion projection lithography machine. Ions are accelerated through a hole of 0.6-mm-diameter with an energy of 15 kV. The second electrode is electrically biased at -1 kV for electron suppression, and the last electrode is connected to ground. The beam is extracted under an underdense condition shown in Fig. 5.4. The beam has a cross-over near the plasma electrode. The acceleration system is designed for an expanding beam and only a small portion (~10 %) of the accelerated beam is employed in the process. This expanding beam design with a cross-over is not very

sensitive to changes in ion current density. A more detailed discussion of the accelerator system will be found in Chapter 8.

a) $\overline{5\ mm}$

b) $\overline{0.5mm}$
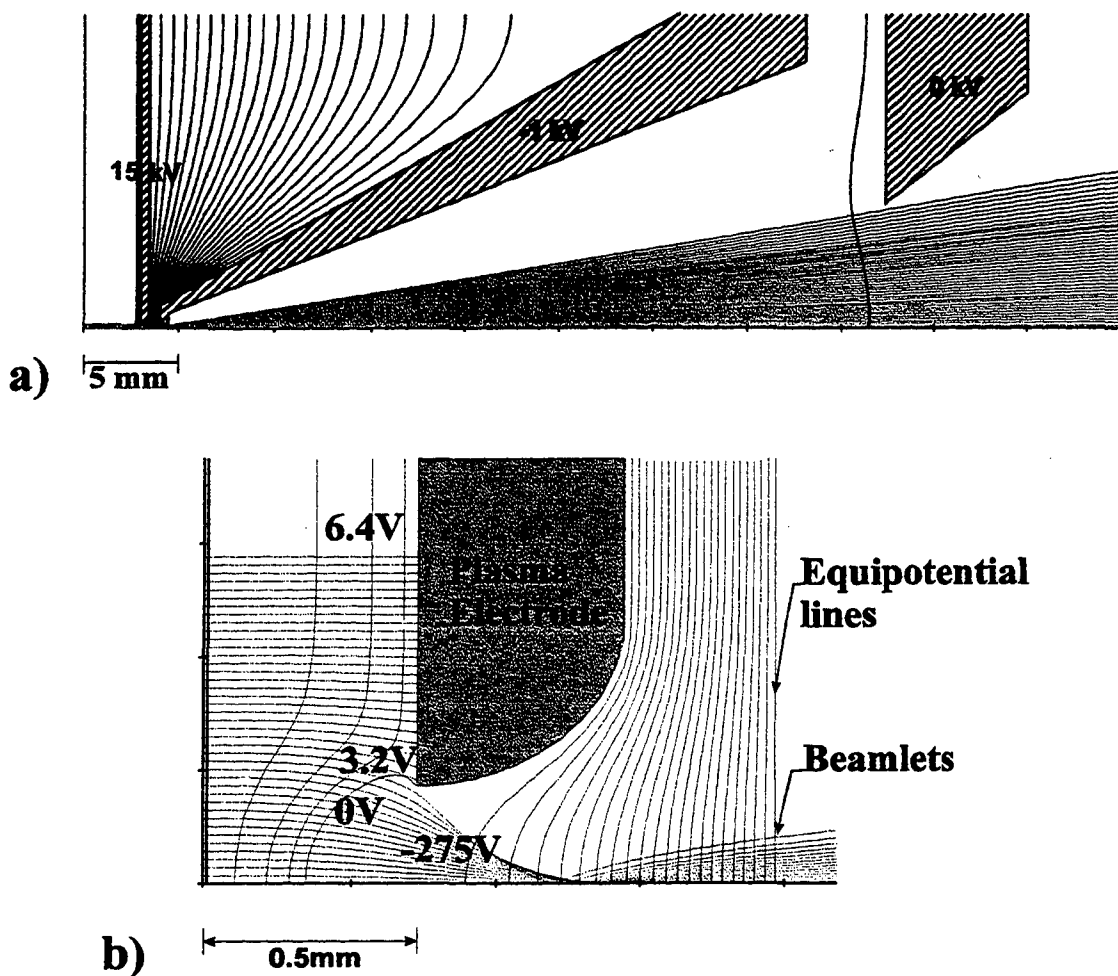
FIGURE 5.4 a) The accelerated beam has a cross-over right after the plasma electrode. Calculation was performed on IGUNE code. b) Expanded view of the plasma electrode region with the cross-over. The voltage values are relative to the plasma electrode.

5.3 RETARDING FIELD ENERGY ANALYZER

A method of obtaining the longitudinal or axial energy spread of the ions consists of using a retarding field energy analyzer. The principle is similar to the energy analyzer

described in previous chapters, except the ions are extracted from the quasineutral plasma. For the accelerated beam, the influence of electrons from the plasma on the measuring device is non-existent.

A schematic for the retarding field energy analyzer is shown in Fig. 5.5, and the picture of the device is shown in Fig. 5.6. The special design of the energy analyzer avoids problems caused by energetic ions of few kilovolts from hitting the collector where the energy analysis takes place. Second, it minimizes the influence of the ripples of the power supply because the collector is electrically connected to the potential of the source.
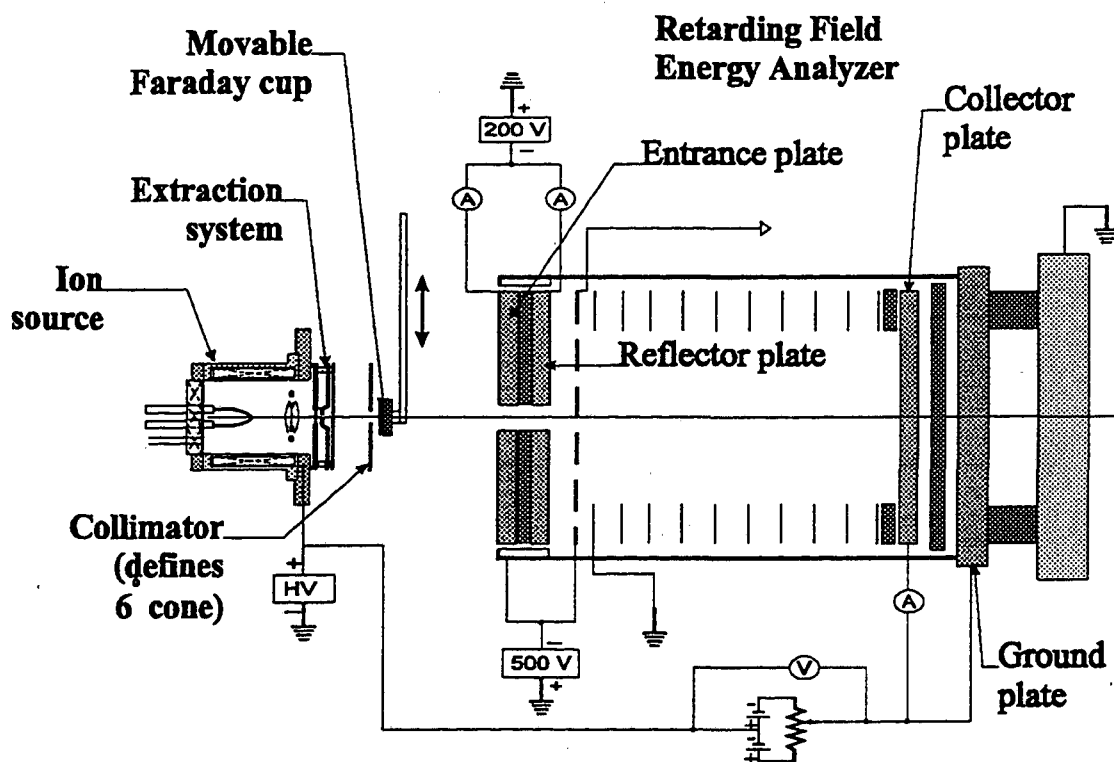
FIGURE 5.5 Schematic of the retarding field energy analyzer setup for measuring the axial energy spread of accelerated beam. It includes the ion source, collimator and a movable faraday cup.
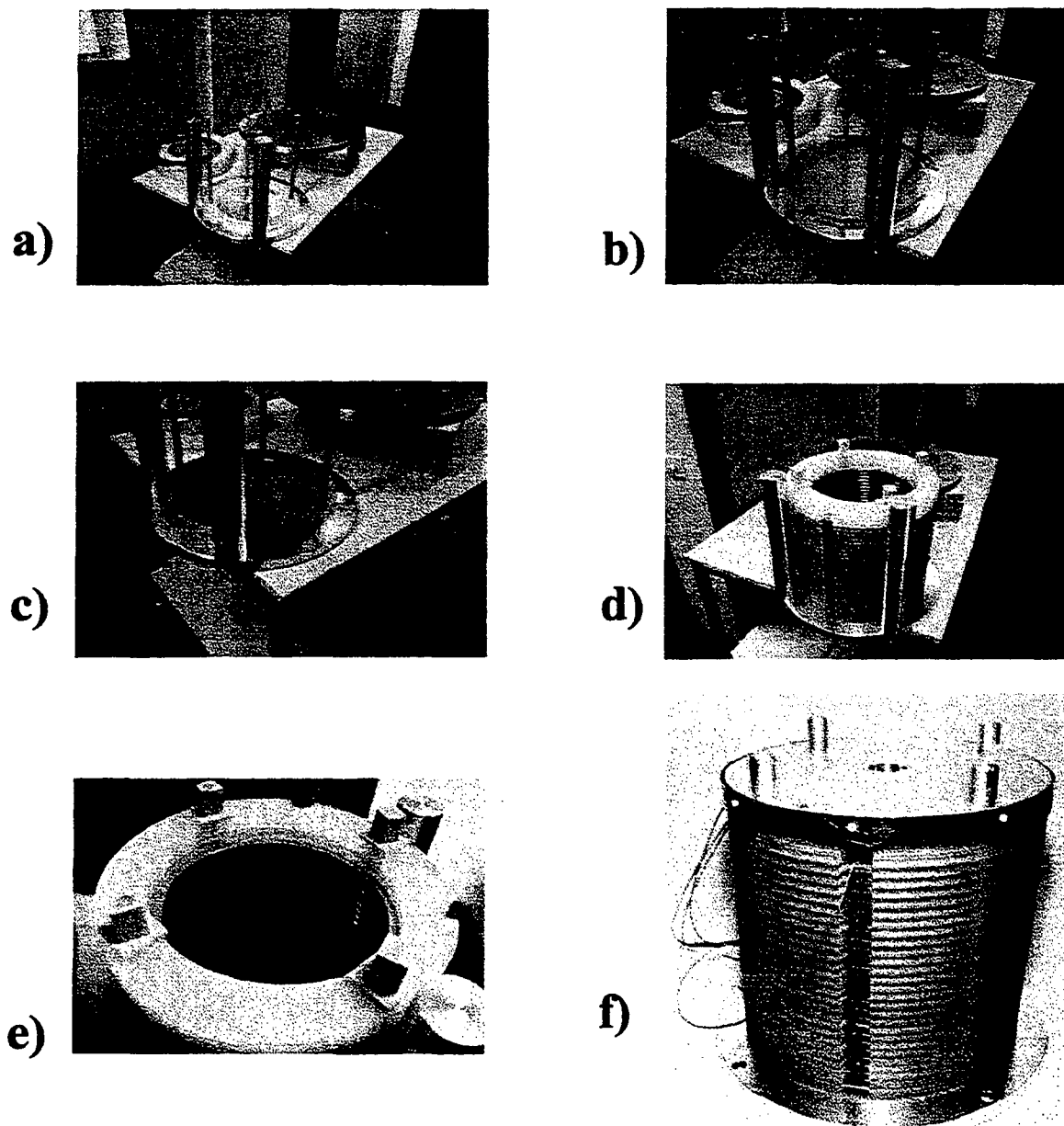
FIGURE 5.6 Picture of the retarding field energy analyzer at different building stages. **a)** High voltage ground plate is placed at the bottom and alignment devices are placed for later additions. **b)** The analyzer plate is added. **c)** Electrode rings are connected will provide smooth electric field lines at the center. **d)** Spacers are placed between the electrodes. **e)** A fine mesh grid is placed before the reflector plate and the entrance plate. **f)** The final assembled energy analyzer.

As shown in Fig. 5.5, the collector plate is biased at the same potential as the ion

source. A homogeneous electric field is generated inside the analyzer chamber whose

direction is opposite to the ion beam trajectories. Energy analysis of the ions in the beam is

accomplished by adjusting the potentiometer (P). To be able to measure the true axial

energy spread of the accelerated ions, the beam has to be collimated well enough such that

only a parallel portion of the beam is analyzed. As shown in the figure a collimator was

placed in the setup in order to accomplish this limit.
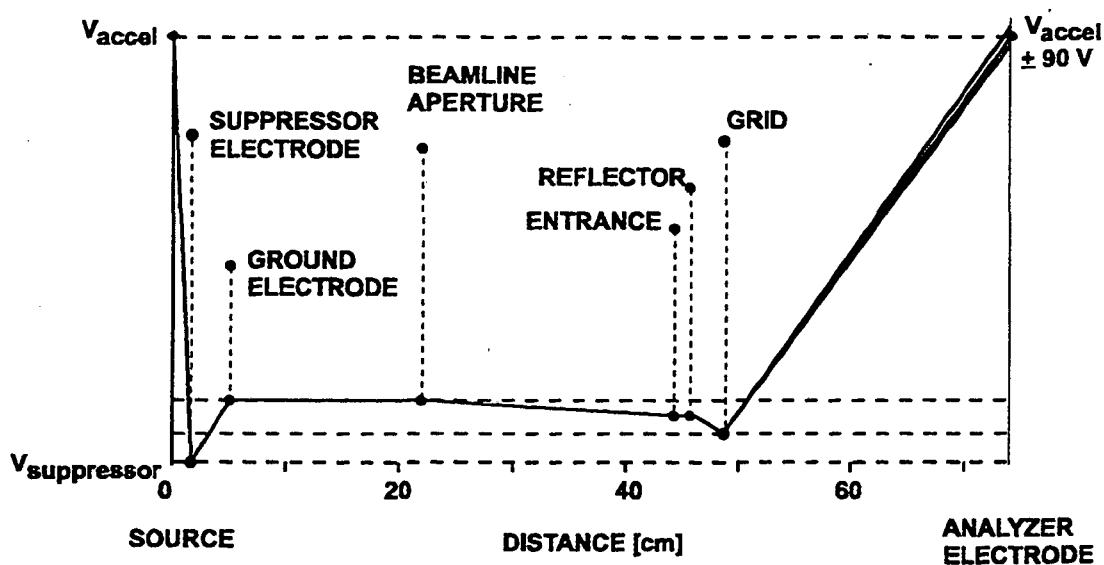
FIGURE 5.7 Potential diagram of the setup.

Fig. 5.7 shows a potential diagram as the ion leaves the source and reaches the

collector. The entrance plate and the reflector plates are biased (-250 V) in order to

prevent secondary electrons from entering the system. Fine tungsten wires (approximately

0.001" in diameter) were used to form a grid which was placed after the reflector plate.

The spacing between grids is approximately 1 cm. The grid is biased even more negative

than the reflector plate (-500 V) to further electron suppression. A small power supply or

battery is connected to the collector and small changes in potential with respect to the plasma source can be applied for ion discrimination.

When the collector is biased slightly more negative than the reference then the ions are reflected back and can be recorded on the reflector plate. Thus, the energy spread measurement can be done either on the collector plate or the reflector plate. In either case, it has been demonstrated that the results are comparable.

5.4   FILAMENT DISCHARGE SOURCE RESULTS WITH FILTER

The ions are extracted from the source with an acceleration voltage of 7 kV. The axial energy spread of the positive hydrogen ion beam from the 20-cm-long ion source was measured at pressures that ranged from 2 to 10 mTorr. The discharge voltage was kept constant at 80 V, but the discharge current could be varied by adjusting the cathode emission.

Fig. 5.8 shows the axial energy spread as a function of the discharge current, measured at the collector plate (the ion energy spectra at the collector and the reflector plates are consistent). It can be seen that the axial energy spread increases as the discharge current increases.[30] At a discharge current of 1 A, the axial energy spread for the 20-cm long source was measured to be 1.2 eV. At a discharge current of 9 A, the energy spread was 3.3 eV. Space charge effects outside the source could be the cause of the change since the extraction system was designed for an expanding beam with a cross-over as illustrated in Fig. 5.4b. Computer simulation indicates that the cross-over is insensitive to small changes of current density.
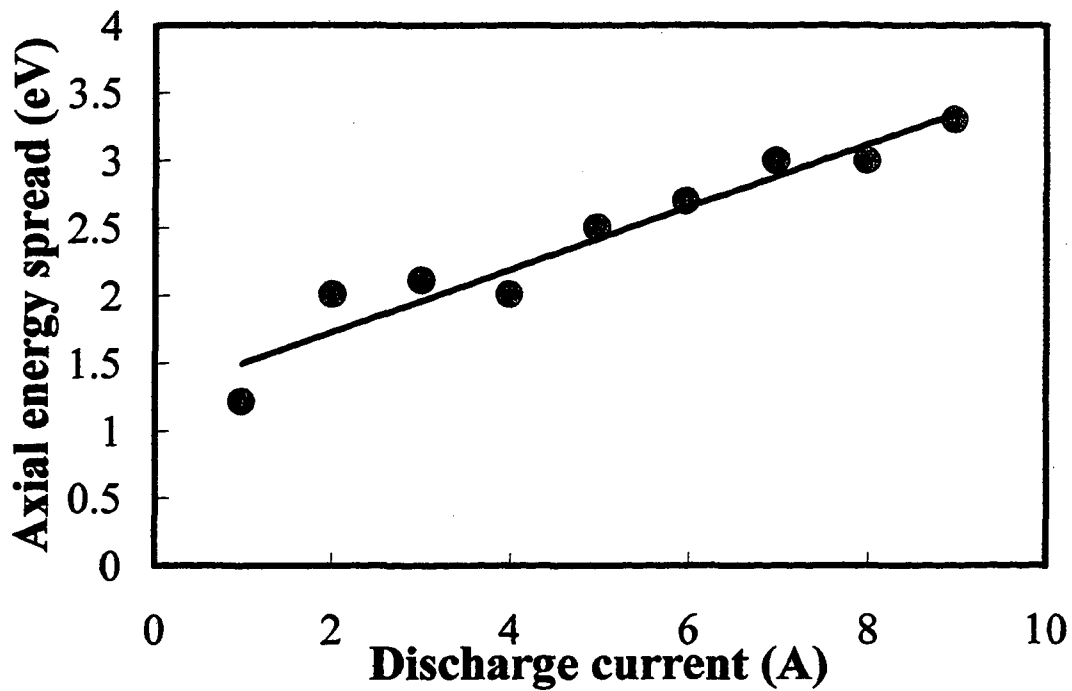
FIGURE 5.8 Axial energy spread as a function of the discharge current, measured at the collector plate for the 20-cm long source. Source pressure is 8 mTorr.

Fig. 5.9 shows that the energy spread decreases when the gas pressure of the source increases. At a discharge current of 8 A, the energy spread decreases from 3 eV at 2 mTorr to 2.1 eV at 10 mTorr. The presence of neutral gas particles in the extraction system can reduce the space charge effect by providing the background electrons in the drift space, thus lowering the energy spread.
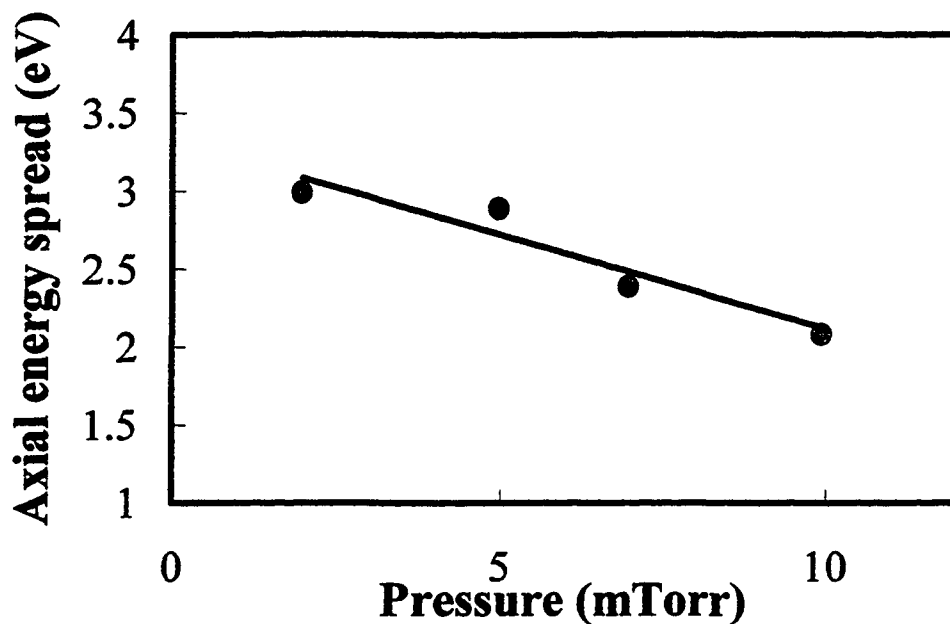
FIGURE 5.9 Axial energy spread as a function of pressure for the 20-cm-long source. Discharge current is 8A.

Similar results on the ΔE measurements were obtained for the 10-cm long source. At a discharge current of 10A and a pressure of 8 mTorr, the energy spread of the extracted beam was found to be 2.3 eV. In general, the energy spread results for the 10-cm-long source were consistent with those in the previous Chapter.

5.5 RF-DRIVEN SOURCE RESULTS WITH FILTER

Initially, the axial energy spread of the RF-driven multicusp ion source has been measured with the RF power supply operated at ground potential. Voltage isolation is obtained by using a transformer with sufficient insulation in the matching circuit. The

axial ion energy spread for the RF source has been found to be greater than 100 eV. It is very large compared to the measured values of 2 to 3 eV for filament discharge cases. This measured energy spread is comparable to the values that have been reported by Zackhary[31] and Olthoff, et. al [32].

The large axial energy spread of the RF-source may have been due to the RF voltage coupling to the extraction voltage, and thus resulting in a modulation of the beam energy. The RF modulation has been eliminated through the following steps. Problems associated with ground loops between the measurement devices and the data acquisition circuits have been minimized with the use of fiber optics for electrical isolation and with longitudinal chokes (neutralizing transformers). Longitudinal chokes are used to eliminate longitudinal currents within the ground loop, while having an insignificant effect on the signal current.

The axial energy spread is reduced to approximately 47 eV when the RF-power supply is installed at the high voltage platform, so that it is operated at the same potential as the ion source, as shown in Fig. 5.10. The ion energy distribution is shown in Fig. 5.11a. This measured curve is fitted with a polynomial function. The corresponding differentiated curve (shown in Fig. 5.11b) shows two peaks similar to those as previously reported by Zakhary [31]. These two peaks are clearly due to the RF-coupling to the high voltage which causes fluctuation in the beam energy.
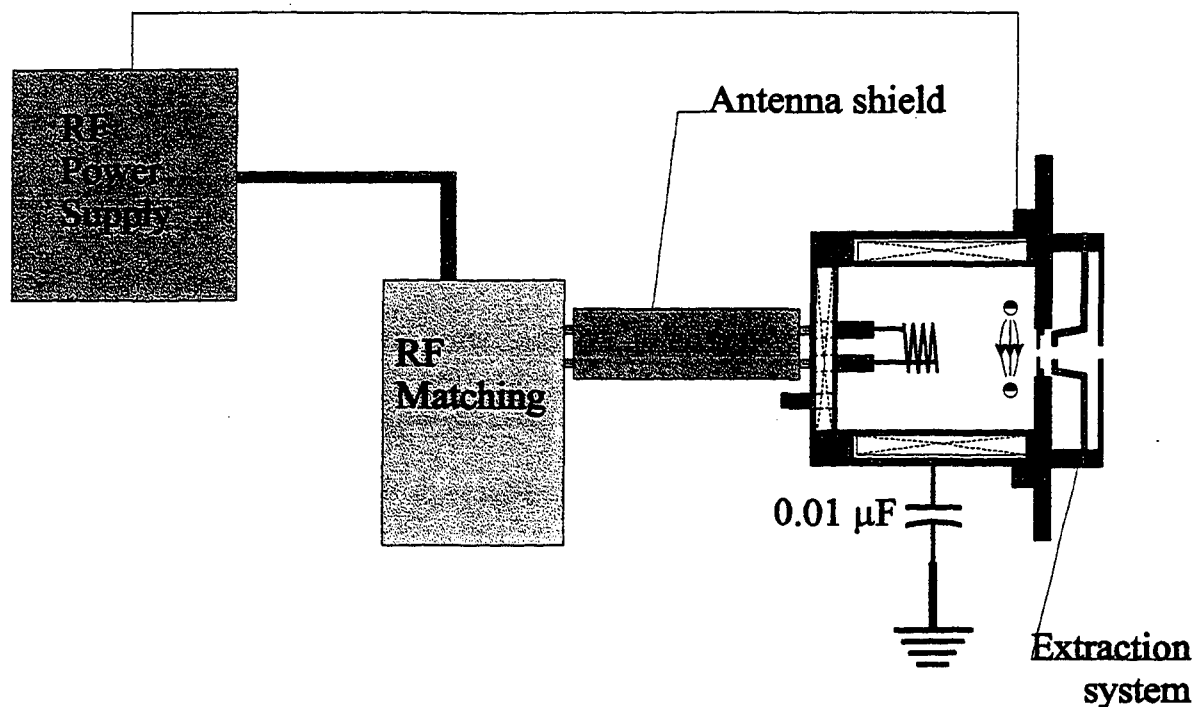
FIGURE 5.10 The rf-matching and power supply was raised to high
potential. The leads between the matching network
and the induction coil can be shielded completely, as a
gap between the matching network and the source is
no longer required.

The axial energy spread is further reduced by shielding the leads between the

matching network and the induction coil. Operating the RF-power supply at the extraction

potential enables complete shielding of the leads between the matching network and the

induction coil. A voltage isolator between the matching network and the source is no

longer required. With this modification, the axial energy spread is found to be reduced

dramatically, from 47 eV to 3.2 eV. The I-V characteristic curve which shows only a

single peak, as illustrated in Fig. 5.12, has been fitted with a function to find the energy

spread because there are still some modulations in the measured data.
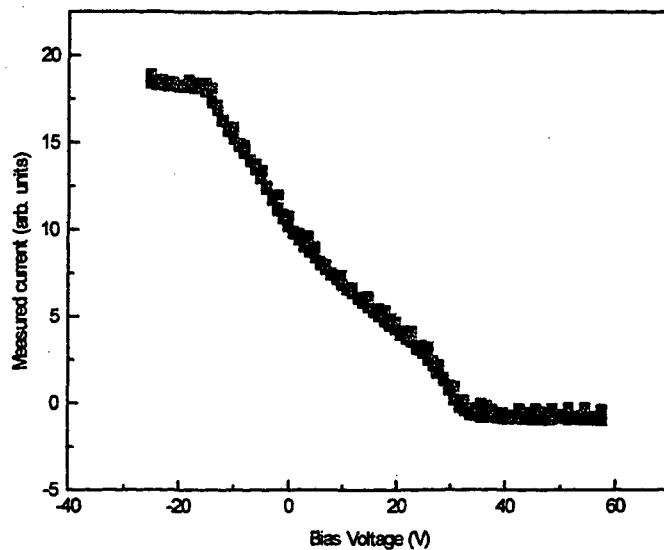
a)
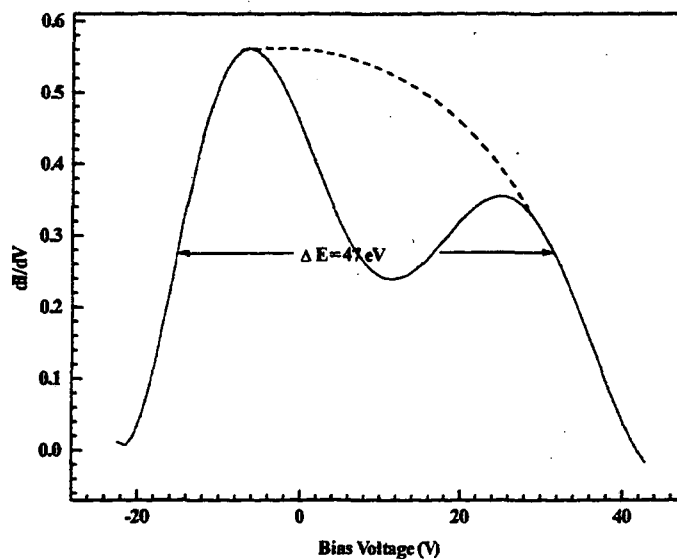
b)

FIGURE 5.11 a) The I-V characteristic curve when the rf power supply is raised to a high voltage platform. The antenna leads are not shielded and no capacitors are used. **(b)** The I-V characteristic curve in (a) has been differentiated to obtain the energy distribution. Two peaks can be observed due to the rf modulation of the extraction. The resulting axial energy spread was approximately 47 eV.
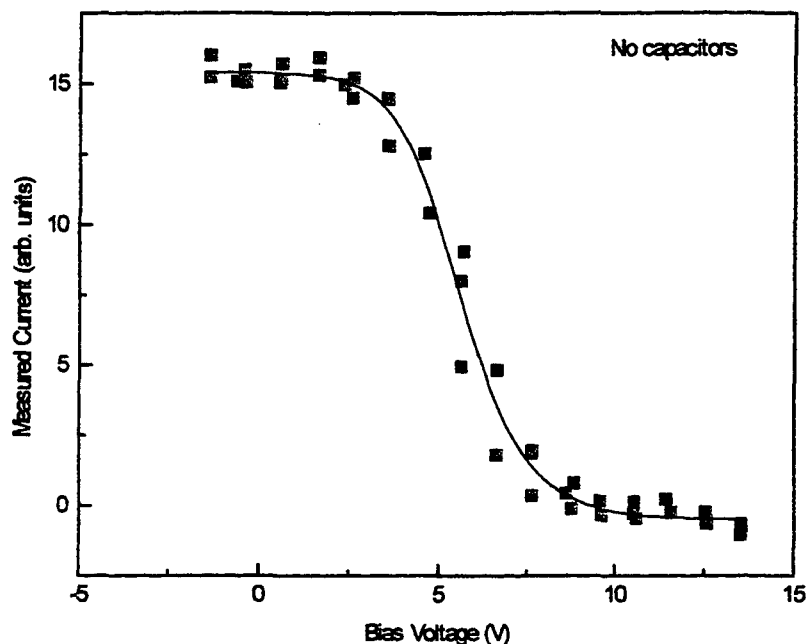
FIGURE 5.12 The I-V characteristic curve when the antenna leads
are shielded, but without using capacitors.

In an attempt to further reduce the RF-coupling to the extraction voltage,
capacitors have been used. The previously observed modulation of the extraction voltage
is minimized by connecting capacitors from the source chamber to ground. These
capacitors function essentially as a low-pass filter, largely eliminating the modulation of
the dc acceleration voltage with RF-interference. The value of the capacitor used is
$0.01\mu F$. After connecting the capacitors between the high voltage to ground, the axial
energy spread is still found to be 3.2 eV. However, as shown in Fig. 5.13, the I-V
characteristic curve is cleaner without fluctuation seen in Fig. 5.12. Even at an RF-power
of 1 kW, the axial energy spread is approximately 3.6 eV. The energy spread found for

the RF-driven source is comparable to the filament discharge source for comparable input

power[33], as shown in Fig. 5.14.
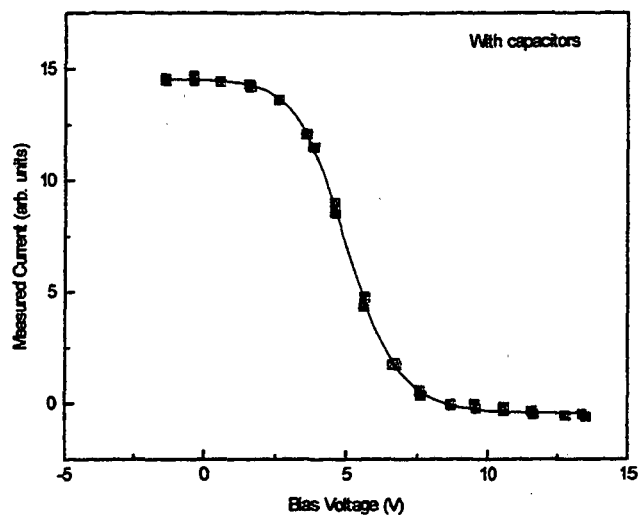
a)
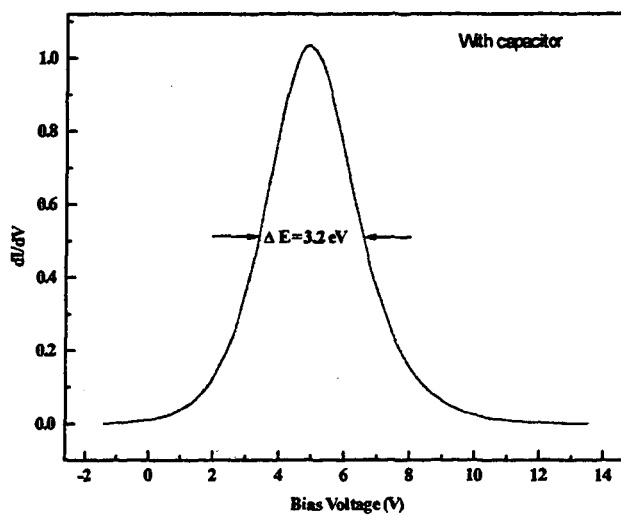
b)

FIGURE 5.13 a) The I-V characteristic curve was obtained when capacitors were added (with the antenna leads shielded). (b) The curve in (a) has been differentiated to obtain an axial energy spread of approximately 3.2 eV.
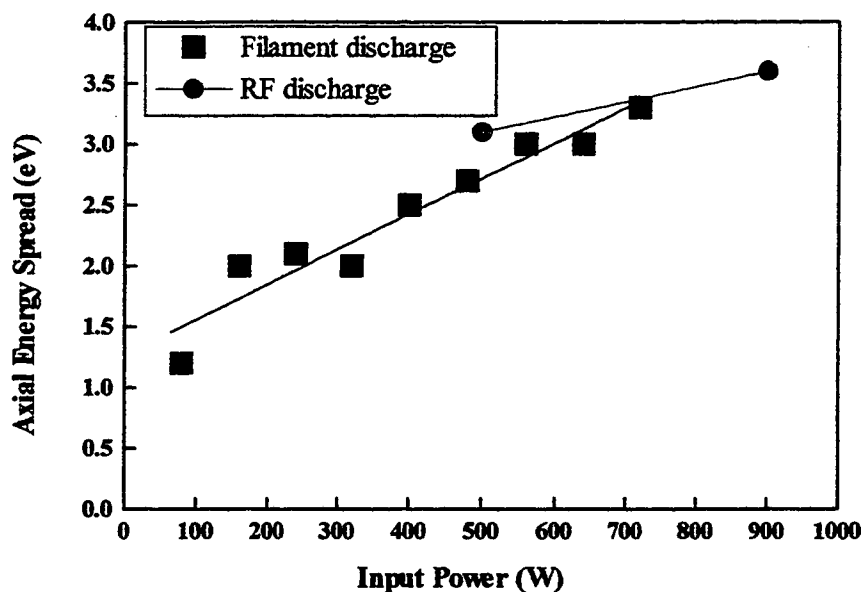
FIGURE 5.14 Energy spread for the rf-driven source is comparable
to that of the filament discharge source.

The axial energy spread of the RF source without the magnetic filter has also been
measured. It is found to be approximately 5.6 eV at an RF-power of 1 kW. The presence
of the magnetic filter reduces the axial energy spread in the RF-driven source in the same
manner as in the filament dc discharge multicusp source.

5.6   SOURCE PERFORMANCE ON AN ION PROJECTION LITHOGRAPHY
MACHINE

Thus far, it has been proven that low axial energy spread ion beams can be
obtained with a multicusp ion source. The source was tested in an ion projection
lithography (IPL) machine. In IPL, projection of sub-0.13 μm patterns from a stencil

mask onto a wafer substrate is required for semiconductor fabrications. In order to maitain the chromatic aberrations to a minimum, an ion source which delivers a beam with an energy spread of less than 3 eV is required.
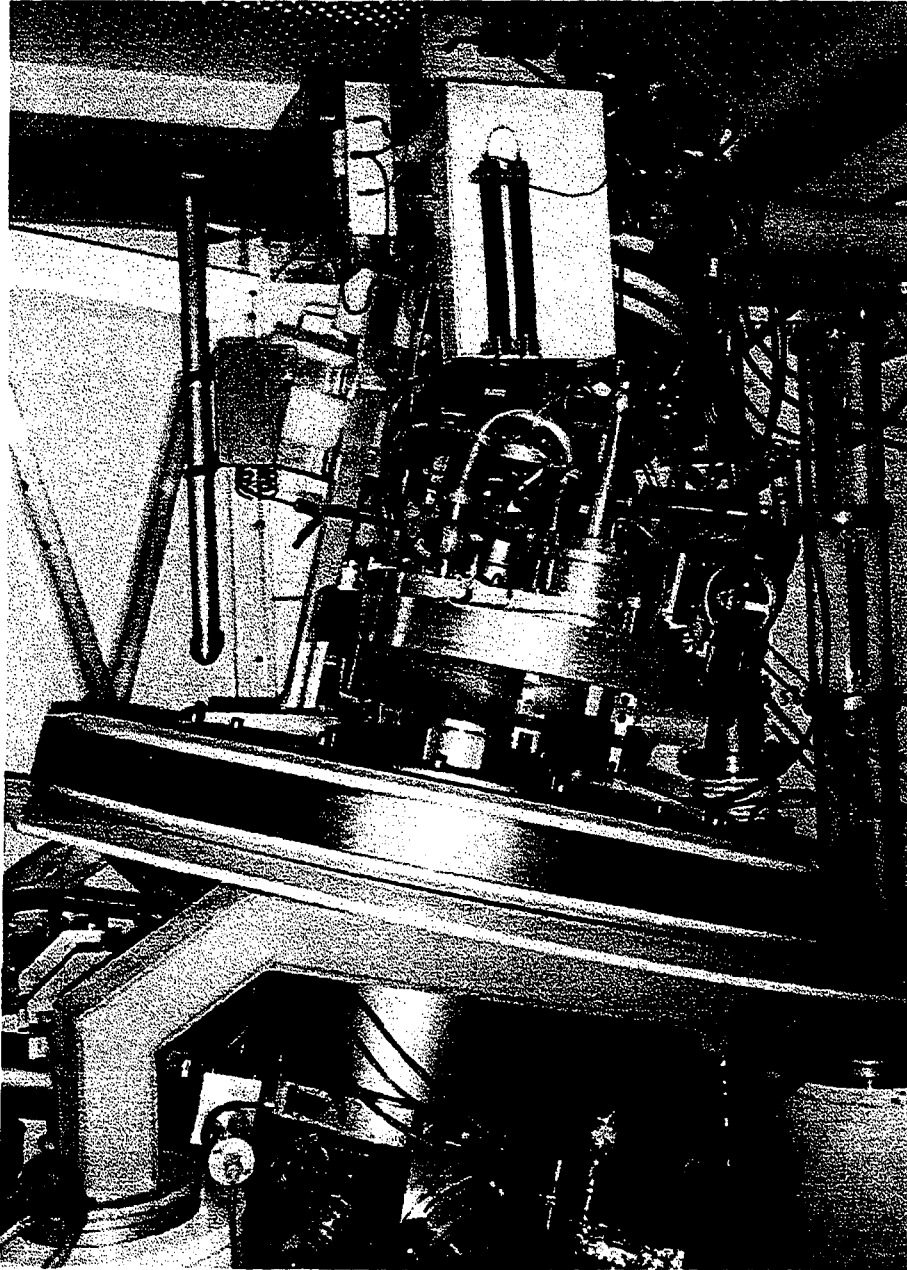
FIGURE 5.15 Ion projection lithography machine in Berlin.

There are currently two IPL machines in the world, only one of these is operational. The machine is located in the Fraunhofer Institute in Berlin (Fig. 5.15). In this system, a duoplasmatron was used to produce the ions. Duoplasmatrons have a measured energy spread of approximately 10 eV. Recently, the filament driven multicusp source replaced the duoplasmatron and the result was very encouraging. Fig. 5.16 shows the two different sources next to each other. A picture of a representative stencil mask used in IPL is shown in Fig. 9.4. This 6" IPL stencil mask has a membrane 120 mm of diameter with a thickness of 3 µm. The stencil pattern is a 7 x 7 array.

FIGURE 5.16 Two ions sources: duoplasmatron (left), multicusp source (right)
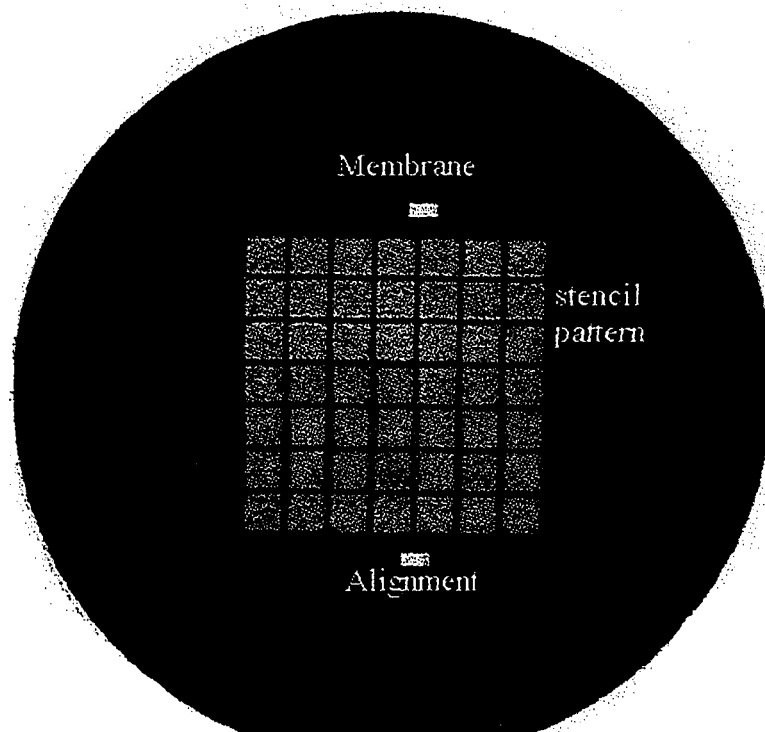
FIGURE 5.17 6" IPL stencil mask. The membrane is 120 mm in diameter with a thickness of 3 μm. The stencil pattern is a 7 x 7 array.

Fig. 5.18 shows pictures of the projected image on the substrate. The feature size in this case is 60 nm. The image shown in Fig. 5.18a is a bit distorted and such distortions are also noticeable with a tilt of the viewing angle as shown in Fig.5.18b. After replacing the duoplasmatron with the multicusp source the exposure process was repeated under the same conditions as with the previous source. The resulting image is much sharper then the previous run (Fig. 5.19). This confirms indeed the importance of energy spread in reducing the aberration.
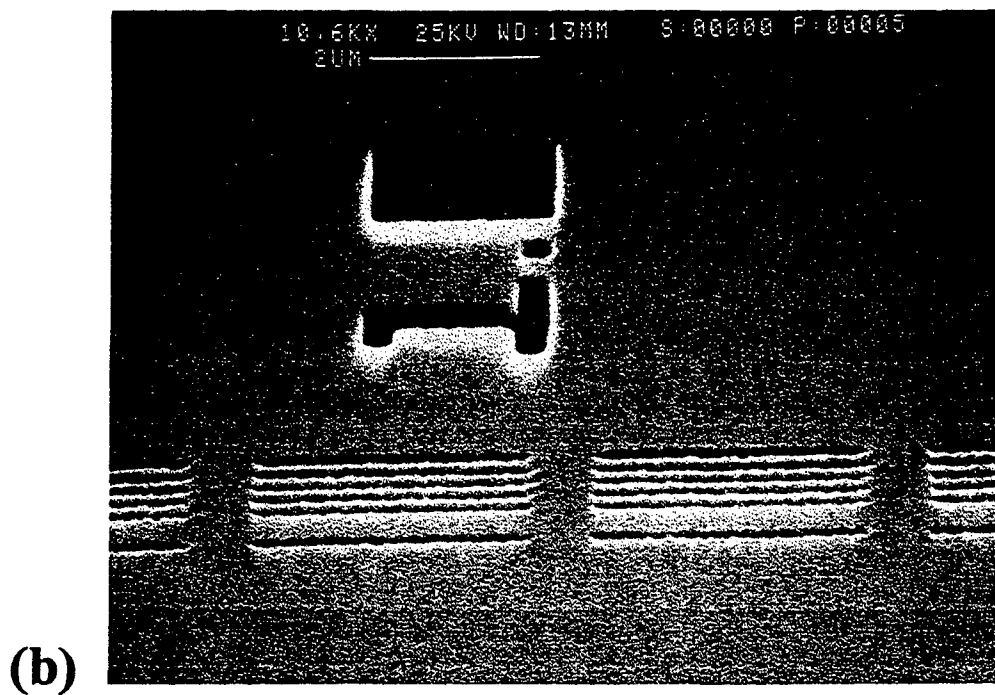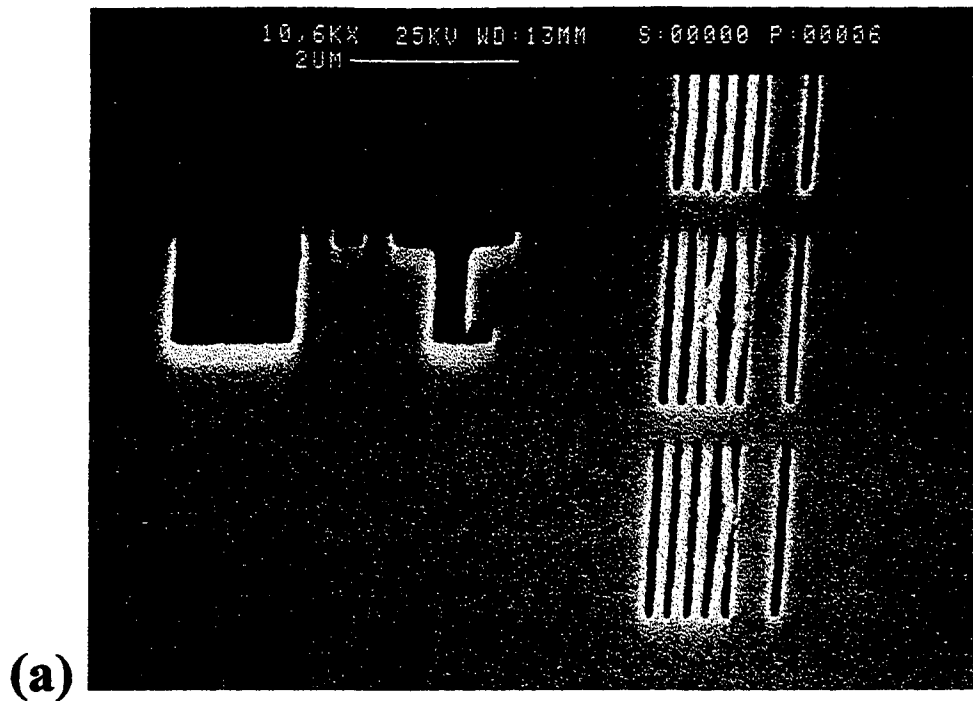
FIGURE 5.18 Exposed image is from an 8.4 reduction system using a duoplasmatron ion source. Image is 60 nm lines. **(a)** top view.**(b)** 50° tilt.
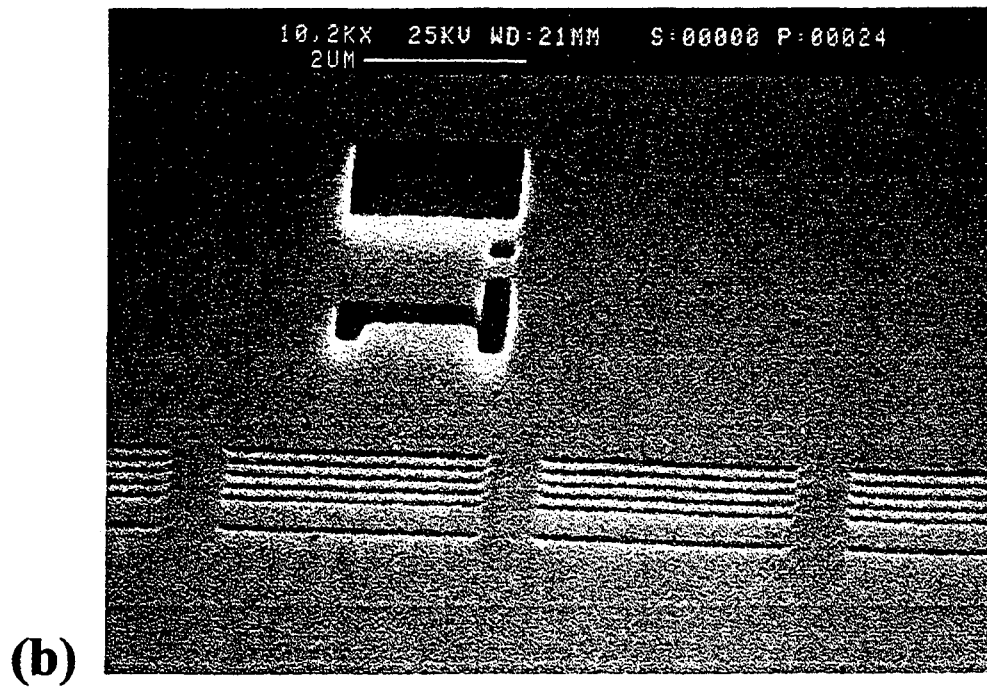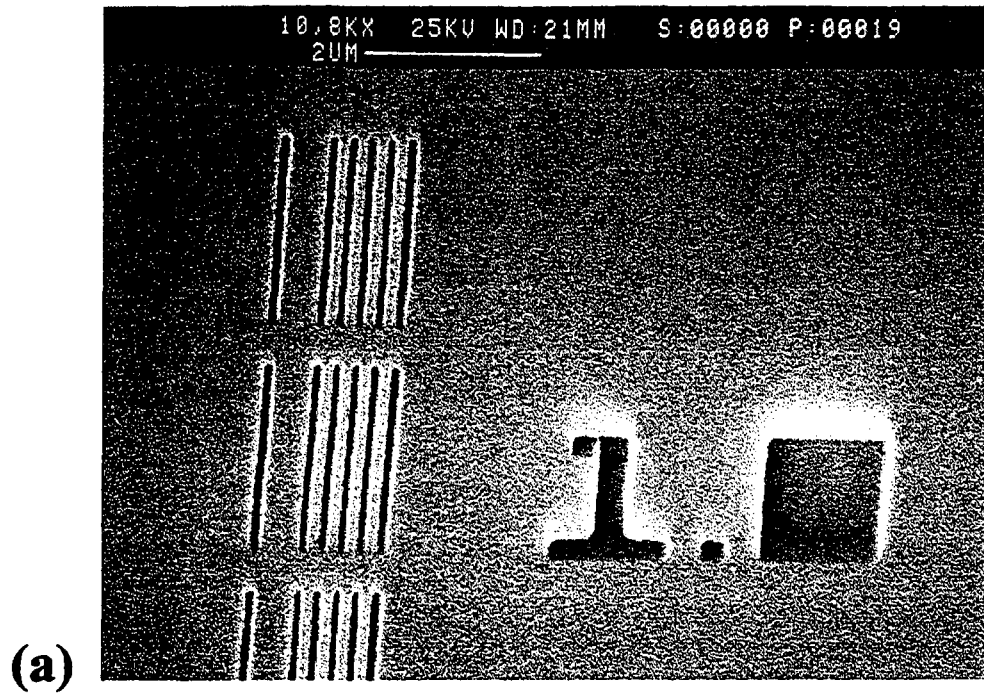
FIGURE 5.19 Exposed image is from an 8.4 reduction system using a multicusp source. Image is 60 nm lines. (a) top view. (b) 50° tilt.

In later chapters a scheme will be presented where energy spread is further reduced. With this modified multicusp source arrangement, the result is expected to be superior than ever before.

CHAPTER 6

MAGNETIC ENERGY ANALYZER FOR ACCELERATED ION

BEAM MEASUREMENT

6.1   EXPERIMENTAL SETUP

The Chapters 4, 5 and 6 of this dissertation describe two different techniques for ion energy spread measurement. A third method to confirm the axial ion energy spread consists of using a magnetic energy analyzer shown in Fig. 6.1. Energy spread measurements of a compact multicusp ion source (8 cm long by 2.5 cm diameter) have been performed with this magnetic energy analyzer. Sixteen samarium-cobalt magnets were spaced evenly around the exterior of the source chamber housing. The ion source was air cooled; two sets of air blowers, not shown in the figure, were used for this purpose.[34]

Unlike the electrostatic retarding field analyzers, the magnetic energy analyzer can be used to measure energy spread of the extracted (i.e. accelerated) beams for the various positive ion species as well as H^- ions. It can also be used to measure the hydrogen ion species distribution by comparing the heights of the three hydrogen ion species (H^+, H_2^+, H_3^+) signals.

The extraction system used for the mass analyzer and the extracted beam experiments, consists of two electrodes. The first electrode is connected to the source chamber wall which is biased at a positive high potential and the second is electrically

grounded. The accelerated beam is collected by a graphite Faraday cup. A pair of permanent-magnets is installed at the cup entrance in order to suppress secondary emission electrons.
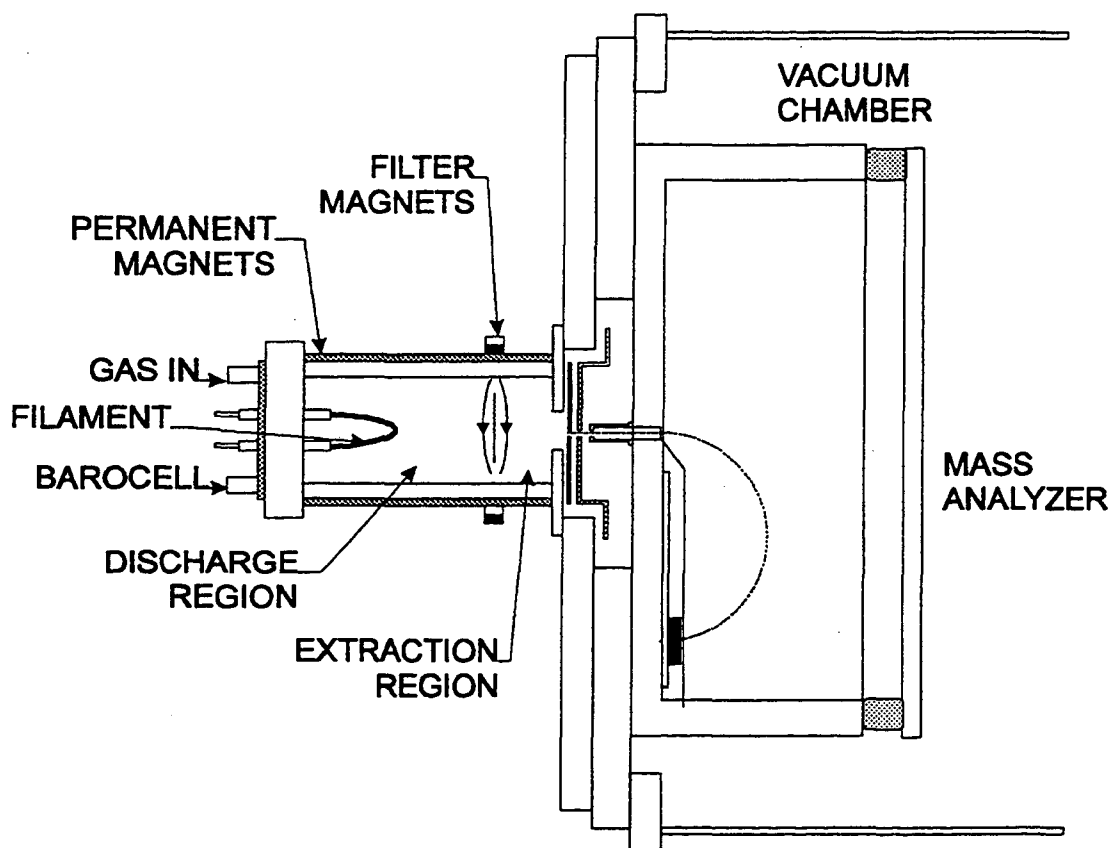
FIGURE 6.1 Schematic drawing of a filament operated multicusp ion source mounted in a vacuum chamber. A magnetic analyzer is shown.

6.2 HYDROGEN ION SPECIES MEASUREMENT

The ion species measurement was carried out with the filter at various hydrogen gas pressures that ranged from 0.6 to 2.4 mTorr and discharge currents from 0.5 to 2 A.

The discharge and extraction voltages, however, were maintained at 75 V and 1 kV respectively, throughout the ion species measurement.

Fig. 6.2 shows a sample trace of the hydrogen ion species spectrum. In this figure, the percentage of H^+, H_2^+ and H_3^+ are approximately 10 %, 87 % and 3 % respectively. Depending on the operating conditions, the distribution of these ion species can change.
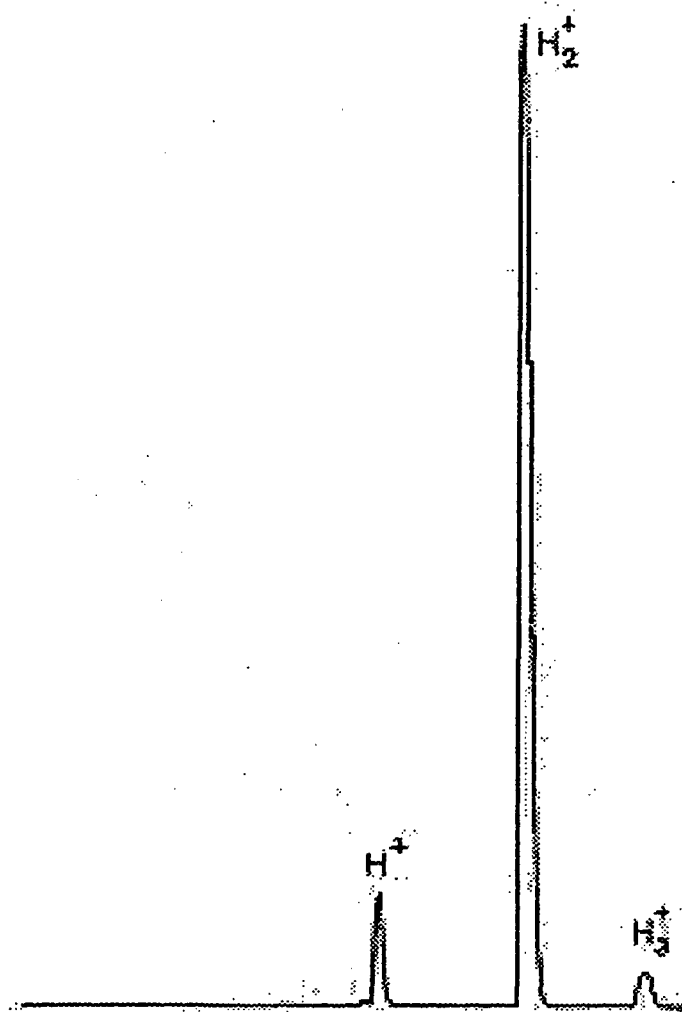
FIGURE 6.2 The output signal of the magnetic mass spectrometer. The percentage of H^+, H_2^+ and H_3^+ are approximately 10%, 87% and 3 % respectively.

In a hydrogen discharge, the H_2^+ ions are mainly produced in the discharge region by the following reaction:

$$H_2 + e \rightarrow H_2^+ + 2\,e \qquad \text{(Eq. 6.1)}$$

The other two species of hydrogen ions are formed from H_2^+, H_2 and H.

For H^+:
$$H_2 + e \rightarrow H^+ + H + 2e \qquad \text{(Eq. 6.2)}$$

$$H_2^+ + e \rightarrow H^+ + H + e \qquad \text{(Eq. 6.3)}$$

$$H + e \rightarrow H^+ + 2e \qquad \text{(Eq. 6.4)}$$

For H_3^+:
$$H_2^+ + H_2 \rightarrow H_3^+ + H \qquad \text{(Eq. 6.5)}$$
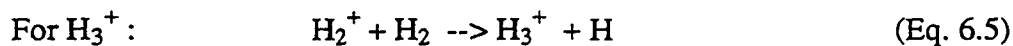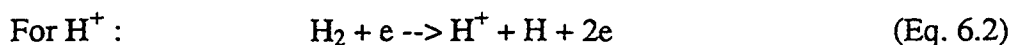
The percentage of each ion species versus gas pressure at a fixed discharge current of 2A is plotted in Fig. 6.3. The H^+ and H_2^+ fractions decrease with increase in pressure while the H_3^+ concentration increases. At higher pressures, more H_2 molecules are available to react with the H_2^+ ions forming H_3^+ ions. The cross-section for the reaction, $H_2^+ + H_2 \rightarrow H_3^+ + H$, at low interaction energies (< 2 eV) is in the 10^{-15} cm^2 range. At very low pressures, because of the limited number of hydrogen gas molecules for the reaction, the percentage of H_3^+ is smaller than H^+.
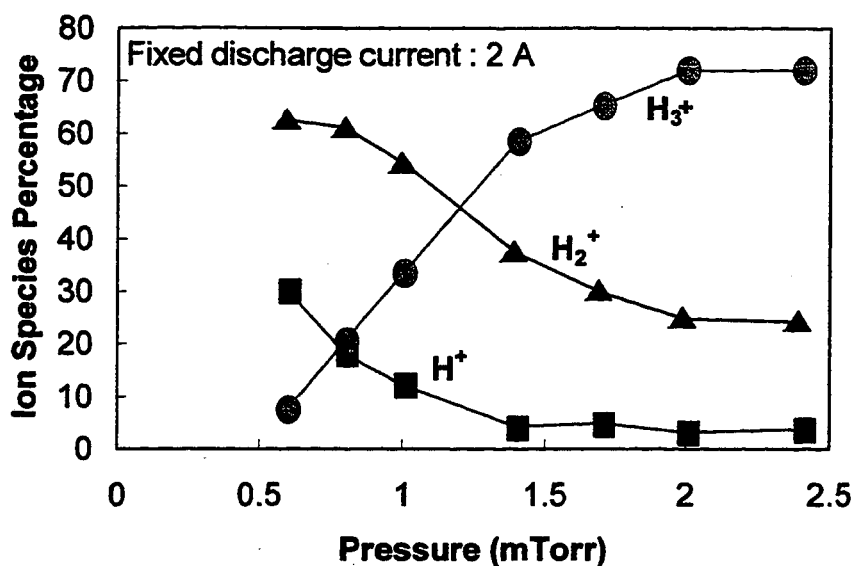
FIGURE 6.3 Percentage of hydrogen ion species versus gas pressure at a fixed discharge current of 2 A.

The percentage of ion species versus discharge current at a fixed pressure of 0.6 mTorr, is plotted in Fig. 6.4. Within this small range of discharge current, the ratio of the three hydrogen species H^+, H_2^+, H_3^+ remains nearly constant. Fig. 6.5 shows the percentage of each species versus discharge current at a higher pressure (1.1 mTorr). It can be seen that H_2^+ is still the dominant ion species but there are more H_3^+ ions than the H^+ ions due to the higher pressure.
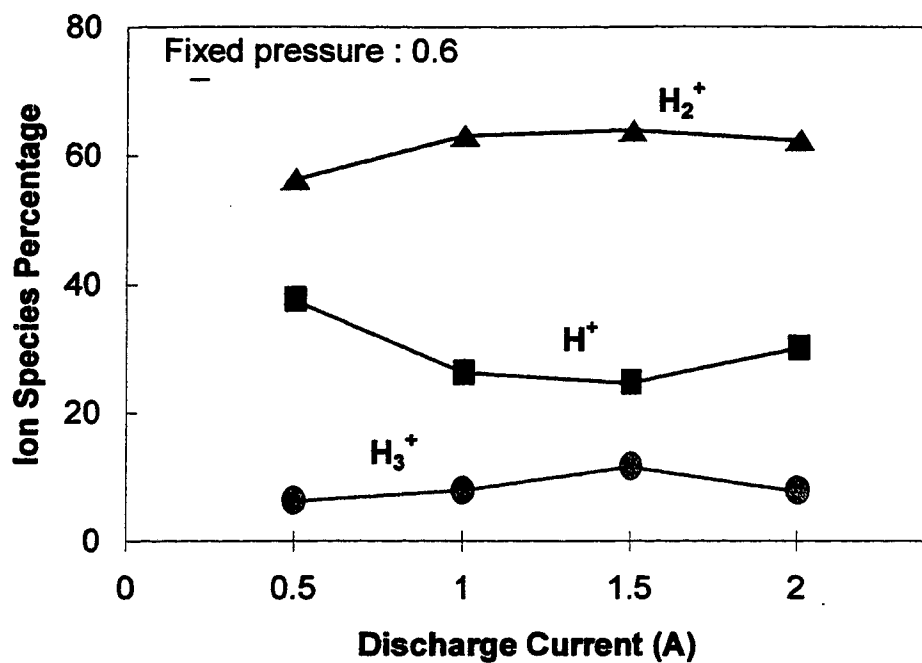
FIGURE 6.4 Percentage of hydrogen ion species versus discharge current at a fixed extraction voltage of 1kV and at a gas pressure of 0.6 mTorr.
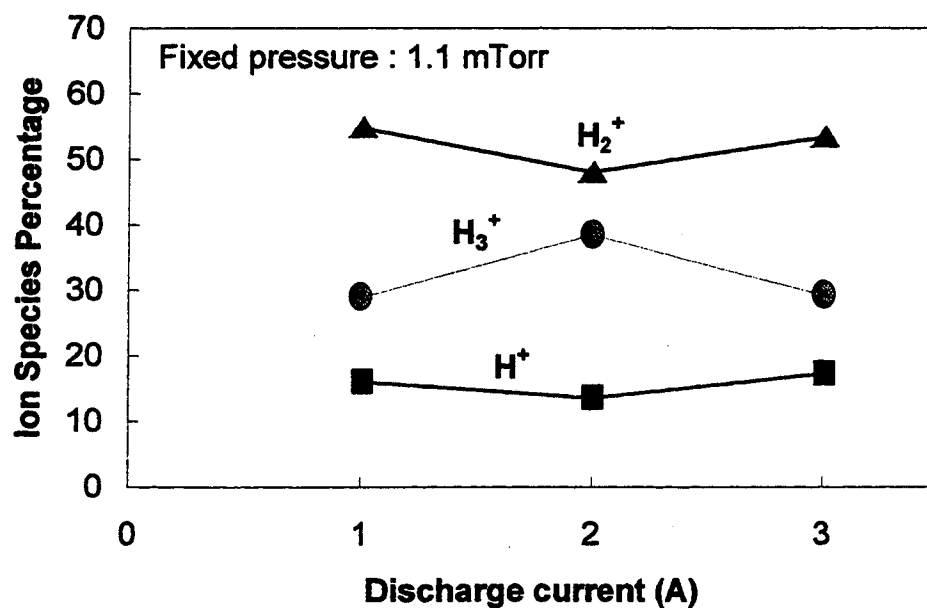
FIGURE 6.5 Percentage of hydrogen ion species versus discharge current at a fixed extraction voltage of 1kV and at a gas pressure of 1.1 mTorr.

6.3 AXIAL ENERGY SPREAD MEASUREMENTS

The ion species distribution was obtained by the use of the magnetic deflection mass spectrometer.[35] The magnetic field B for deflecting a singly charged ion of mass M and energy E to a gyroradius R is given by:

$$B(\text{Gauss}) = \frac{144[\mu E(\text{eV})]^{1/2}}{R(\text{cm})}$$

(Eq. 6.6)

where $\mu \equiv M/M_p$ and M_p is the proton mass.

Fig. 6.6 shows that each peak has a finite width due to the axial energy spread of individual species, where the accuracy is limited by the resolution of the instrumentation (e.g. the angular divergence, and the fall and rise time of the x-y recorder pen). The axial energy spread, ΔE, is defined as the full width at half maximum (FWHM) of the peak signals.

Fig. 6.6a shows that if the energy of the individual ion peaks is the same, then the distance along the x axis (the B-field) is proportional to $(ME)^{1/2}$. The position of the individual ion peak center is the average energy of the extracted ion beam species. The distances from the origin to the peak (x_1, x_2 and x_3) can be easily calculated. Once the distances x_1, x_2 and x_3 are known, the energy spread of the beam can be inferred from the width of the peak signal using the relationship of Eq. 6.6
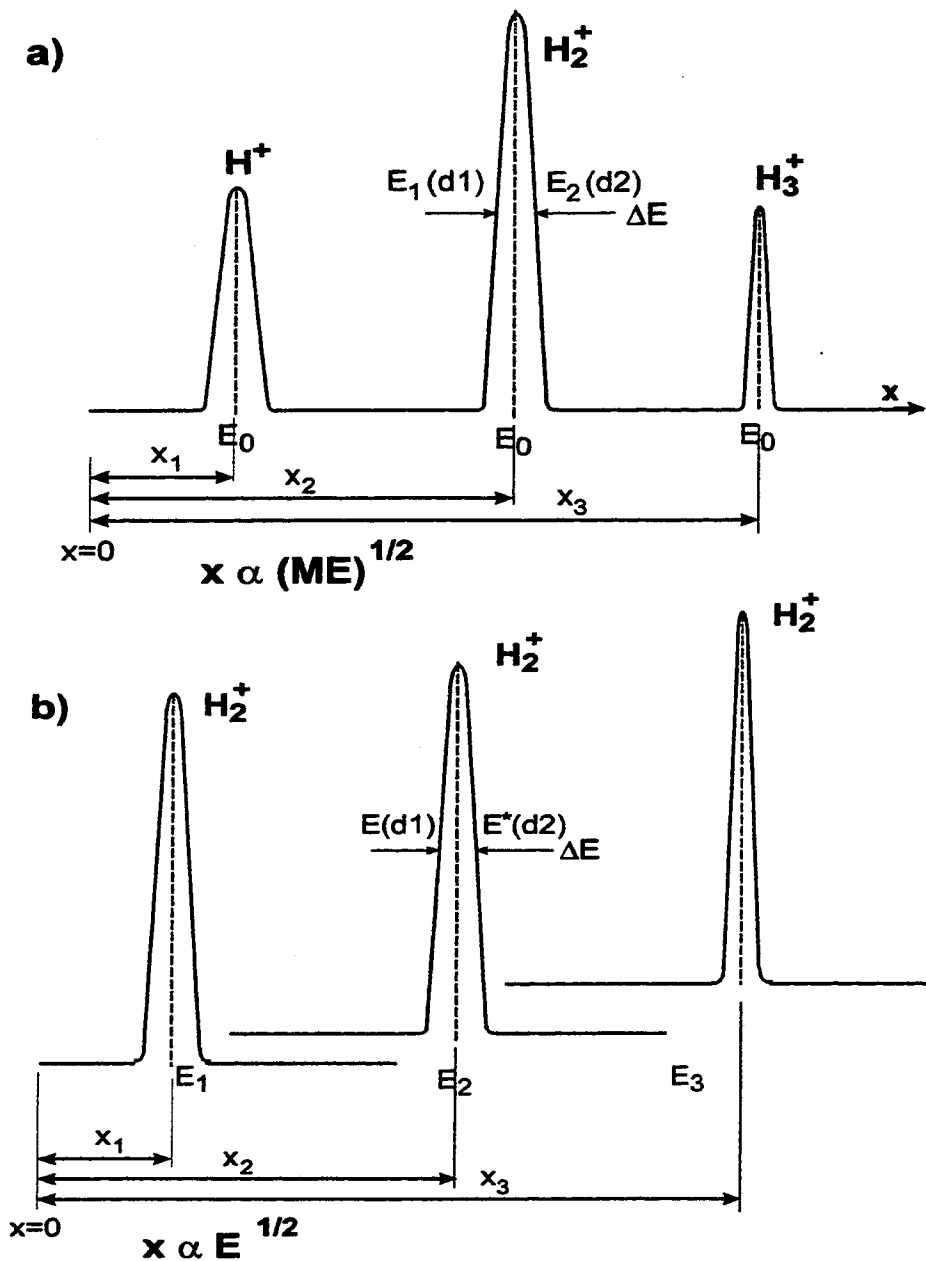
FIGURE 6.6 **(a)** The axial energy spread is found graphically from the ion species traces. The energy of the individual ion peaks is the same and the distances are proportional to $(ME)^{1/2}$. The position of the individual ion peak center is the average energy of the extracted ion beam species. (Fixed beam energy, vary magnetic field B). **(b)** Spectrometer output traces of same ion species at different energies as an alternative method.

In the figure (Fig. 6.6a), E_2 and E_1 are energies corresponding to the half height of the peak, and d_2 and d_1 are the corresponding distances from the origin. The energy spread, ΔE, is the difference between E_2 and E_1. This method is also used for a single ion species measurement; instead of using traces of the different species at a same energy, traces of one species at different energies can be used, as shown in Fig. 6.6b.

The axial energy spread in the filament driven multicusp source using the magnetic filter for the hydrogen ion species H^+, H_2^+, H_3^+ was found to be 2.3 eV, 2 eV, 1.7 eV, respectively. As expected, the axial energy spread with the filter removed was larger and was found to be 3.5 eV for H_2^+ and H_3^+. The H^+ signal was too small to be analyzed.

The same technique was used for the axial energy spread measurement for the negative hydrogen ions. The H^- ions are formed predominantly in a two-step dissociative attachment process: [36]

$$H_2 + e \text{ (high energy)} \rightarrow H_2^* + e \qquad \text{(Eq. 6.7)}$$

$$H_2^* + e \text{ (low energy)} \rightarrow H_2^- \rightarrow H^- + H \qquad \text{(Eq. 6.8)}$$
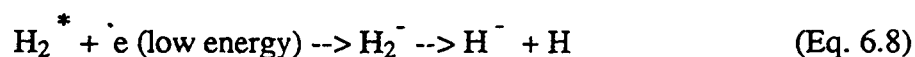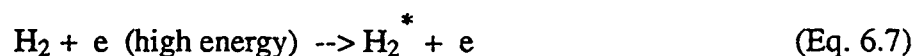
where H_2^* is a vibrationally excited molecule. The magnetic filter arrangement can enhance the formation and reduce the destruction of H^-. The filter separates the extraction region from the discharge region. In the extraction region, the electron temperature is much lower than in the discharge region. Thus, with the proper tailoring of the filter-field, it can be arranged such that the H^- is formed in the extraction region. Since the plasma potential gradient in this region is small, the H^- ion energy spread is expected to be lower

than that of the positive ions. The H$^-$ energy spread, measured by the magnetic deflection spectrometer, as shown in Fig. 6.7, was found to be approximately 1 eV, half of that of the positive hydrogen ions.
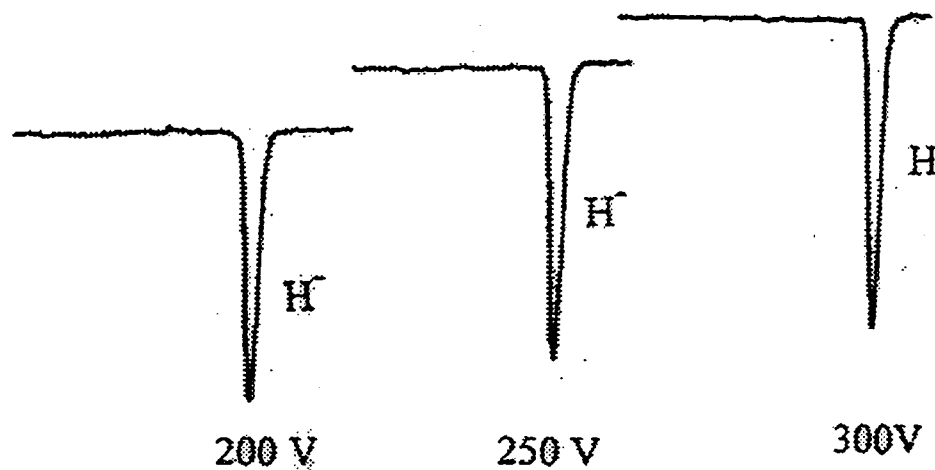
FIGURE 6.7 Spectrometer output signal showing the H$^-$ ion peaks at 3 different extraction voltages.

Negative ions present some advantages over positive ions that could well be used for ion projection lithography. As feature size requirement becomes smaller and smaller, negative ions can outperform positive ions. When positive ions impinge on the substrate surface, secondary emission electrons are produced resulting in a net positive charge on the surface. The positive ion beam is then deflected, broadening the size of the features. This charging problem is eliminated when negative ions are used. As the secondary emission electrons leave the substrate surface, they will counteract the accumulation. As a result the charging problem is minimized, Fig. 6.8
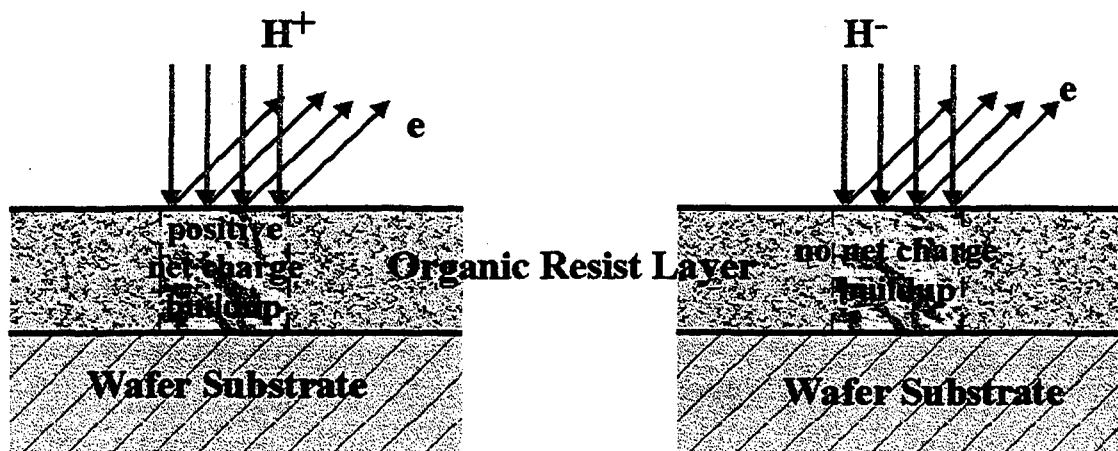
FIGURE 6.8 Charging problem between positive and negative hydrogen ion beams on resist layer.

6.4 COMPARISON OF ENERGY SPREAD MEASUREMENTS BETWEEN THE RETARDING FIELD ENERGY ANALYZER AND THE MAGNETIC ENERGY ANALYZER

The magnetic deflection spectrometer described in the previous section was used to measure the axial energy spread of the extracted ions. The retarding field analyzer measures the energy spread at the exit aperture of the small ion source without using beam extraction. This apparatus is used to study the energy spread of the combined ions in this small multicusp ion source. Figures 6.9a and 6.9b show the measured data and its differentiated curve for hydrogen, at a gas pressure of 1 mTorr. The energy spread in this measurement was found to be 0.8 eV. With this analyzer, the energy spread of each species cannot be determined, and the reported value is assumed to be the energy spread of the H_2^+ ions, as H_2^+ is the dominant ion species.

Similarly, helium was also used for energy spread measurements with the electrostatic energy analyzer. Under the same discharge conditions as for hydrogen, ΔE was found to be approximately 0.9 eV.
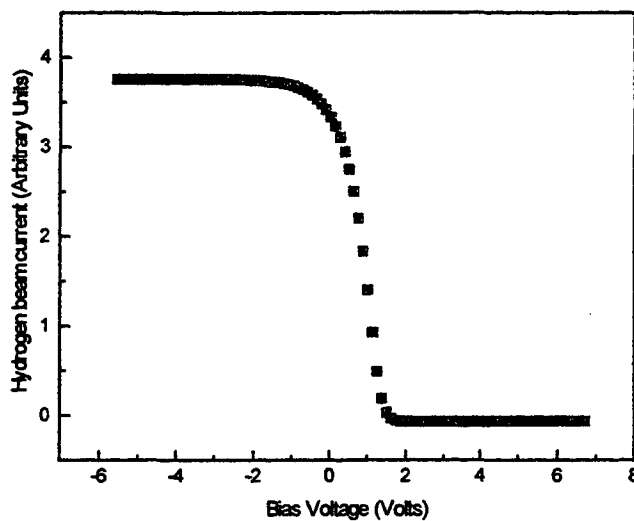
a)
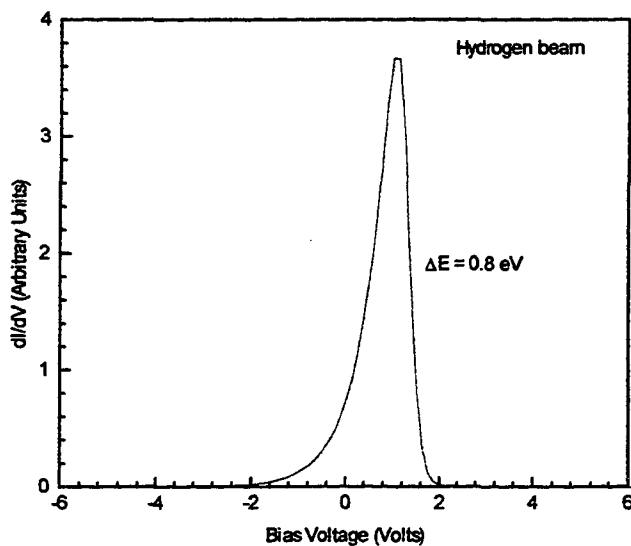
b)

FIGURE 6.9 (a) The I-V characteristics from an electrostatic energy analyzer for hydrogen. (b) The differentiated curve from (a).

CHAPTER 7

CO-AXIAL SOURCE FOR ULTRA-LOW ENERGY SPREAD BEAM

GENERATION

7.1   BACKGROUND OF SOURCE CONFIGURATION

The reduction in ion energy spread ΔE through axial plasma potential distribution adjustments has been confirmed in the experimental results presented in previous chapters. In order to further reduce ΔE, a new ion source configuration has to be designed. The radial plasma density profile for a 30 cm diameter multicusp generator has been measured by using a movable Langmuir probe.[37] Figure 7.1 shows that the density is uniform at the center and quickly falls near the walls. The plasma potential V_p has a similar radial distribution. This particular plasma density or potential distribution is due to the magnetic cusp field that confine the plasma efficiently.
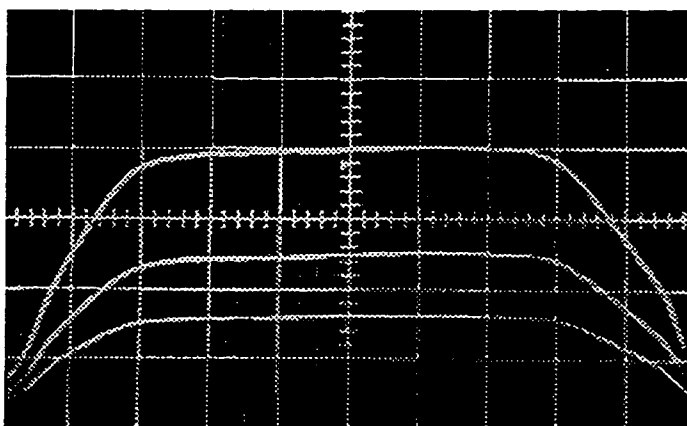
FIGURE 7.1 Radial plasma density profile. X-scale is 3 cm per division.

The ion energy spread in the central uniform region is very small, and it should approach the thermal energy of the ions (< 0.1 eV). This characteristic of the multicusp ion source can be utilized to form ion beams with energy spreads lower than 1 eV. In order to extract the ions that are generated in the uniform region, a co-axial source geometry has been proposed. This new source configuration should provide ions with very low axial energy spread.

Fig. 7.2 shows the schematic diagram of the co-axial source. The coaxial source uses the conventional multicusp chamber but with a new filter arrangement. The filter has a co-axial cage configuration with 6 permanent-magnet columns. Plasma is generated in the annular region between the source chamber walls and the filter cage and diffuses into the central region. The axial plasma potential of the outer annular region is uniform outside the cusp-field. Efficient plasma confinement and uniform plasma potential distribution are provided by permanent magnets on the side walls as well as those on the back and front flanges. The radial plasma potential profile suffers a dip at the center or extraction region. Ions present in this region are generated at the discharge side of the source with approximately the same energy, and have diffused from the discharge region to the central region. Since ions are not produced in the extraction region, the radial plasma potential distribution does not affect the axial energy spread.
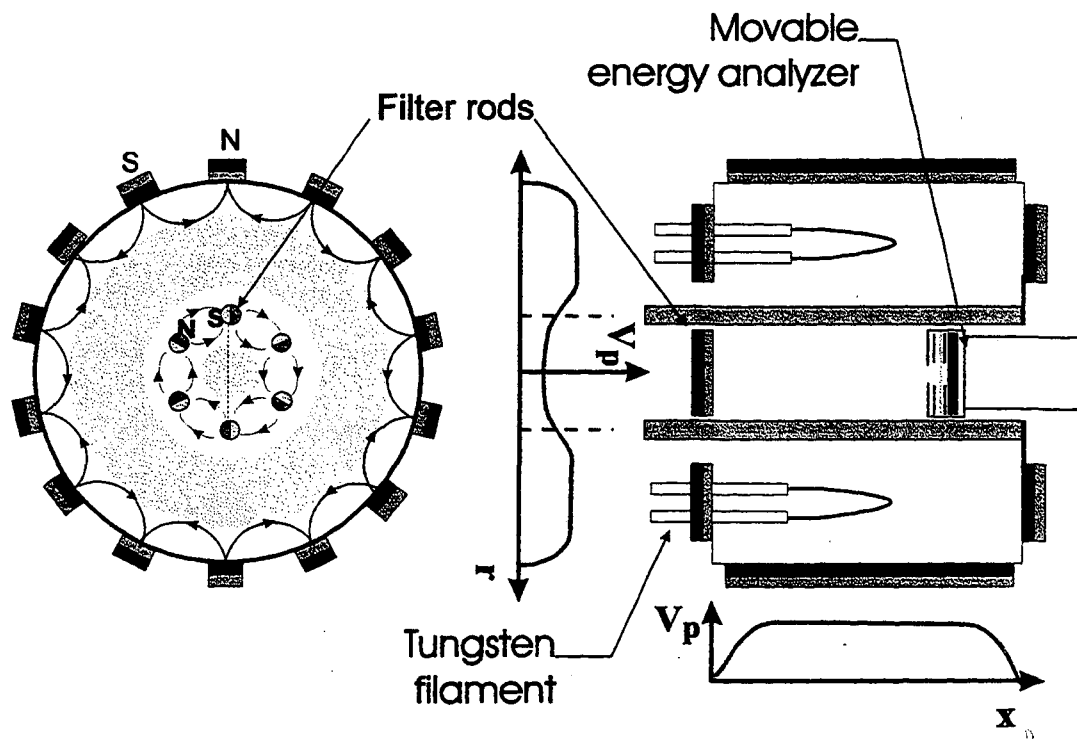
FIGURE 7.2 Radial and transverse view of the co-axial source.

7.2   CO-AXIAL SOURCE DESIGN

The source design has been aided by a computer program (called Beefy). The field free region (< 30 Gauss) in the center of the filter cage as well as the annular region is critical in the design since plasma is generated and extracted in these two regions respectively. Figure 7.3 shows a calculation using the computer code "Beefy". In the figure, a multicusp source (20 cm diameter) with 20 columns of permanent magnets surrounding the chamber was simulated. The magnets are placed around the chamber body with alternating polarities to generate the cusp field (8900 Gauss, samarium-cobalt magnets). The magnetic filter is designed with 6 permanent magnet columns (9000 Gauss, samarium-cobalt magnets). The positioning of these filter magnets are different

from those in the chamber wall, as shown in the figure. The magnitude of the field at regions of interest can be determined. In Fig. 7.3, the pink regions are the field free regions. Eventhough the Beefy program's graphical representation of the magnetic fields are not uniform, it is a useful tool in multicusp source design.
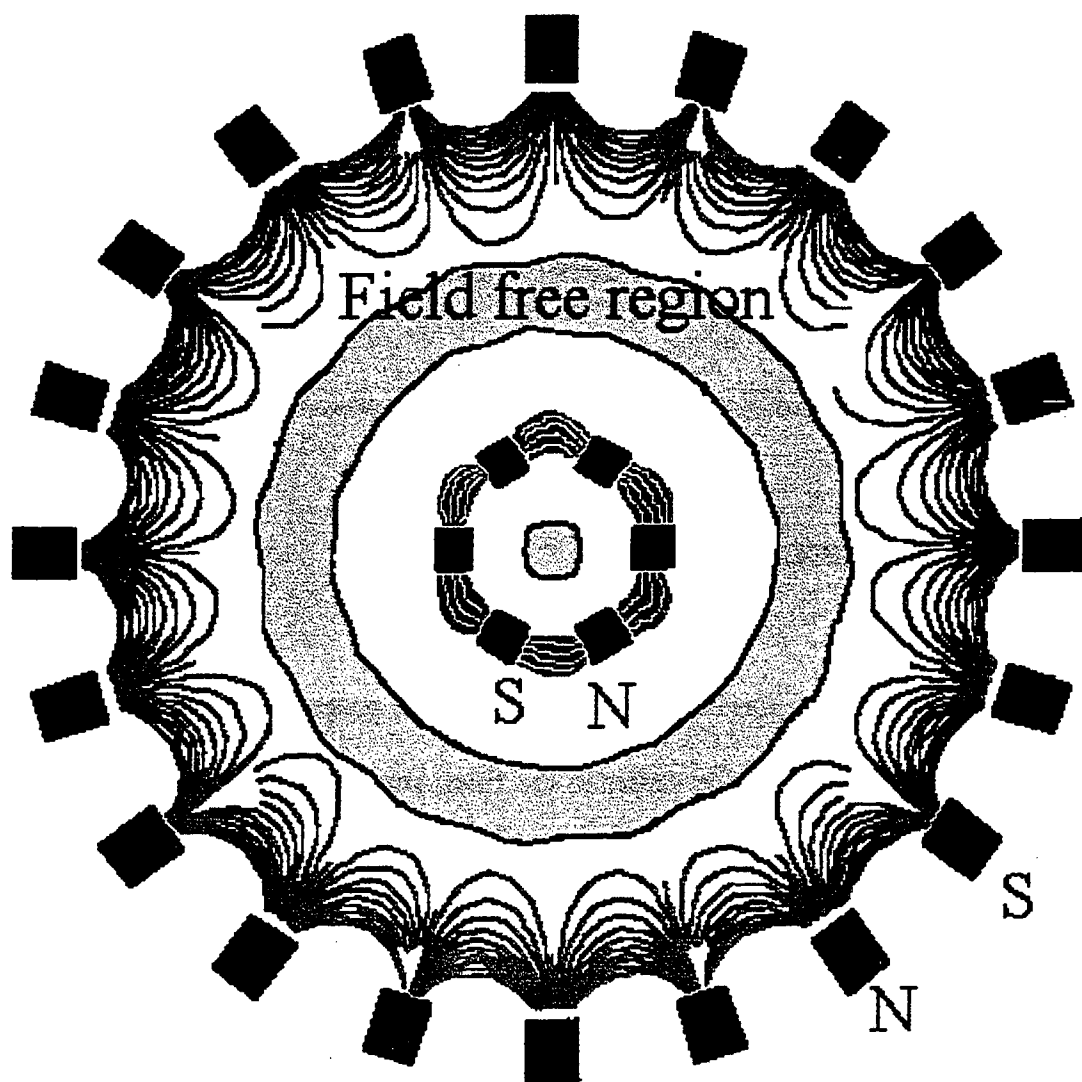
FIGURE 7.3 With 20 permanent magnet columns for the source chamber and 6 magnet columns for the filter cage.

The final coaxial source chamber design has 14 bars of magnets surrounding the chamber and a magnetic filter cage. The chamber is copper-plated stainless steel 20-cm-diameter by 20 cm long. The front plate has 14 magnets placed radially as shown in Fig. 7.4. The back flange has four rows of magnets. Four filament can be used for plasma generation. Additional ports are provided on the backflange for placing the filter cage, gas line, barocel, Langmuir probes, etc. The chamber and the flanges are water cooled.
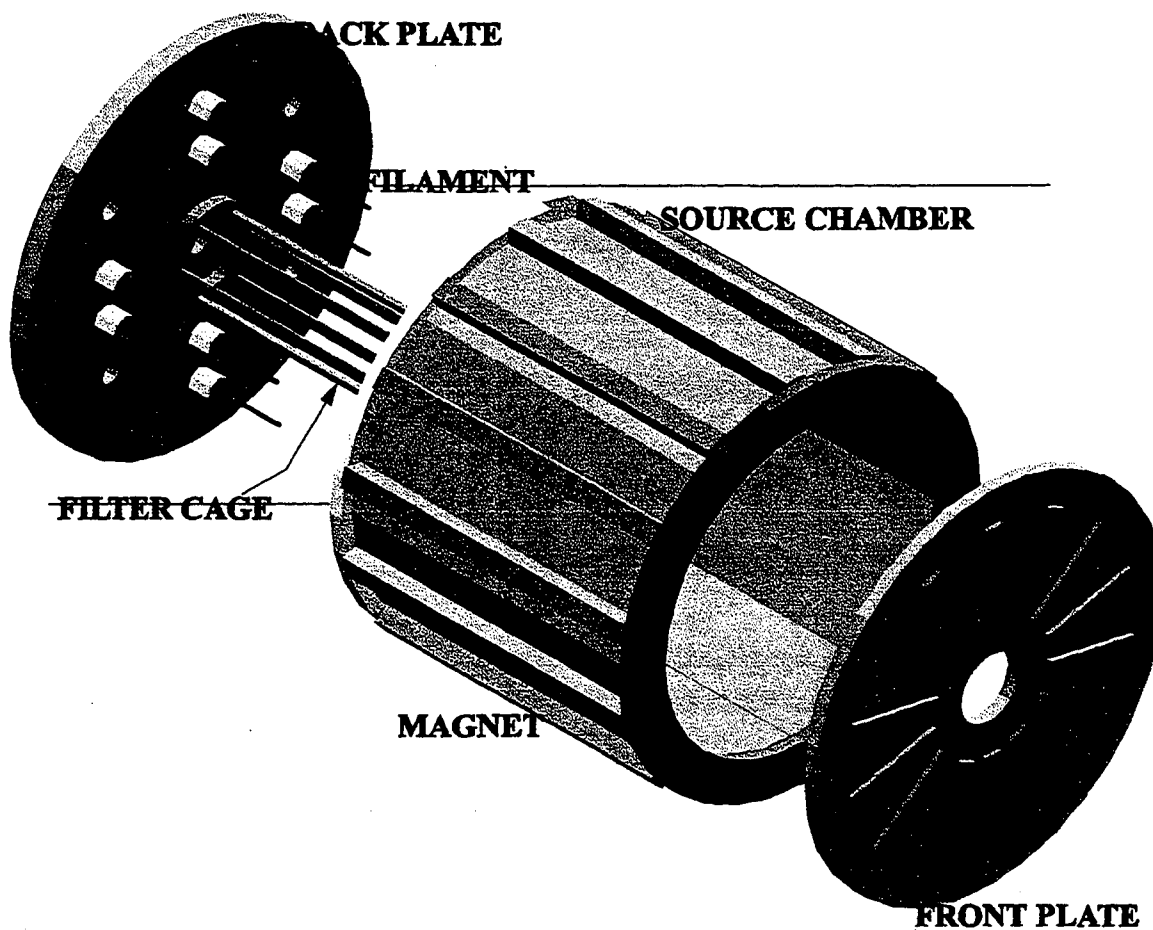
FIGURE 7.4 Three dimensional drawing of the co-axial source.

The filter cage is made out of copper. Small samarium cobalt magnets are placed inside the broached copper tubing. Water is supplied through one of the openings and distributed to cool the magnets.

Characterization of the co-axial source including axial plasma potential distribution, axial energy spread and extractable current testing results are presented in the following sections.

7.3   PLASMA POTENTIAL MEASUREMENT

The plasma potential of the co-axial source was measured by using Langmuir probes placed in the center region as well as in the annular region of the source. The probe trace was recorded by using an X - Y recorder. The probe can be moved along the axis to measure the axial plasma density and potential profile. The setup for this measurement is shown in Fig. 7.5.
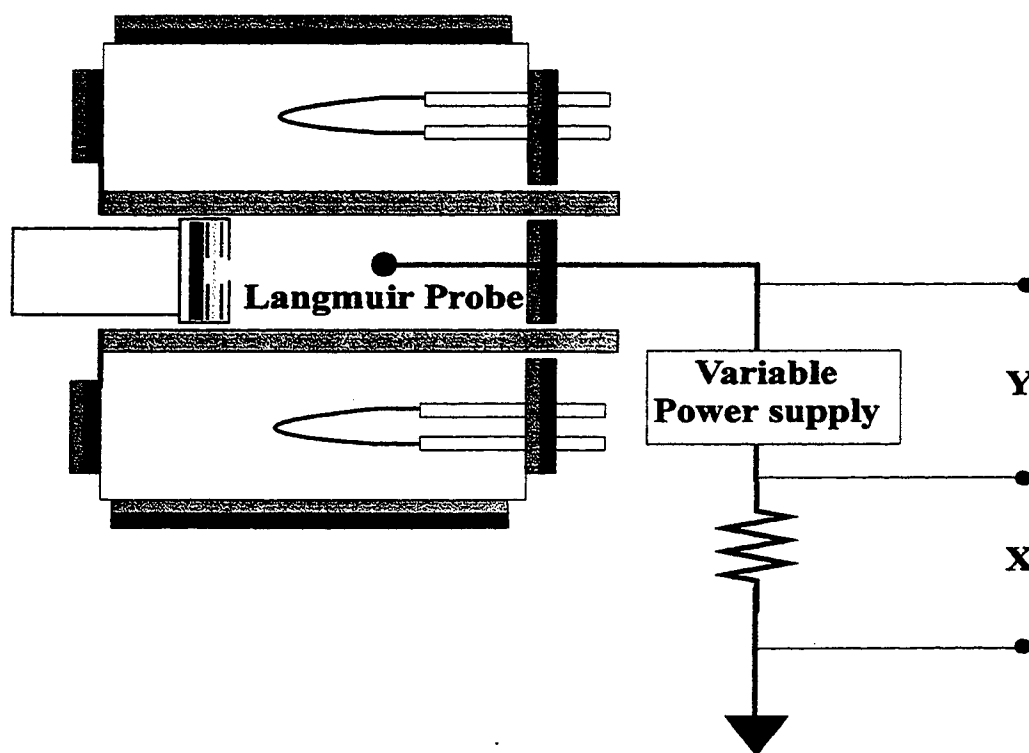
Figure 7.5   Langmuir probe measurement setup
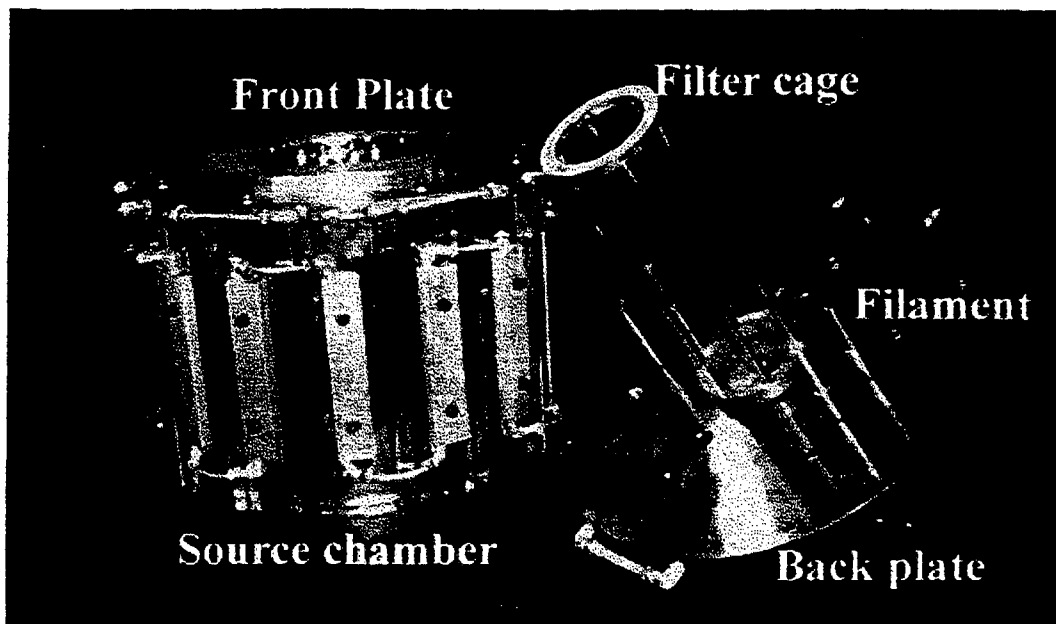
Figure 7.6   Picture of the co-axial source

In the co-axial source, it is expected that the electron temperature (T_e) in the extraction region to be lower than that in the discharge region. The maximum magnetic field between the magnet columns of the cage is ~ 40 Gauss for the weak filter and 250 Gauss for the strong filter.

With the weak filter and low discharge voltage (e.g. 50 V), electron temperature in the extraction region is lower than that of the discharge region. However, electron temperature in the extraction and in the discharge regions are approximately the same at high discharge voltages (e.g. 80 V). In the same manner, the plasma density in both regions are also approximately the same. This is because the magnetic field of the filter is not strong enough to confine the primary ionizing electrons. Langmuir probe traces of the extraction region and discharge regions at a discharge voltage of 80 eV are shown in Fig. 7.7. The difference between the two probe traces are almost negligible.
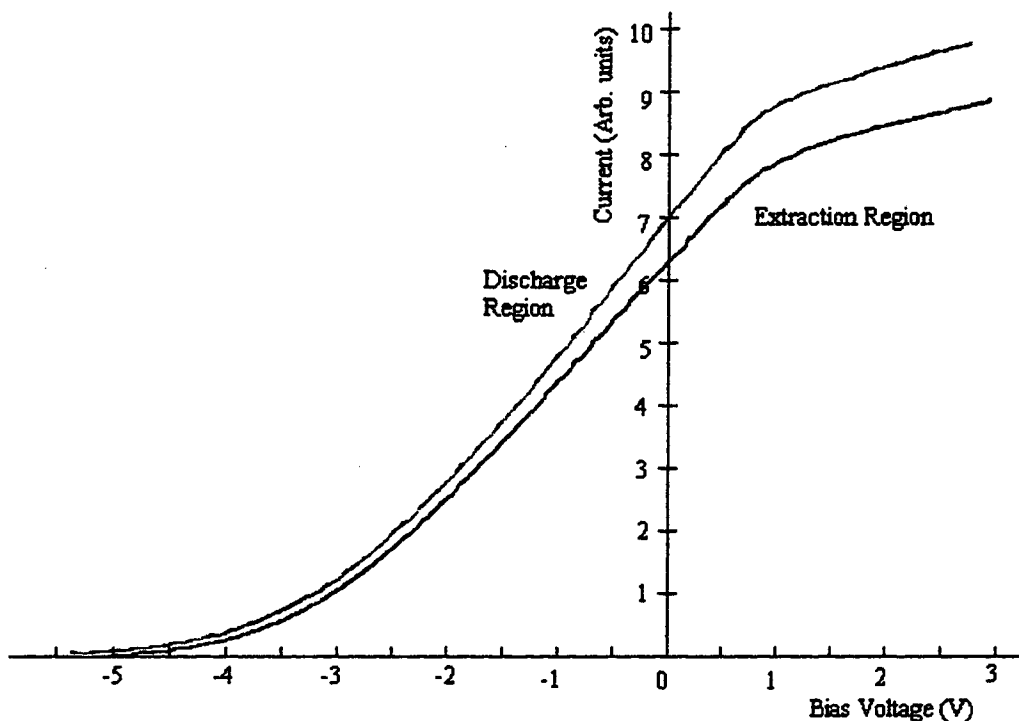
Figure 7.7   Langmuir probe trace at the extraction and discharge
regions. y-scale is the same for both traces.

Using a stronger filter (~250 Gauss), the electron temperature in the extraction

region has been found to be lower. Electron temperature as low as 0.1 eV has been

recorded at the extraction region, which is about an order of magnitude lower than that of

the discharge region (Fig. 7.8). A plasma source that can provide such low electron

temperature cannot be found easily. A low electron temperature ion source is desirable in

applications such as electron beam lithography.
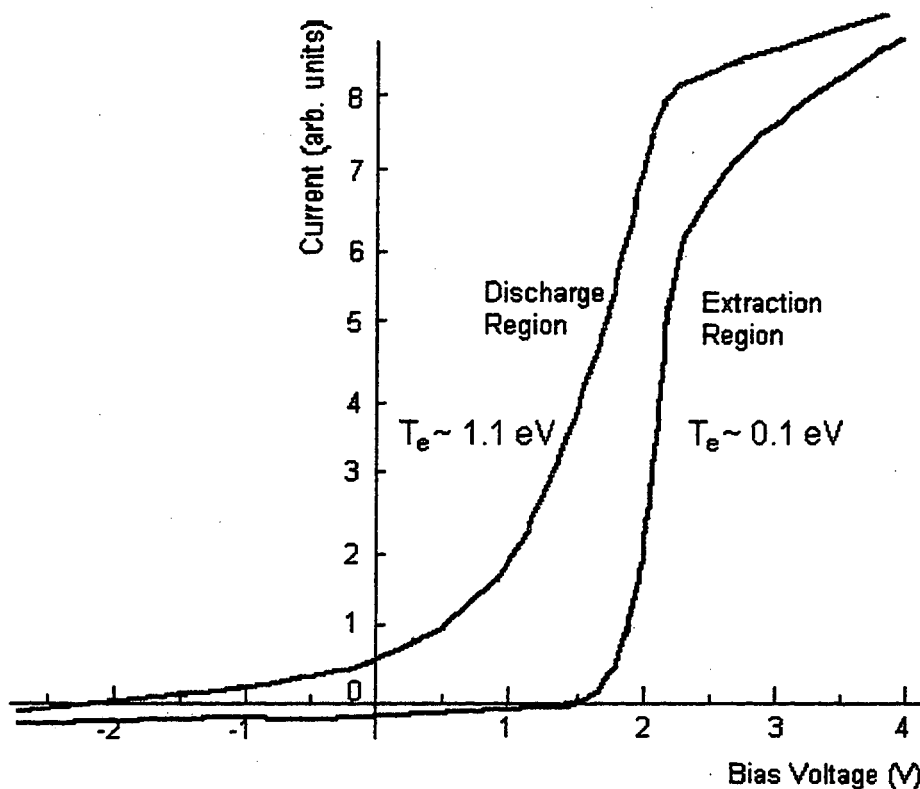
Figure 7.8   Langmuir probe trace at the extraction and discharge
regions. y-scale for the trace of the discharge region is 10
times greater than that of the extraction region.

Axial plasma potential distribution has been measured in both the central and the

outer annular regions. The plasma potential at the center is lower than that of the

discharge region (by ~ 0.5 V) as it has been expected (Fig. 7.9). However, uniformity of

the radial plasma potential distribution is not critical in reducing the axial energy spread.

Nevertheless, the axial plasma potential distributions are quite uniform in both regions.
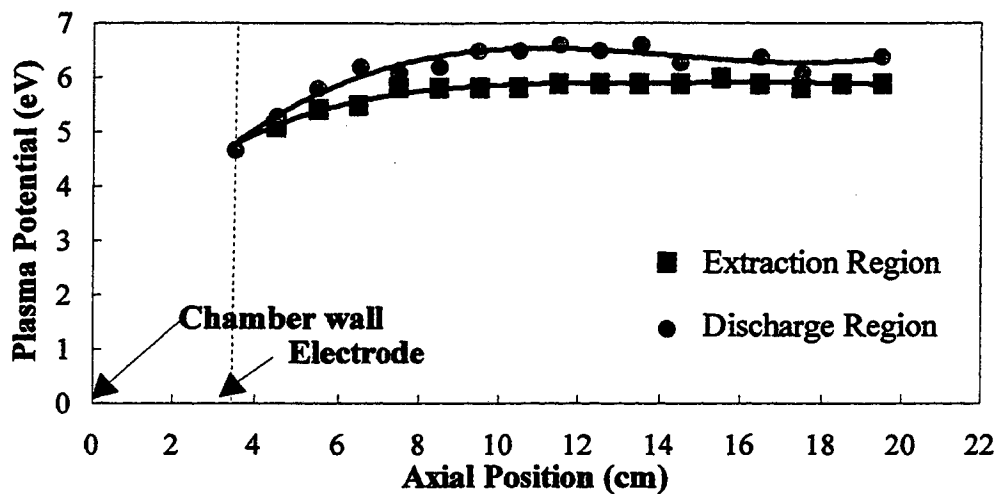
Figure 7.9   Axial plasma potential distribution in the coaxial source at
the extraction and discharge regions.

The electron temperature T_e inside the source can be inferred from the Langmuir probe trace. In Fig. 7.10, electron temperature versus axial position is plotted for the central and annular regions of the co-axial source when the strong filter cage is used. Electron temperature is lower in the center (labeled extraction region) than the annular region (discharge region) everywhere in the source. The electron temperature in Fig. 7.10 becomes lower at the axial position greater than 12 cm. This is because the probe is penetrating the cusp field of the back flange. This result demonstrates the effect of the filter, similar to the case of the planar filter described in Chapter 3.

The plasma density is obviously higher in the discharge region (Fig. 7.11). The plasma density and electron temperature were measured at a hydrogen gas pressure of 3 mTorr, at a discharge voltage of 80 V and at a discharge current of 4 A. The plasma density increases with the increase in discharge power, as shown in Fig. 7.12.
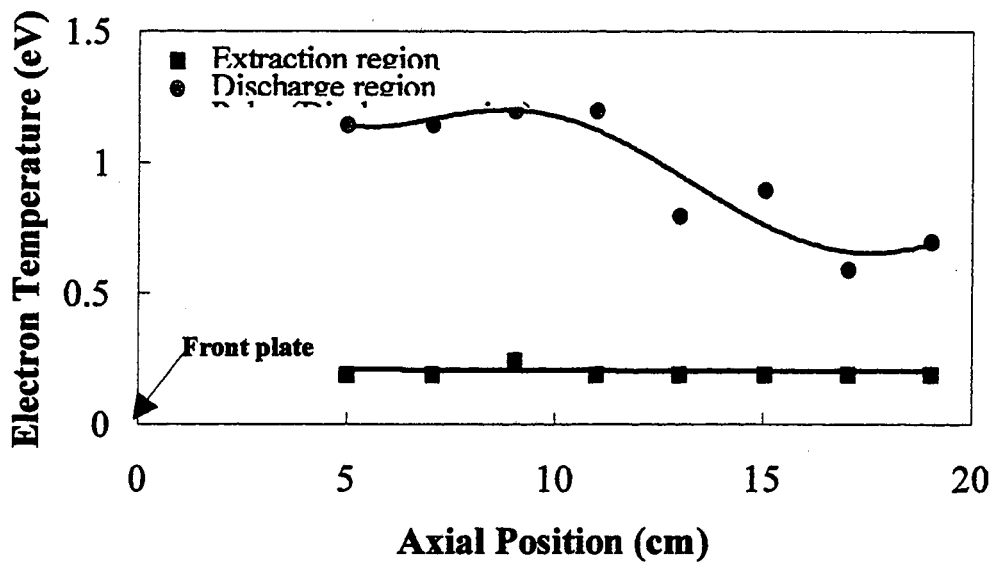
Figure 7.10   Axial electron temperature distribution in the coaxial source at the extraction and discharge regions.
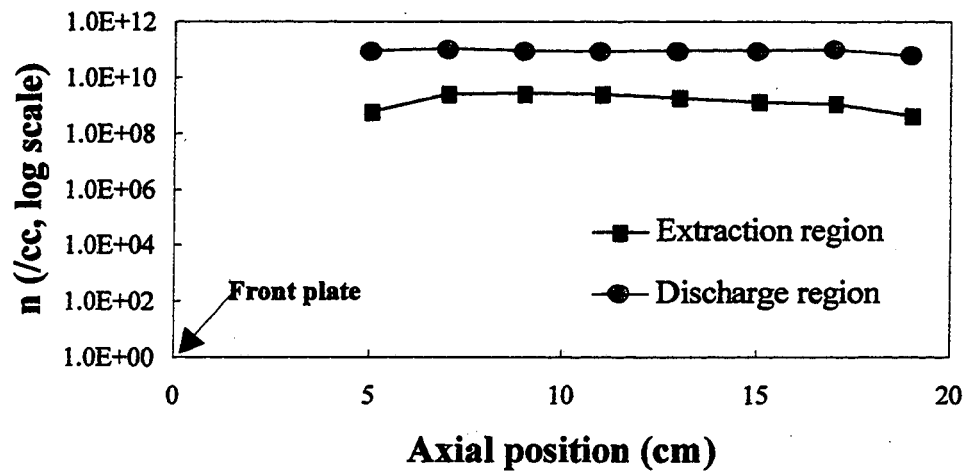
Figure 7.11   Axial plasma density distribution in the coaxial source at the extraction and discharge regions.
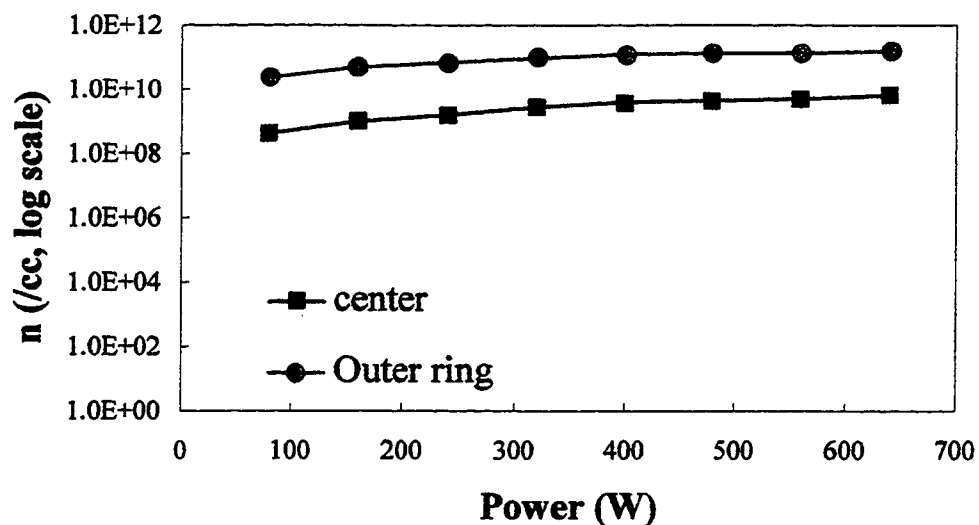
Figure 7.12 Plasma density increases with increasing discharge power in the extraction as well as in the discharge regions.

7.4 AXIAL ENERGY SPREAD MEASUREMENTS FOR THE CO-AXIAL SOURCE

The axial ion energy spread of the co-axial source has been measured using the retarding field energy analyzer. The energy analyzer was designed to be movable along the axial direction in order to investigate the influence of the plasma potential and density distributions on the axial energy spread. The inside of the co-axial chamber with the energy analyzer is shown in Fig. 7.13.
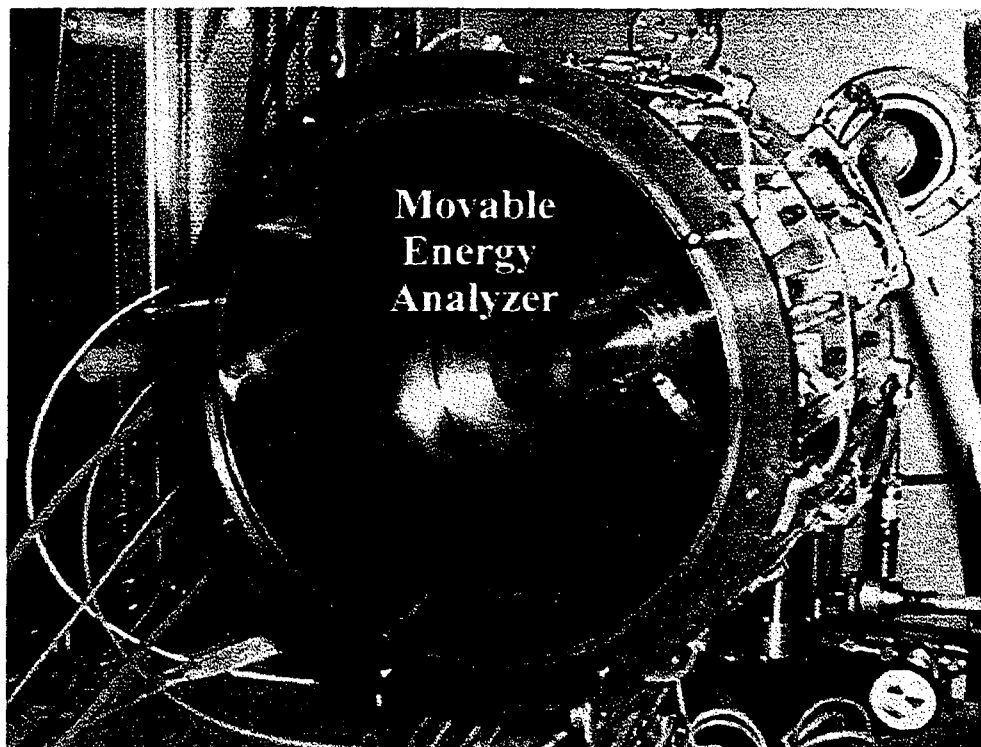
Figure 7.13 Inside of the co-axial chamber with the energy analyzer. The energy analyzer is moveable in the axial direction.

Using a weak magnetic filter cage ($B_{max} \sim 50$ Gauss), the co-axial source is found to have an average axial energy spread of less than 3 eV at a discharge power of 240 W, slightly increasing with increase in power. With a strong filter cage ($B_{max} \sim 250$ Gauss), hydrogen ion energy spreads of as low as 0.6 eV have been achieved (Fig. 7.14). The ion energy spread, ΔE as illustrated in Fig. 7.15, is approximately the same at different axial positions in the source. In Fig. 7.16, ΔE was measured at a discharge voltage of 80 V and discharge currents ranging from 1 A to 4 A at a fixed pressure of 3 mTorr. The energy spread is found to be < 1 eV at different discharge conditions. Even at different gas pressures, ΔE remains below 1 eV, as shown in Fig. 7.17.
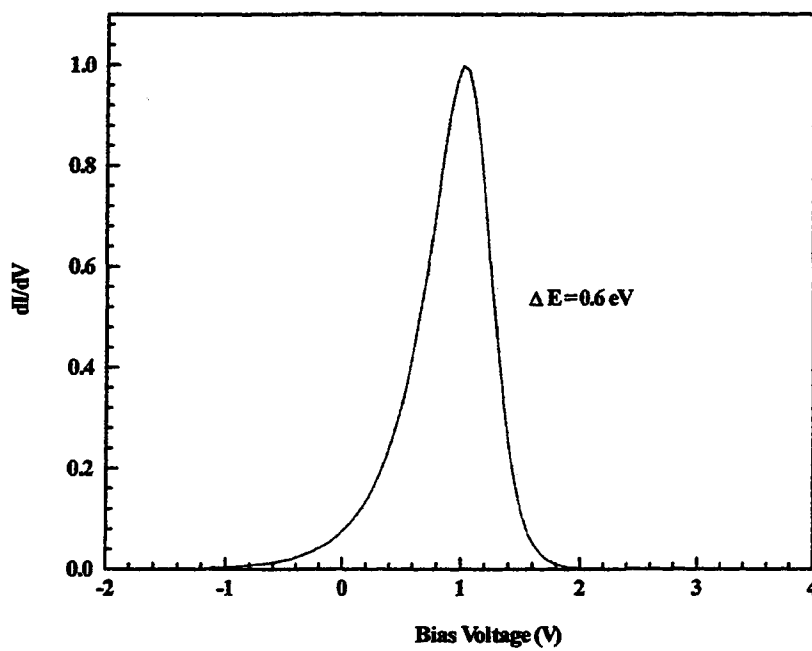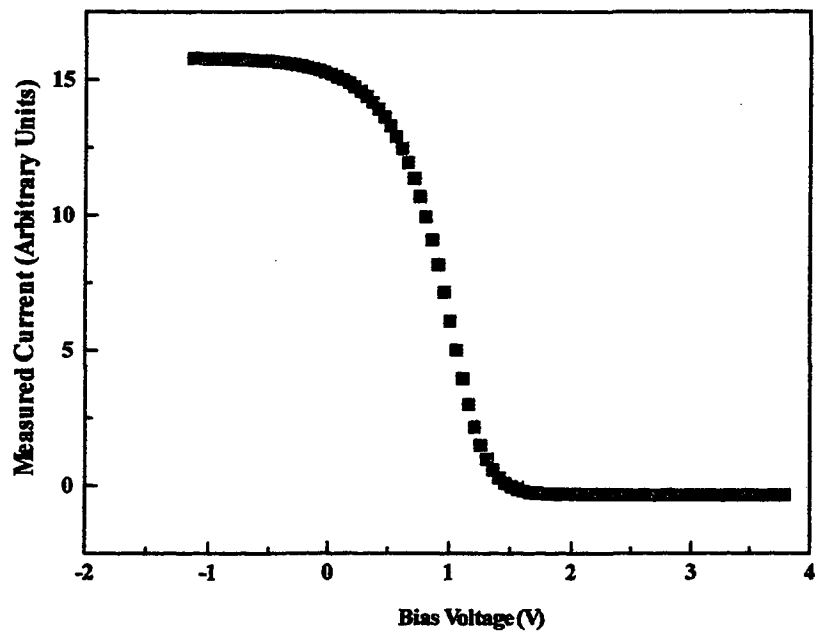
Figure 7.14   Energy spread of the co-axial source was measured to be as low as 0.6 eV.
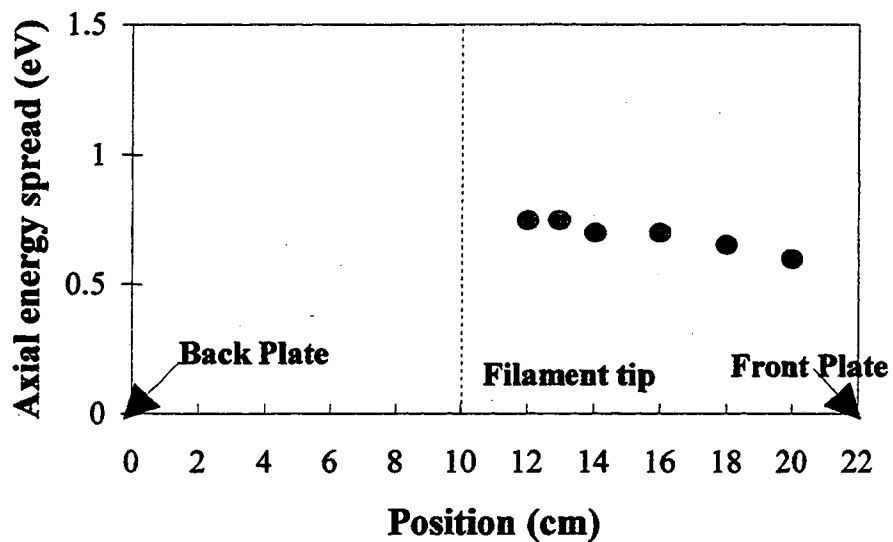
Figure 7.15   Energy spread of the co-axial source was measured at different axial positions. The results shows that energy spread is not sensitive to the axial position of the energy analyzer.
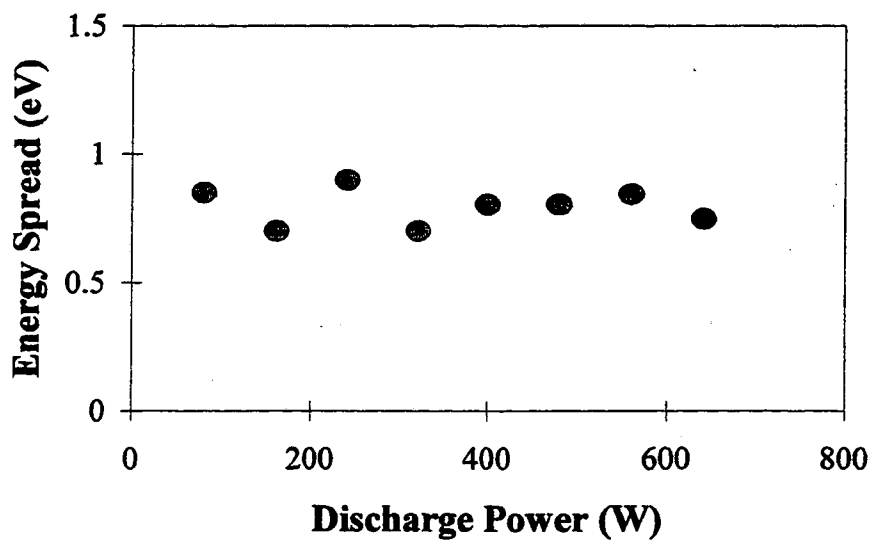
Figure 7.16   Energy spread vs. Power was measured with the energy analyzer 5 cm into the extraction region.
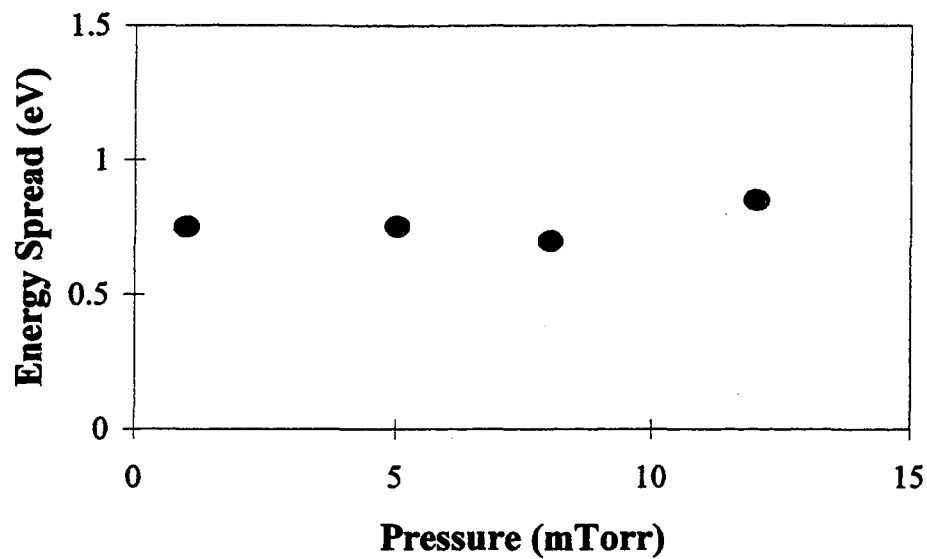
Figure 7.17   Energy spread vs. Pressure of the co-axial source at 320 W
of discharge power.

All these results demonstrate that the ion energy spread can be reduced below 1

eV by employing the co-axial source configuration. However, the filter strength must be

properly optimized to achieve a low energy spread as well as reasonable extractable

currents. Nevertheless, this new filter arrangement should not generate any fields at the

extraction aperture to affect the ion optics.

CHAPTER 8

ION OPTICS AND MEASUREMENTS FOR THE

CO-AXIAL SOURCE

8.1   EXTRACTION SYSTEM DESIGN

An extraction system has been designed for the co-axial source for beam extraction study, such as beam emittance. A simple triode extraction system was designed using a particle accelerator code, IGUNE. The first electrode is 3 mm thick with a 3-mm-diameter hole. The edge is sharpened with a Pierce angle of 67°. The second and third electrodes are 2 mm thick. with 14-mm-diameter and 29-mm-diameter hole sizes, respectively. The gap between the first and the second electrode is 20 mm, and between the second and the third is 30 mm. The first electrode is at 5 keV with the second or suppresser electrode at -300 V for electron suppression. This design yields an underdense condition with a cross over much like that of the IPL extractor design. The beam with the full energy is expanding as shown in the computer simulation in Fig. 8.1. This assembly has been tested for emittance measurements. In the figure, the beamlets at the end of the simulation is plotted in angle versus radius (r, r'). The rms emittance value given by the program is in x x' phase space. Eleven beam profiles at different axial positions are shown.
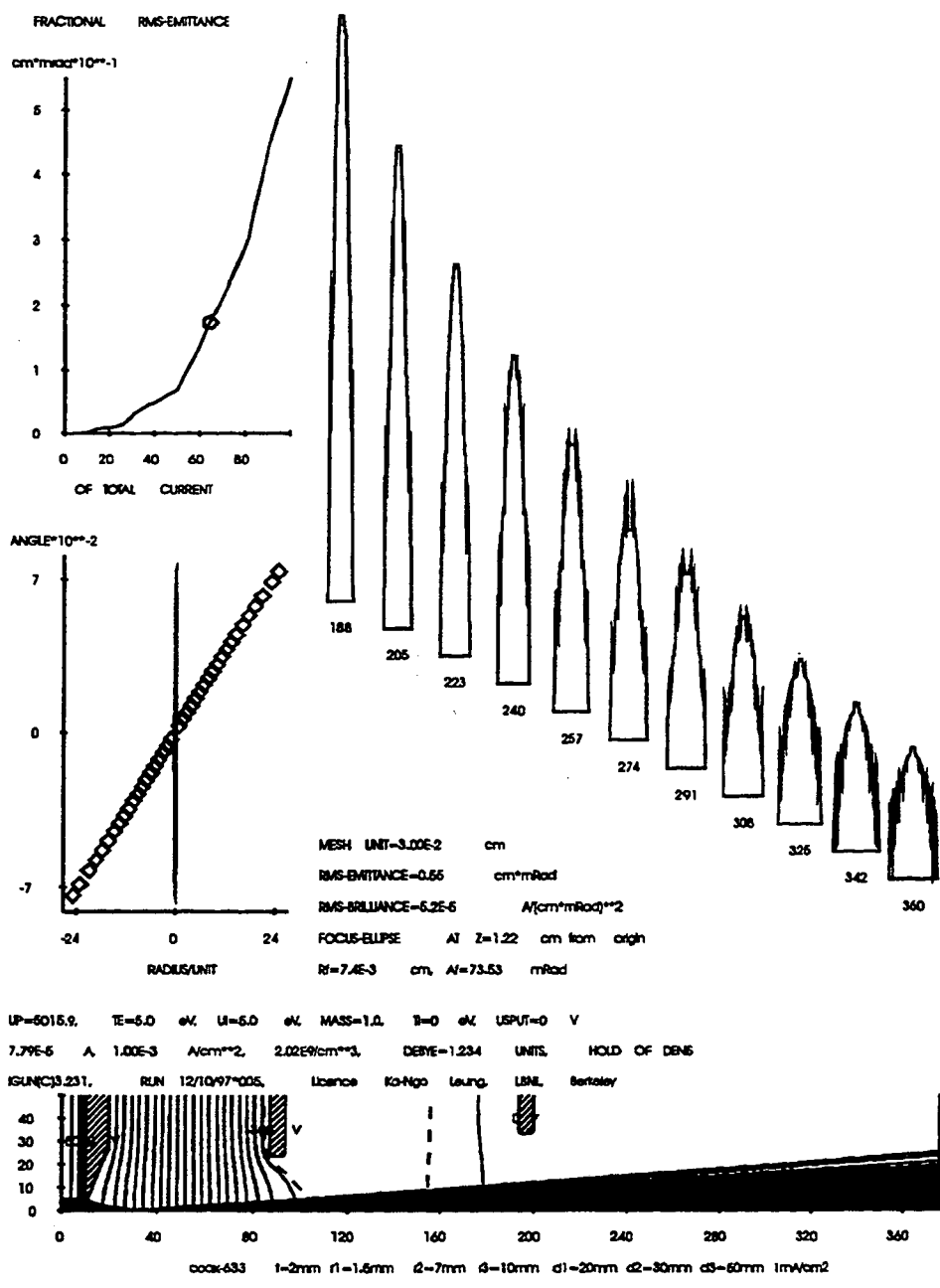
Figure 8.1 IGUNE design for the coaxial source. First electrode is at 5kV and the suppresser is at -300V. The beam has a cross over.

The first electrode can be positioned at 5 cm into the extraction region of the co-axial source where the axial density profile becomes uniform. Figure 8.2 shows a drawing of the complete accelerator assembly. The assembly consists of three electrodes and two

flanges. Between the electrodes, quartz tubes are placed in order to minimize voltage breakdown. The aluminum flange is directly mounted onto the front flange. This flange is water-cooled. The first electrode is mounted on this flange such that it is electrically connected to the source body. The second and third electrodes are mounted on the second flange (transparent plastic), and they are separated by insulators. Additional electrodes or a Faraday cup can be added if necessary. Figures 8.3 to 8.5 are pictures of the parts of the accelerator unassembled and also assembled.
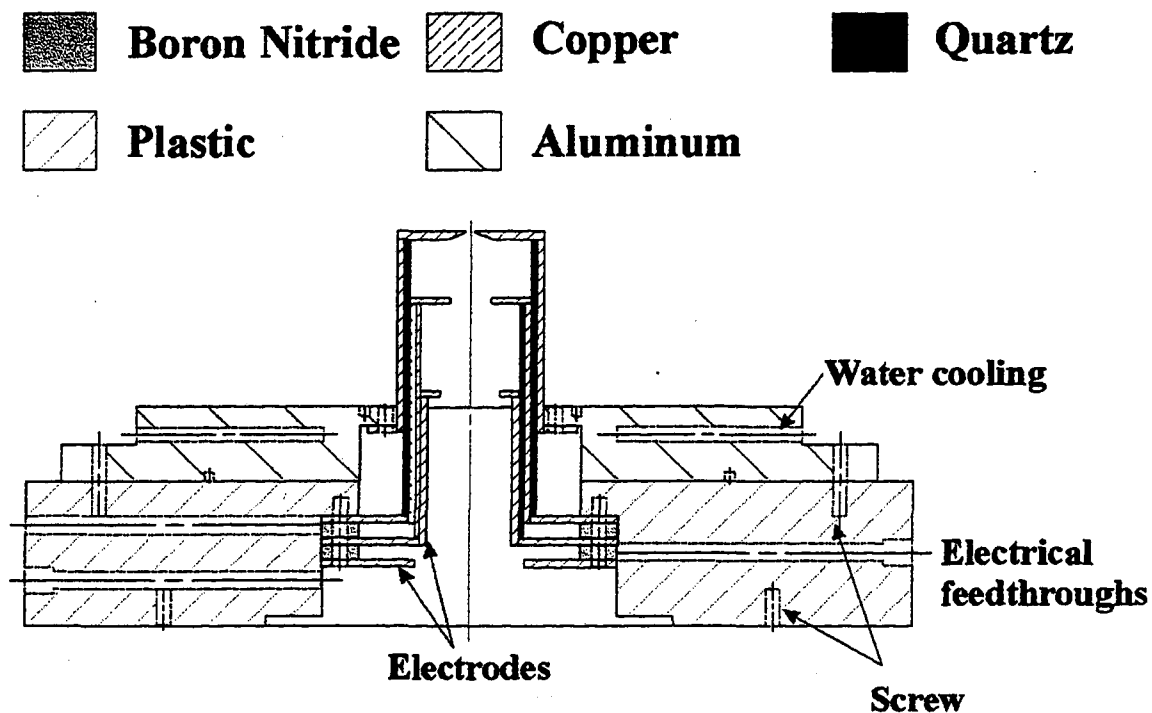
Figure 8.2   The aluminum flange is directly mounted to the front flange of the co-axial source. The first electrode is 5 cm into the source.
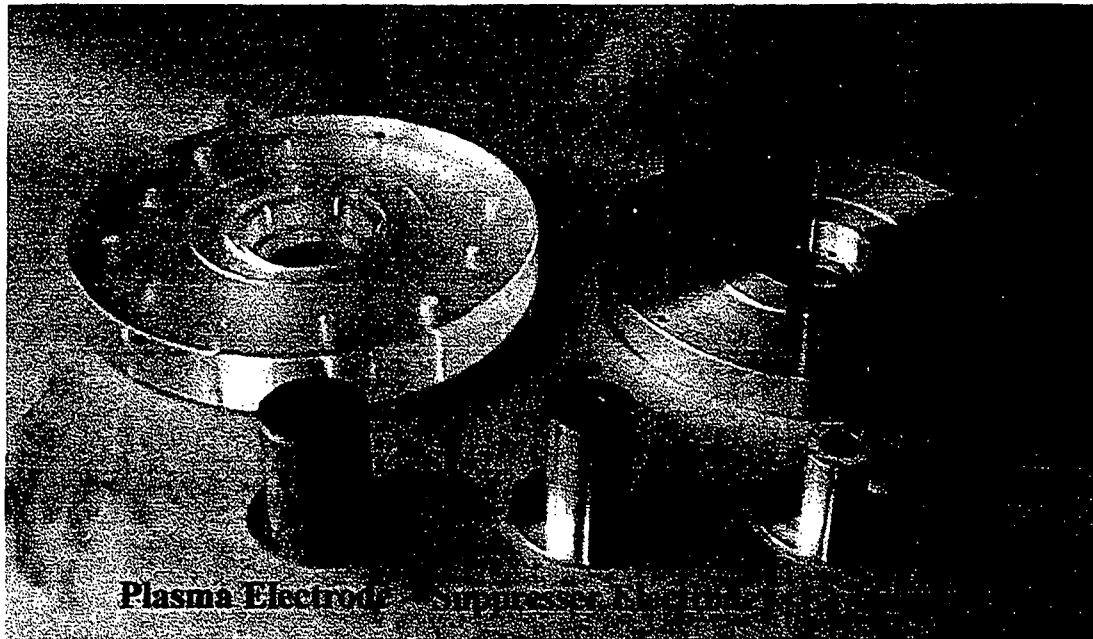
Figure 8.3   Unassembled parts of the accelerator. The aluminum flange
is directly mounted to the front flange of the co-axial
source. The first electrode is placed 5 cm into the source.
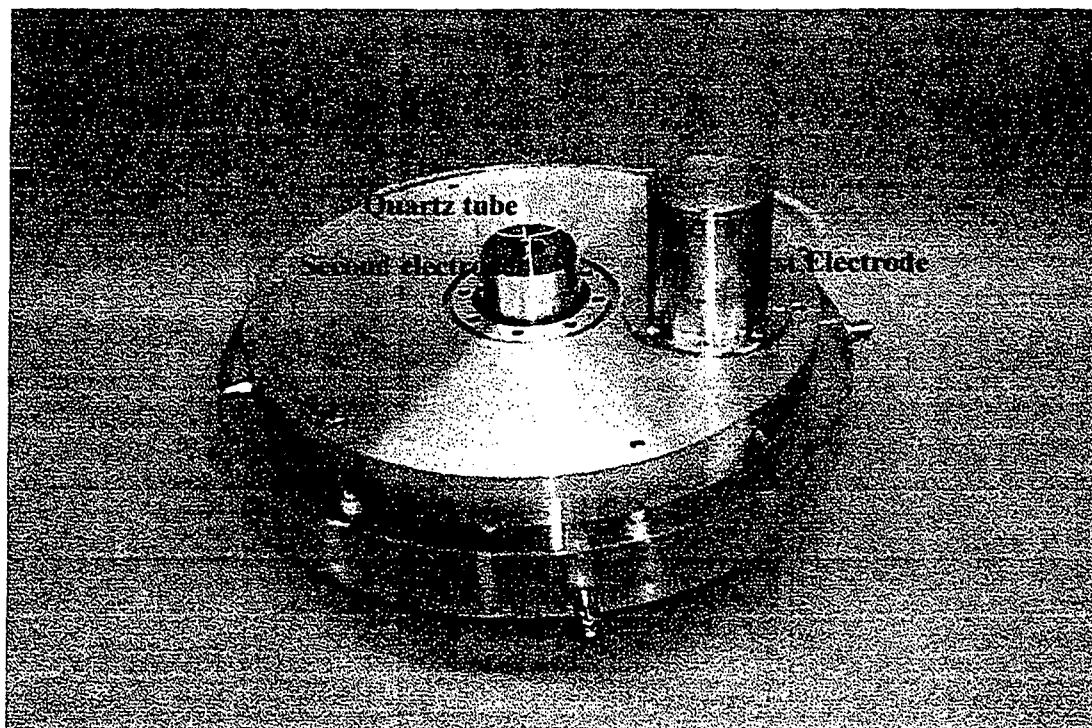
Figure 8.4   The quartz tube separates the first and the second
electrodes.
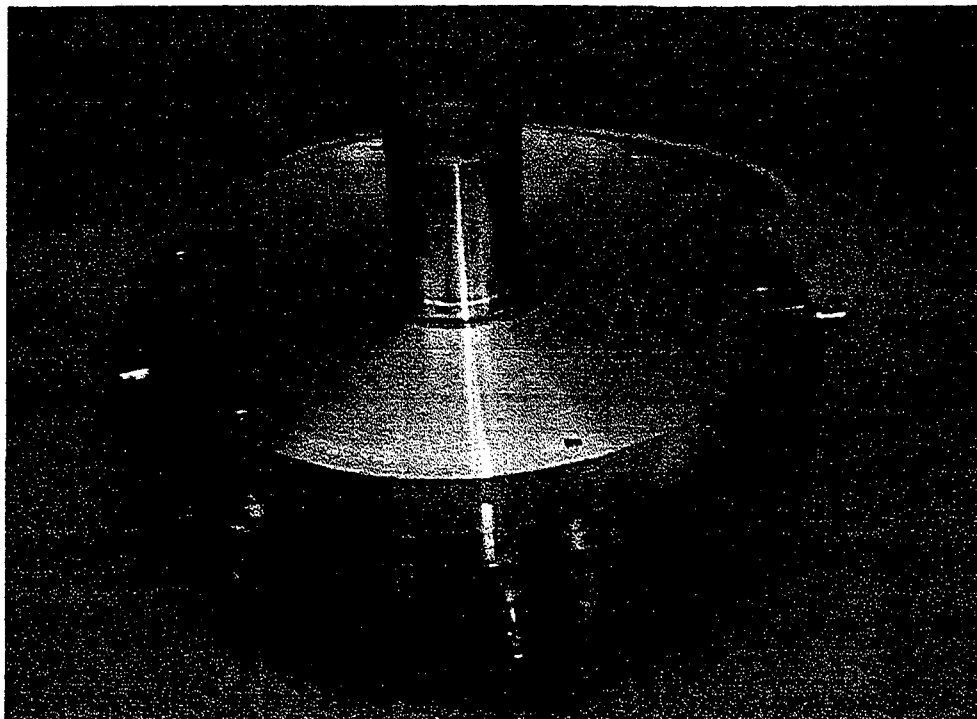
Figure 8.5   The fully assembled extraction system.

8.2   BEAM EMITTANCE

By definition, the beam emittance is related to the pattern that the beam particles occupy within the six-dimensional phase space. In many practical cases the three coordinate pairs within the entire phase space are completely decoupled, and the longitudinal projection of the actual pattern does not have any meaning. Only transverse motions are important. Assuming further that transverse motions are slow compared to the velocity in the beam direction, and non-relativistic conditions are fulfilled throughout, one can substitute the transverse linear momentum $m\, dx\,/\,dt$ and $m\, dy\,/\,dt$ by the tangent values $x' = dx\,/\,dz$ and $y' = dy\,/\,dz$ of the divergence angles for all individual trajectories.

Thus, the commonly used two-dimensional emittance definitions are the patterns that the trajectories independently occupy in the (x, x') and (y, y') planes.

In the case of one round emitting aperture, the plane of interest is (r, r'). The difference between either (x, x') and (y, y') emittance patterns or (r, r') patterns is that in the former two cases all trajectories of a beam are projected into the plane considered while an (r, r') pattern represents a radial half-section through the beam only.

A beam is divergent if its emittance pattern mostly extends from the third into the first quadrant of the coordinate plane, convergent if its major extension runs from the second into the fourth one, roughly parallel if it is extended along the positional coordinate (x, y or r), and it is focused if the emittance pattern runs along the angle coordinate (x', y' or r'). But for real beams the emittance pattern always has a finite width, and therefore there are always some divergent trajectories in an overall convergent beam, Fig. 8.6.
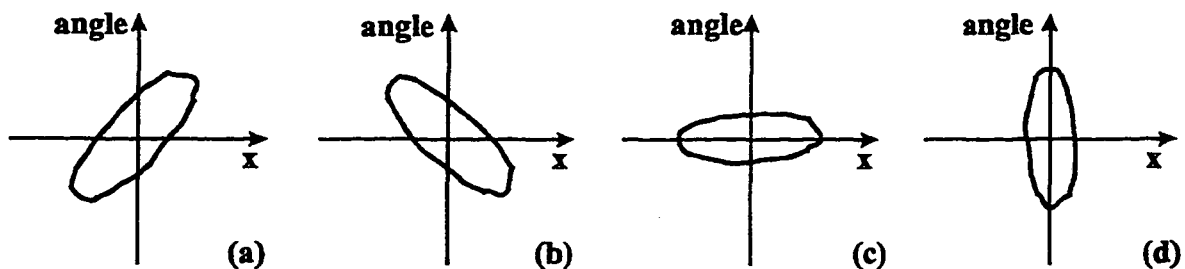
Figure 8.6   Four different cases of two-dimensional emittance patterns. The corresponding beams are roughly divergent (a), convergent (b), parallel (c), and focused (d).

There are two different conventions to quantify the size of an emittance. One can either directly take the area occupied by the emittance pattern and express its size, for example, in units of [mm mrad] or of [m rad]. But in many cases the other convention is followed, that is, to define the size of an emittance value of the area of its pattern, divided

by π. The reason for this second convention is that frequently the emittance patterns are elliptical in shape. Then one can directly deduce the extension of the second semi-axis of this ellipse when the emittance size and the extension of one semi-axis are numerically known. A combination of these two conventions is used to quantify emittance. One takes the actual size as the emittance but writes the π as a distinct factor to it. The emittance unit in this case is [π mm mrad].

The emittance of a beam will shrink if the beam is further accelerated, because for given transverse velocities the longitudinal velocity has increased. To avoid this effect, "normalized" emittances are defined as follows:

$$\varepsilon_n = \beta\gamma\varepsilon \qquad \text{(Eq. 8.1)}$$

where ε_n is the normalized emittance; $\beta = v/c$, ratio of particle velocity to the velocity of light in vacuum; and $\gamma = (1 - \beta^2)^{-1/2}$.

The relativistic parameter β can easily be calculated from the known beam parameters according to

$$\beta = 1.46 \times 10^{-3} (\xi U / A)^{1/2} \qquad \text{(Eq. 8.2)}$$

where ξ is the charge state of the ions, U is the acceleration voltage of the beam measured in kV, and A is the atomic mass number of the ions.

The normalized emittance of a beam is constant, according to Liouville's theorem, as long as only conservative forces are acting and the two planes of observation are truly decoupled.

For a Maxwellian energy distribution, the dependence of the normalized emittance sizes from the ion temperature has been derived for circular apertures as well as for slits.[38] For a circular aperture

$$\varepsilon_{n,4\,rms} = 0.0653\ r\ (kT\ /\ A)^{1/2}\ \ [\pi\ mm\ mrad] \qquad\qquad (Eq.\ 8.3)$$

where r is the aperture radius (mm), A is the mass number of the ions, and kT is the ion temperature (eV), and for a slit aperture

$$\varepsilon_{n,4\,rms} = 0.0377\ s\ (kT\ /\ A)^{1/2}\ \ [\pi\ mm\ mrad] \qquad\qquad (Eq.\ 8.4)$$

The transverse energy of the ion beam can be calculated once the emittance is measured.

8.3   EMITTANCE MEASUREMENT SET-UP

To measure the angle of a trajectory precisely, a two-slit approach is used, also known as Paul Allison type emittance scanner.[39] The schematic diagram of this device is shown in Fig. 8.7. The spatial position of the front slit determines the position of the diagnostic, while the rear slit measures the angle and angular spread of the trajectories passing through the front slit.
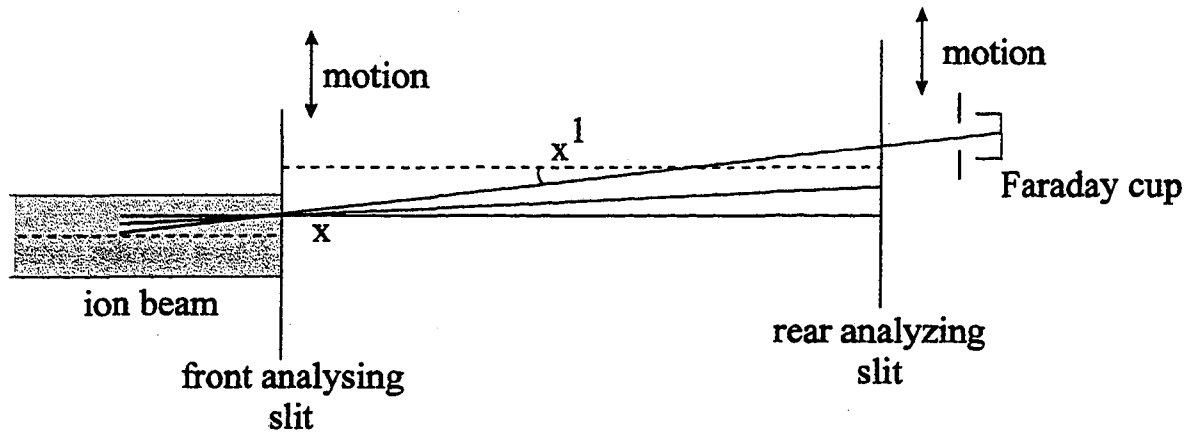
Figure 8.7 The concept of emittance measurement where the position and angle are measured separately.

$$\theta = \frac{V\ell}{2Ud}$$
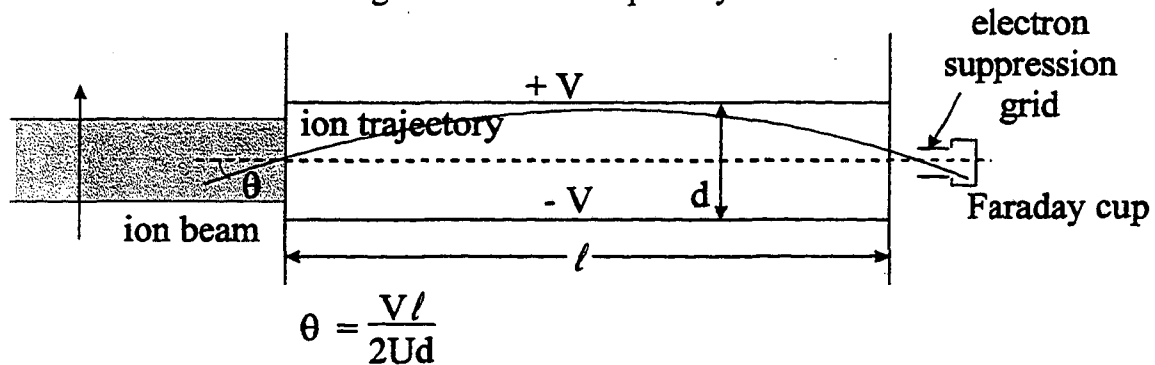
Figure 8.8 The emittance diagnostic, designed by P. Allison, which removes the need for two separate mechanical movements.

An emittance scanner that has been used for testing the co-axial source is also of Allison type. It consists of two parallel plates containing the entrance and exit slits, with a pair of electrostatic deflection plates in between. The first slit separates part of the beam at a certain position x. The particles are then deflected V, the voltage on the deflection plate, which is proportional to x', the derivative of the particle trajectory, and inversely proportional to the particle energy U_0. In our case, the widths and lengths of the two slits are 25 μm and 60 mm, respectively. The distance between the slits is 115 mm, the gap between plates and slits is 0.5 cm and the aperture between the plates is 6.85 mm. This allows a range of measurement of $\pm$ 3 cm in spatial and $\pm$ 110 mrad in angular direction.

Behind the second slit, a collector is used to measure the intensity distribution as a function of x and x'. In front of the collector an electrode is placed, allowing the suppression of secondary electrons. Figure 8.9 shows a picture of the emittance scanner installed inside the vacuum chamber. The emittance scanner is moved on a spindle across the beam. Additionally, the whole unit can be rotated, so that emittance in the x - as well as y-direction are possible.
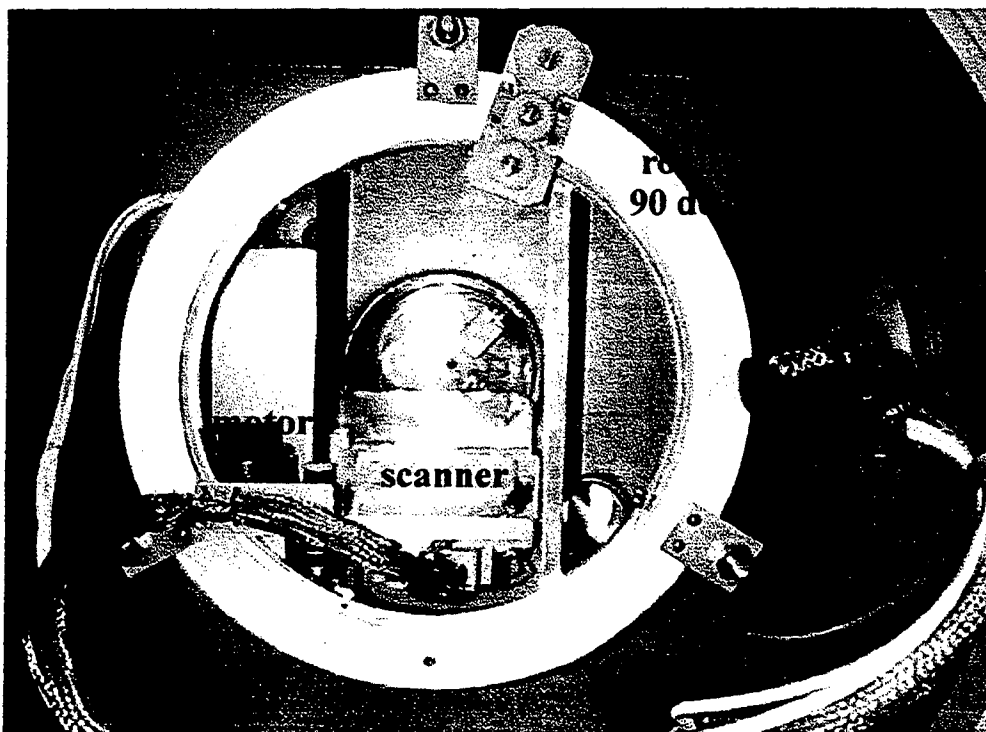
Figure 8.9   Emittance scanner is installed inside the vacuum chamber.

A motor drives the scanner vertically, and the system can be rotated 90°. The motor is connected to an indexer and a power supply outside the vacuum chamber. A computer software written in Labview has been developed at Lawrence Berkeley National Laboratory to control the necessary equipment and to acquire data. Besides the motor, indexer and power supply for the motor, two bi-polar Kepko power supplies for

the upper and lower deflection plates, one negative power supply for biasing the suppresser slit, a current amplifier, a CAMAC rack, and two Macintosh computers are part of the complete emittance scanning system. A schematic diagram of the setup including the computers is shown in Fig. 8.10.
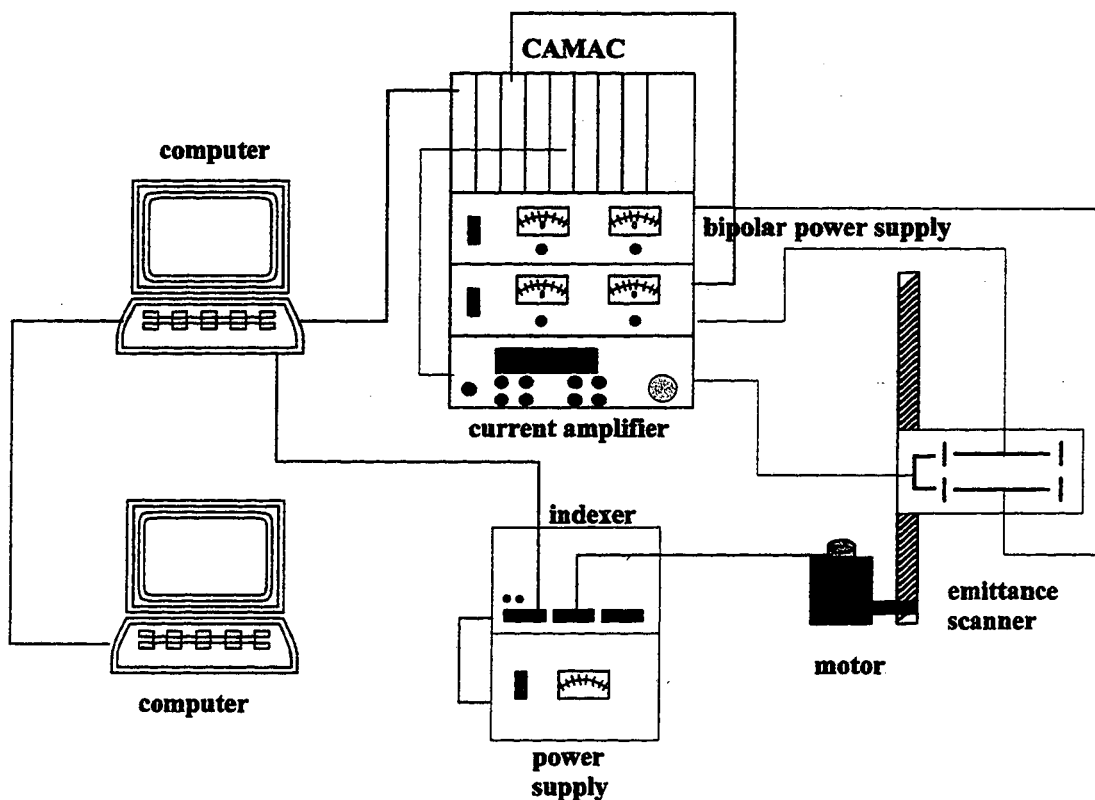
Figure 8.10   Schematic diagram of the emittance measurement setup.

The graphical interface of the emittance scanning program is also written in LABVIEW. The scanning area, angular and axial divisions can be adjusted in this program. The plot on the right hand side of Fig. 8.11 shows the area of scan, x, x' or y, y' (in cm and milliradians, respectively). The plot on the left hand side of Fig. 8.11 shows the intensity of the beam versus the angle as it is taken at a certain position (in arbitrary units and radians, respectively). Emittance measurements for pulsed beams can also be

made, in which case it is possible to measure the emittance at different parts of the pulse, i.e. beginning, middle, end, etc.

Figure 8.11   User interface for emittance measurement.

The measured emittance plot is displayed in another software, also written in LABVIEW. In the following section, results of the co-axial source emittance measurement is presented.

8.4   EMITTANCE MEASUREMENT RESULTS

The beam emittance of the co-axial source with the designed accelerator has been measured. At a discharge power of 320 Watts, the measured rms. emittance was found to be 6.565×10^{-5} [m rad]. The beam emittance is plotted in Fig. 8.12. The units for the y-axis is in mrad and x-axis is in cm. Beam profile can be displayed at different position

indicated by the yellow line in the emittance plot. Normalized emittance, in this case is

1.516×10^{-7} [m rad] by using the equations 8.1 and 8.2.
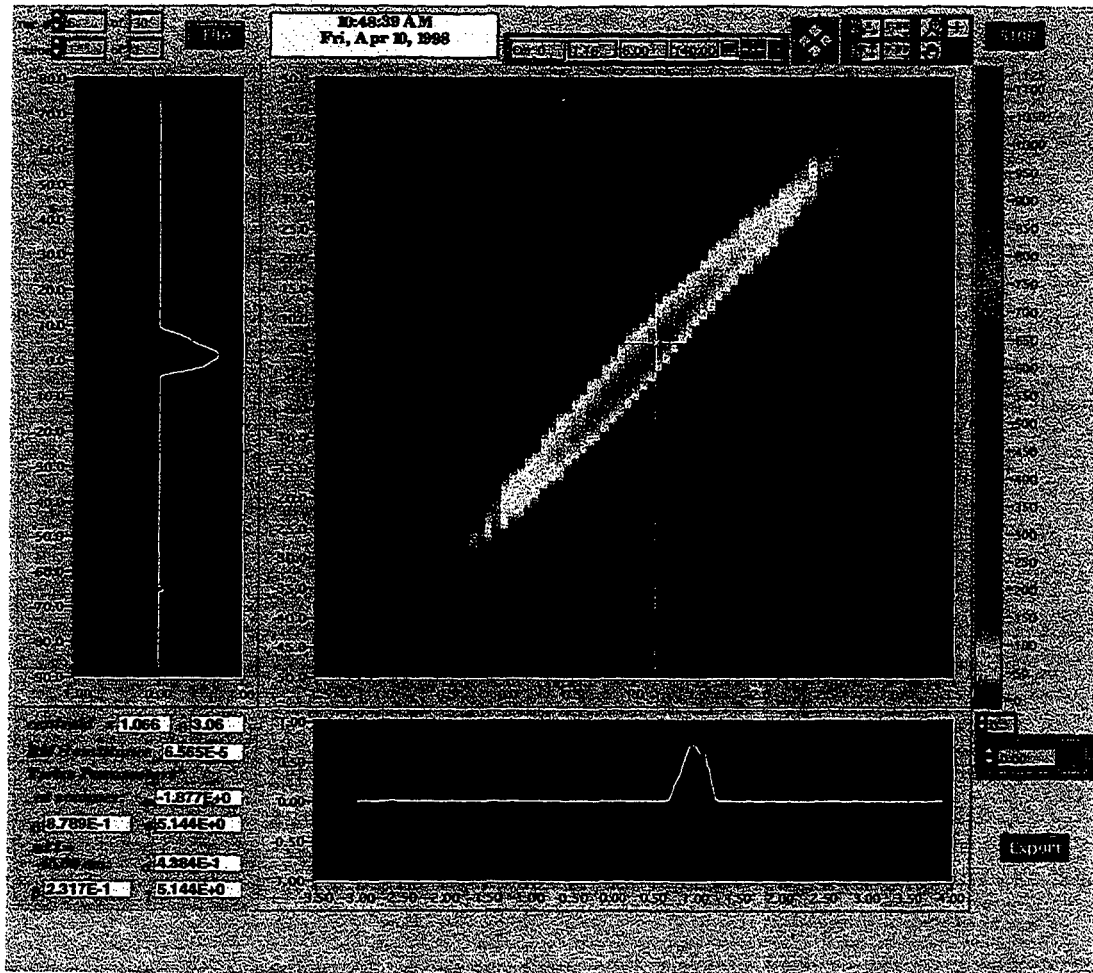
Figure 8.12   Emittance was measured with the designed accelerator and
the co-axial source.

A concern with the co-axial source is the fact that the radial plasma potential

distribution is not uniform. The transverse ion energy is suspected to be larger than the

regular ion source configuration. A small plate was placed in the center region. This plate

was electrically-isolated from the rest of the source. A dc power supply was used to bias

the plate and the source chamber in order to adjust the plasma potential distribution in the center region, Fig. 8.13.
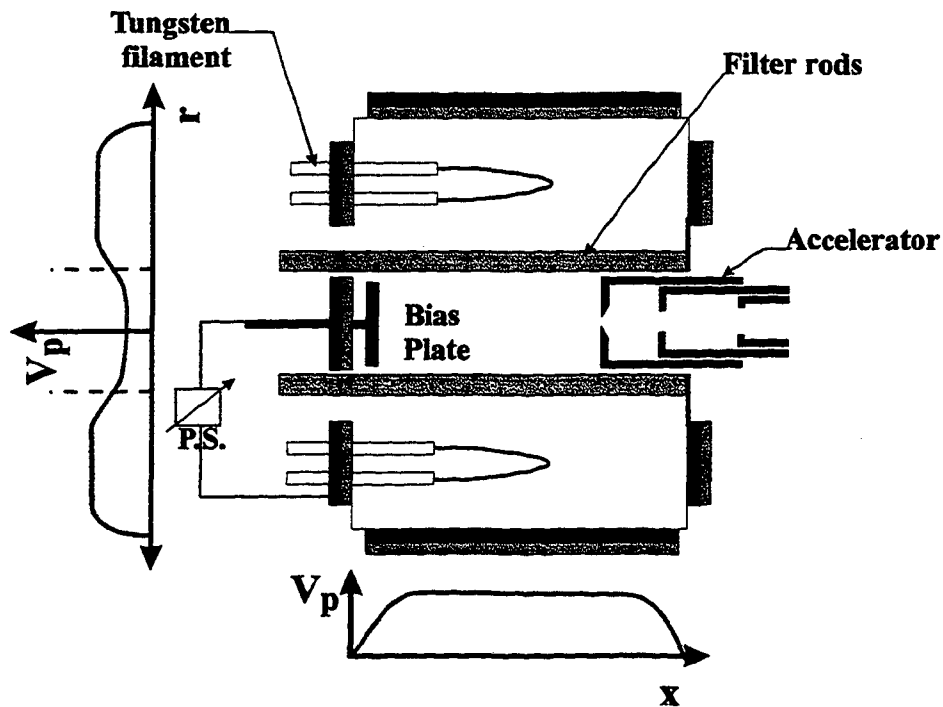
Figure 8.13   Bias plate is used for radial plasma potential distribution adjustments.

A thorough study of the biasing effect is beyond the scope of this dissertation work. However, preliminary testing shows that the emittance is improved when the plate is biased one or two volts more positive with respect to the source chamber. Without any bias, the emittance is 6.565×10^{-5} [m rad]; with a 2 V bias, the emittance is reduced to 5.805×10^{-5} [m rad]. On the other hand, when the plate is biased few volts more negative than the source, the emittance increased slightly to 1.426×10^{-4} [m rad]. A plot of bias voltage versus measured emittance is shown in Fig. 8.14. This measurement was taken under the same discharge condition: 320 watts discharge power, 1 mTorr hydrogen gas pressure, 5 kV beam energy.
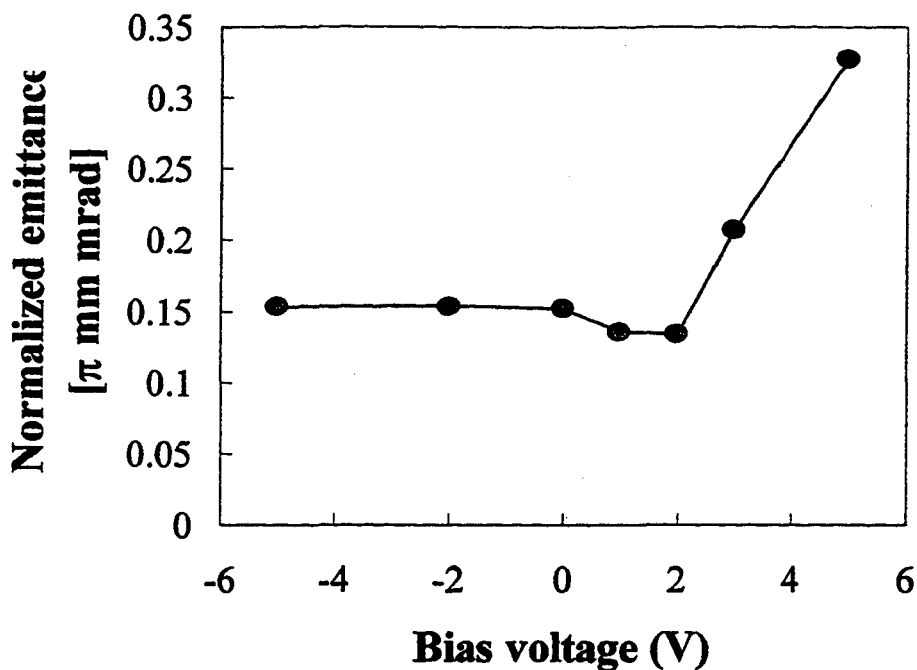
Figure 8.14 Normalized emittance at different bias voltage is shown. The emittance is minimum at two volts bias.

At a negative bias the emittance is almost unchanged, because the plasma potential difference between the center and the outer discharge region is about the same. However, when the plate is biased 1 ~ 2 volts more positive, the plasma potential difference between the annular and the center region is reduced. The transverse temperature of the ion decreases, and therefore, the beam emittance is improved.

When the plate is biased too positive ($V_{bias} > 2$ V) , as is the case in Fig. 8.16, the plasma finds it more difficult to cross the filter, and instability will build up to drive the ions together with the electrons into the central region. As a result of this instability, the transverse temperature of the ions will increase thus yielding a larger emittance. The

results shown in Fig. 8.16 indicate that the beam emittance indeed is larger than the case of $V_{bias} = 0V$.

Leveling of the plasma potential distribution by the use of a biasing plate was proven to be effective in reducing the emittance value. Further study will be needed to determine the length of its influence which is beyond the scope of this dissertation and will be left for future works.
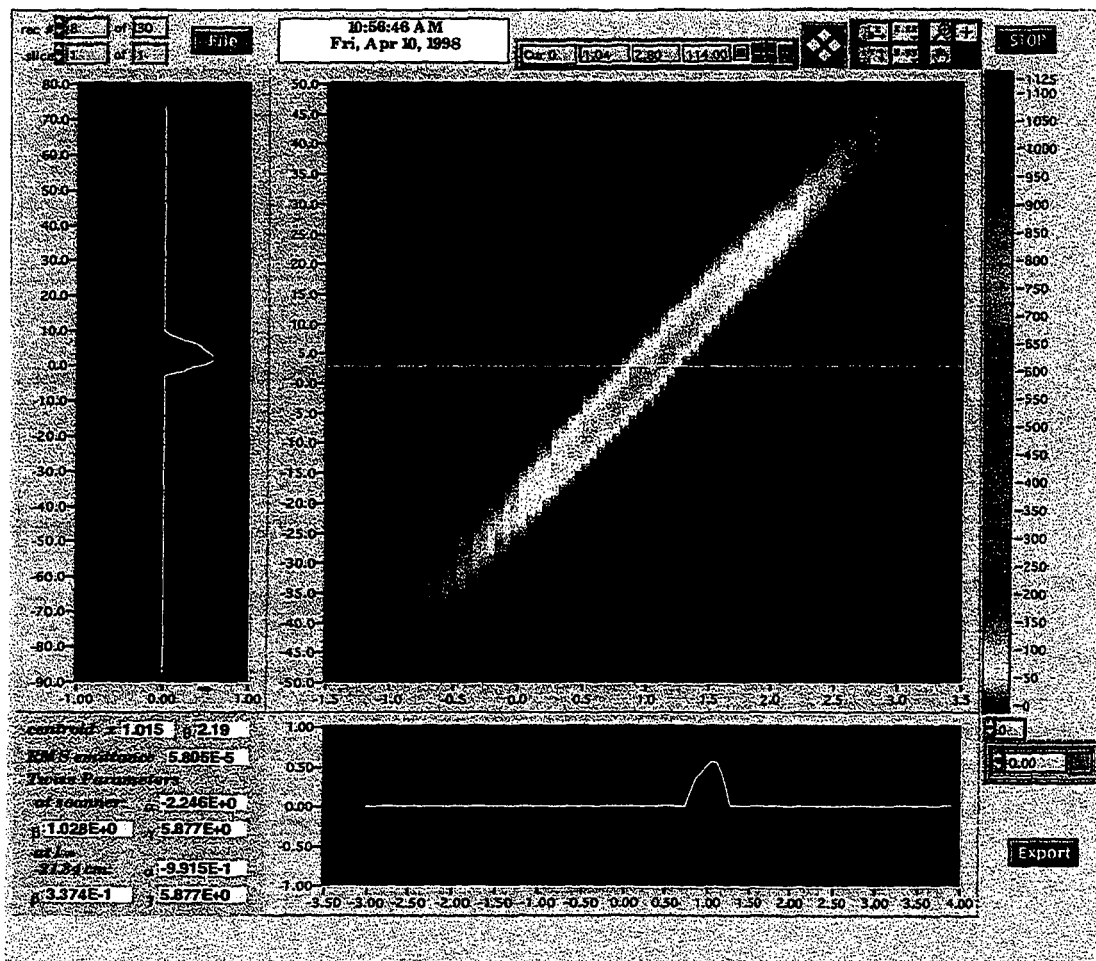
Figure 8.15   Emittance plot with 2 V plate bias.
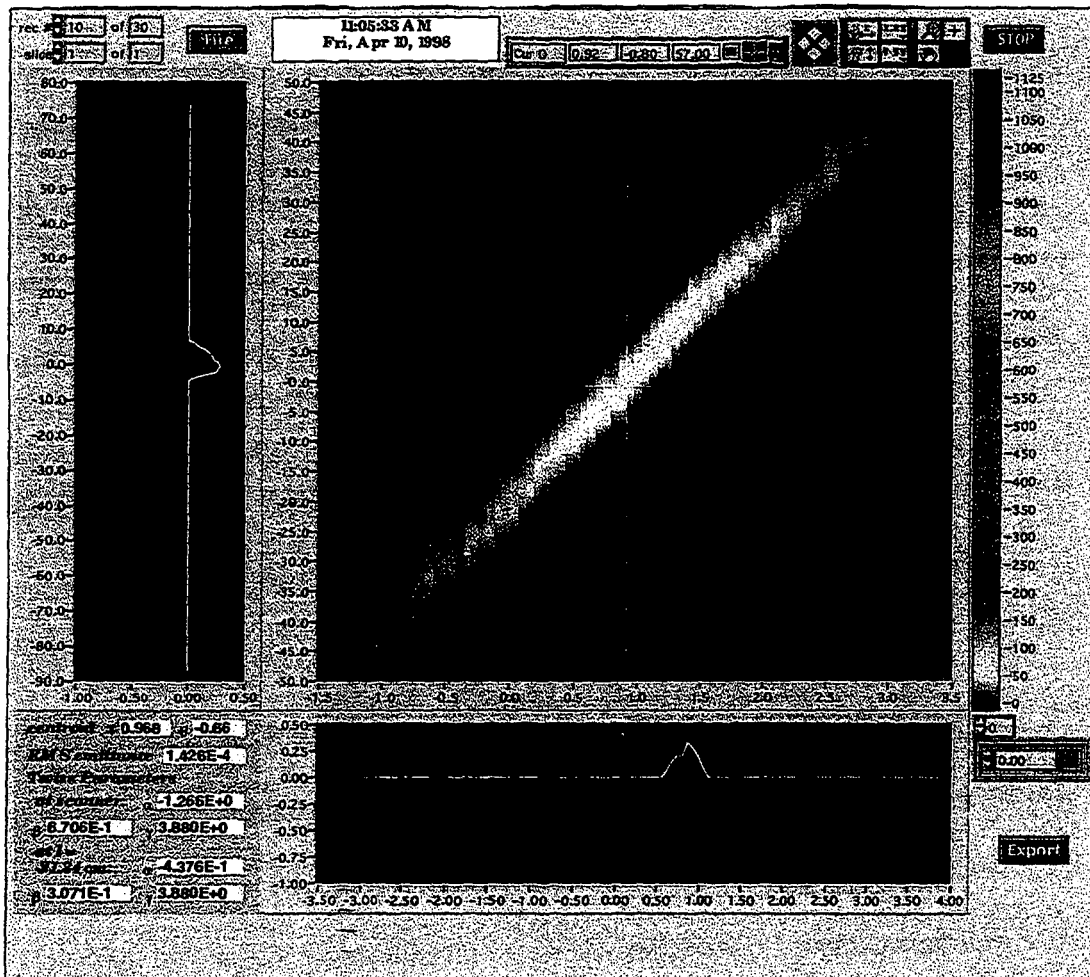
Figure 8.16   Emittance plot with a 5 V bias.

CHAPTER 9

ION SOURCE LIFETIME ISSUES

Ultimately, the ion projection lithography machine requires the ion source to have at least 2000 hours of operation between routine maintenance. Such demand is overwhelming for the filament driven source, especially when the accelerator design requires a very high source operating power. Some solutions are presented in this Chapter.

9.1 LIFETIME ENHANCEMENT BY IMPROVING THE ACCELERATOR DESIGN

The three-electrode extraction system for the IPL tool designed by the Advanced Lithography Group (ALG) is insensitive to small changes in density. The beam is extracted with an underdense condition with a beam cross-over located near the plasma electrode. This system is designed for the generation of an expanding beam. The machine operates with a "useful" beam current of 20 µA within a 3° cone (half angle, 55mrad).

The "useful" beam current was measured by placing the Faraday cup behind the hole of the collimator plate as illustrated in Fig. 5.4. Fig. 9.1 shows this Faraday cup current, the collimator current and the total beam current (sum of Faraday cup and collimator current) as function of discharge current for the 10-cm-diameter, 20-cm-long source. In this measurement, the gas pressure is maintained at 8 mTorr.
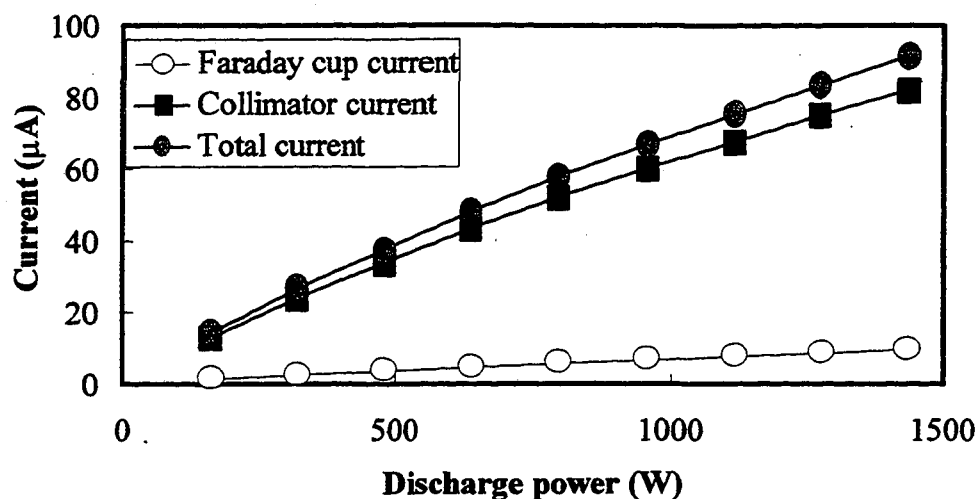
FIGURE 9.1 The Faraday cup current, the collimator current and the total current as functions of discharge current.

With the original accelerator design, approximately 10 % of the total beam current falls within a cone of six degree angle. Through extrapolation of the results in Fig. 9.1, it can be seen that discharge powers as high as 3 kW will be required for the source to provide a Faraday current of 20 μA. Such high discharge power results in fast erosion of the tungsten filament, which in turn will shorten the lifetime of the source operation. Furthermore, tungsten can be deposited on the small extraction aperture which can modify the aperture size and geometry. As a result, both the ion optics and extractable current will be changed.

The extractable ion current of the multicusp source was also examined at a pressure of 8 mTorr for the 10-cm-diameter by 10-cm-long source. A "useful" beam current of 20 μA can be achieved quite easily compared to the 20-cm-long source. As shown in Fig. 9.2, 26 A of discharge current is enough to produce 20 μA of beam current at the Faraday cup. This result indicates that the shorter source is indeed more efficient

than the longer source and is a better source candidate for IPL. However, the longer

source can be operated at a lower gas pressure than the short source.[41]
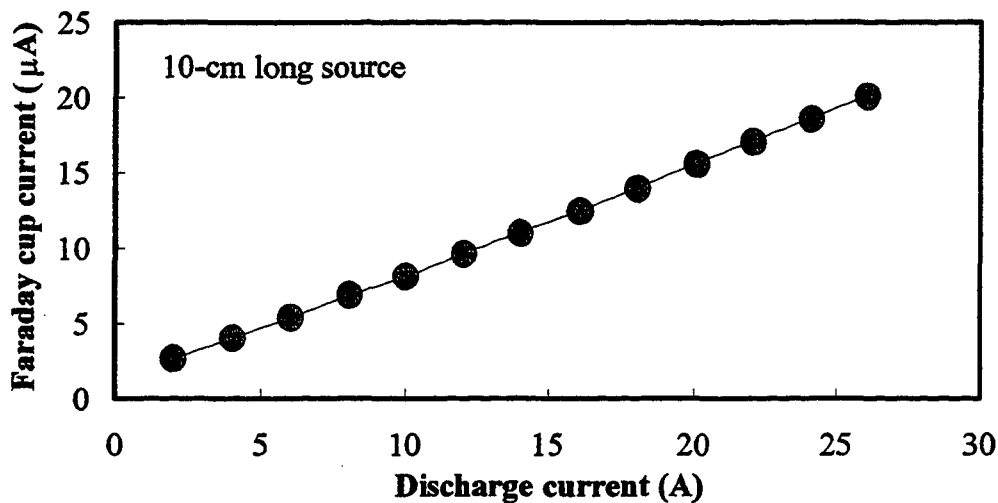
FIGURE 9.2 The Faraday cup current as a function of discharge
current for the 10-cm-long source at a   discharge
voltage of 80 V.

With the original accelerator system, the ion source must provide a total current of

approximately 200 μA (80 mA/cm^2). The beam has a focal (or cross-over) point outside

the source between the first and second electrodes. At higher ion beam currents space

charge force (the Boerch effect[42]) can increase the ion energy spread of the accelerated

beam. Fig. 9.3 shows the IGUNE simulation of the accelerator design for the ALG IPL

machine. The beam divergence is approximately 180 mrad (half angle), and there is only

a small clearance between the ground electrode and the edge of the beam.[43]
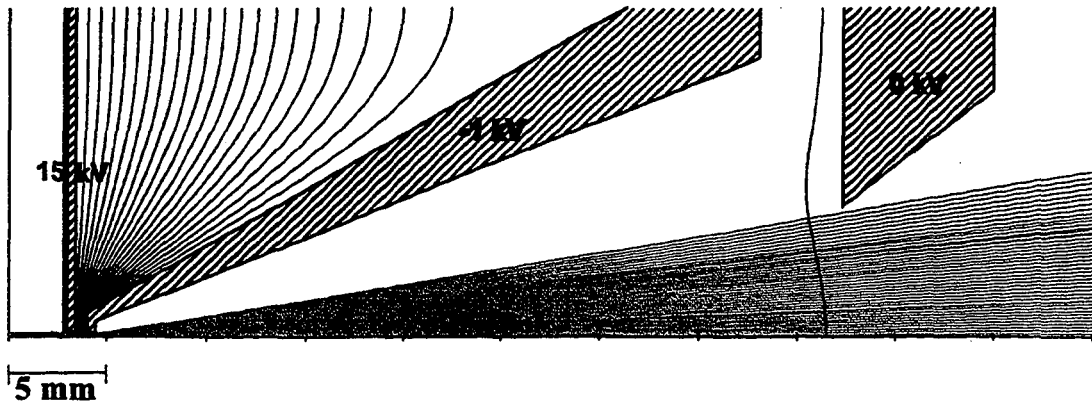
FIGURE 9.3a IGUNE simulation of the original (ALG-1000, IPL tool) design for a current density of 80 mA/cm². The beam has a focal point about 4 mm from the electrode.
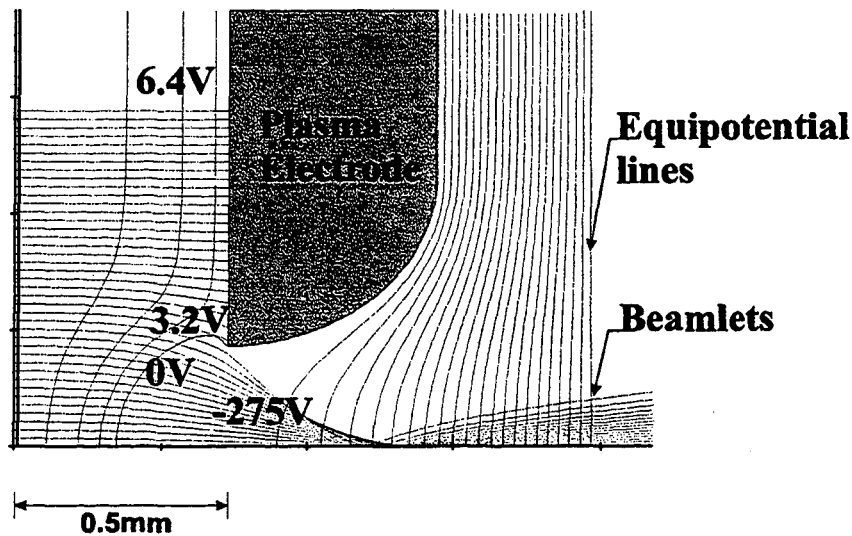
FIGURE 9.3b The beam cross over is shown to be near the first electrode. The voltage values are relative to the plasma electrode.

Computer simulations using an ion trajectory code, IGUNE, have been performed with the goal of increasing the useful beam fraction. If the required ion beam current density is reduced, it will allow the ion source to be operated at a lower discharge power.

For this purpose, the divergence of the beam is decreased by increasing the distance between the first and second electrodes.

Fig. 9.4 shows the simulation of the system with an increased extraction gap and a current density of only $20mA/cm^2$, that is about a quarter of the original design. The total beam divergence is changed to 90 mrad. The focal point is now approximately 4.15 mm from the first electrode, and the current within the 3° cone is approximately 24 μA. This adjustment does not increase the sensitivity of the ion optics to changes in source plasma density because the extraction is still operated at an underdense condition. At 80 mA/cm^2, the beam divergence is approximately 100 mrad, and the current within the cone is about 104 μA.

`5 mm`
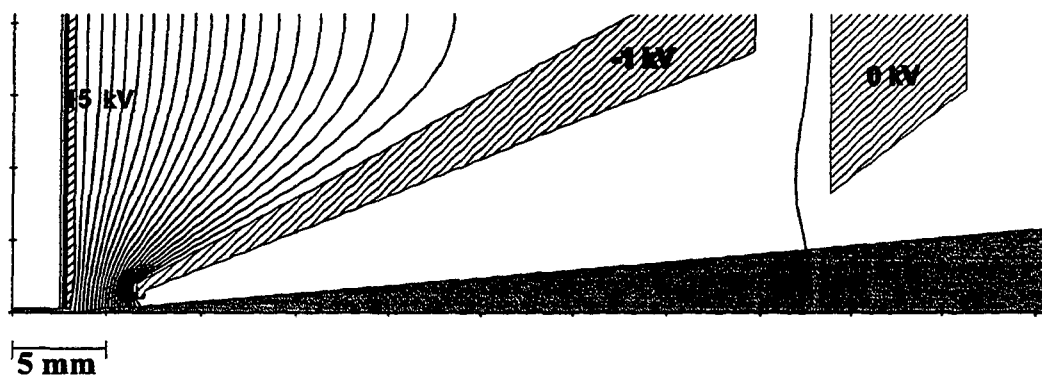
FIGURE 9.4 IGUNE simulation of the original design at 20 mA/cm^2 and with an increased gap. The beam has a focal point about 4.15 mm from the electrode.

Fig. 9.5 shows the ion trajectories when the extraction hole is increased from 0.3 mm to 0.4 mm, and the current density is 10 mA/cm^2. The focal point is located at ~ 4.26 mm away from the exit plane. The current within the cone is approximately 24 μA, and the beam divergence is about 80 mrad. This configuration will allow the ion source to operate at a low discharge power. Lower discharge power (~ a factor of eight reduction)

will lead to longer filament or source lifetime. In addition, lower beam current at the

cross-over will keep the energy spread low. A summary of these different simulations is

shown in Table 1.
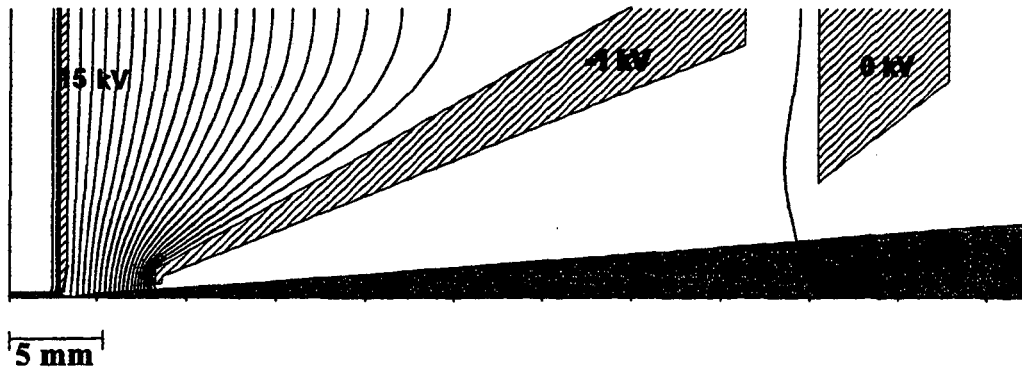
FIGURE 9.5   IGUNE simulation of the original design at 10 mA/cm^2
and with an increased gap. The extraction hole was
increased from 0.3 mm to 0.4 mm. The beam has a
focal point about 4.26 mm from the electrode.

Case	Changes	Hole diameter (mm)	Current density (mA/cm^2)	Beam divergence (mrad)
1	Original	0.6	80	180
2	Increase distance between first and second electrodes	0.6	20	90
3	Increase diameter and distance	0.8	10	80

TABLE 1   Summary of three different extraction designs.

9.2 LIFETIME ENHANCEMENT BY RF INDUCTION DISCHARGE

Tungsten-filament driven sources have shown to have low ion axial energy spread ion beams. However, tungsten evaporation and ion sputtering can eventually limit the filament lifetime. Evaporation of tungsten material from the filament cathode can also modify the shape of small exit apertures, and thus the beam uniformity and extractable current. On the other hand, radio-frequency (RF) induction discharges have a long operational lifetime, and provide a clean discharge plasma. In an RF-driven ion source, an induction coil or antenna is used for the discharge. The induction coil can be either placed inside or outside the ion source chamber. RF-ion sources developed at Lawrence Berkeley National Laboratory (LBNL) have the antenna coil located inside the chamber and can be operated either in pulsed or CW mode.

The ion energy spread of the RF-driven multicusp source has been measured. It is found to be comparable to that of the filament-discharge source (Fig. 9.6). This makes the RF-driven multicusp source suitable for IPL applications.
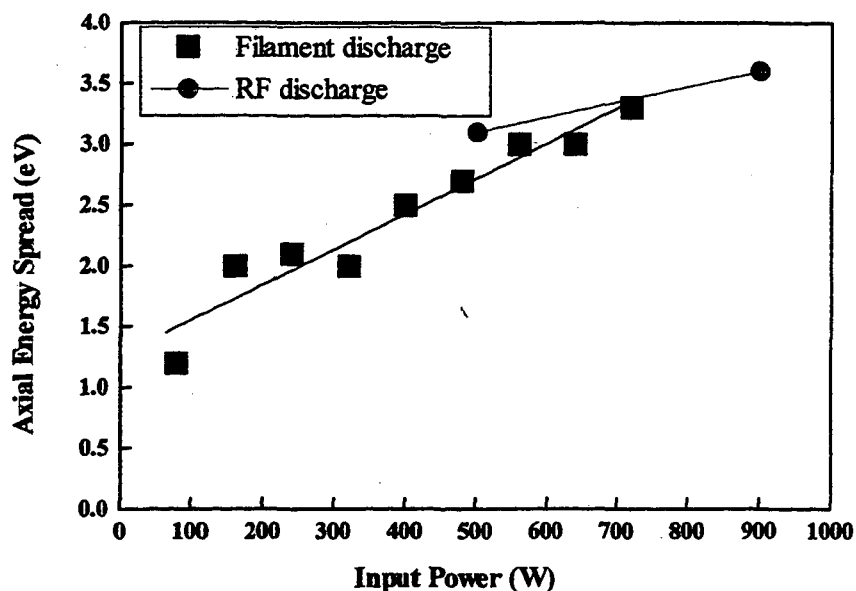
FIGURE 9.6 Energy spread for RF and filament sources as function of power.

The RF-induction coils can be made of different materials. For example, metals such as copper, aluminum, titanium have been used for making the antenna. They can be operated either with or without a porcelain or glass coating. The porcelain-coated antenna, shown in Fig. 9.7, can withstand the ion bombardment from the plasma. A coated antenna is more efficient in plasma production because it prevents the antenna current from being short-circuited between the two legs. It has been demonstrated that a porcelain-coated antenna coil can be operated with various types of plasmas.

Porcelain-coated antennas have been tested in hydrogen plasmas under CW operations for up to 20 hours at RF input power of 10 kW and tens of minutes at 20 kW, without any sign of degradation of the antenna coating. At lower power levels (~5 kW),

antenna lifetime in excess of 260 hours have been reported.[44] At low duty factor pulsed operations, lifetime of this kind of antenna can exceed 500 hours.
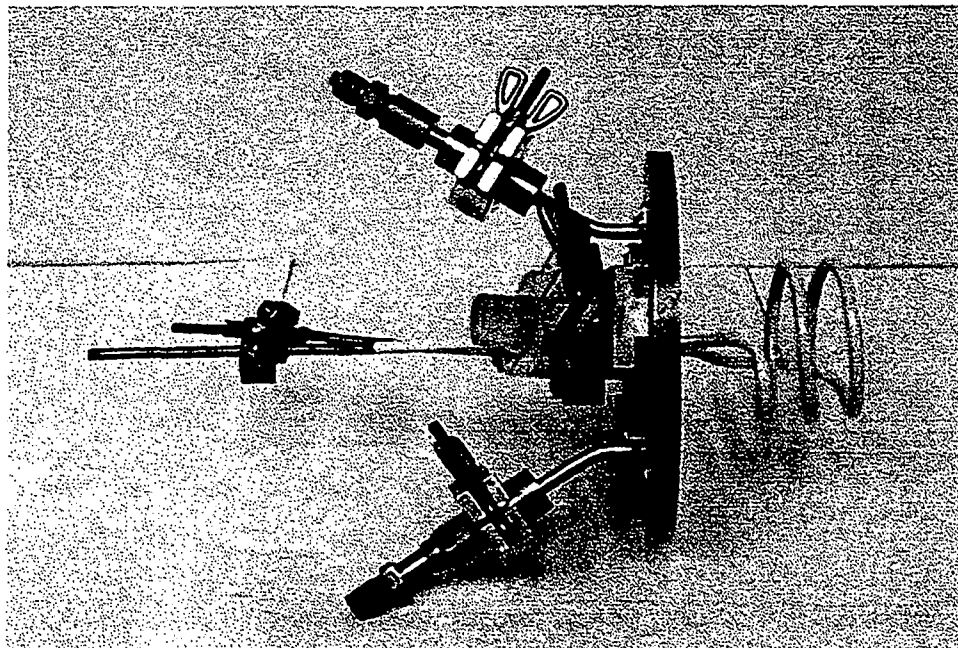
FIGURE 9.7 A porcelain-coated antenna is mounted on the backflange of the multicusp source.

With the increasing RF power requirements and different plasma conditions, even the porcelain-coated antenna can sometimes fail to perform satisfactorily. For instance, in some plasma experiments, oxygen is used as the feeding gas, and the porcelain antenna cannot last more than 10 hours of continuous operations.[45] Similar problems also arise when the source is operated in pulsed-mode without cooling. Due to the high temperature gradient, an uneven thermal expansion occurs between the porcelain coating and the copper surface. As a result, the porcelain coating peels off. A new antenna design using quartz tubing has been investigated. This quartz antenna can provide a much longer lifetime and cleaner operation of the ion source. Sec. 9.3 provides a detailed description of this new antenna configuration.

9.3   QUARTZ ANTENNA FOR RF-DRIVEN SOURCE OPERATION

9.3.1   QUARTZ ANTENNA FOR SMALL ION SOURCES

During the development of a compact ion source for sealed neutron tubes, a regular porcelain-coated copper antenna was used. This antenna was fabricated out of copper tubing 3 m in diameter, and wound to form 2.5 loops of ~ 1.5 cm in diameter. The turn to turn spacing between the induction coils was approximately 0.7 cm. The insulating porcelain coating can be deposited either with plasma spraying or by dipping the metal coil in a molten bath. For this particular application, the antenna could not be water cooled, though this was acceptable given the low duty factor (<1%) operation. The antenna was driven at a frequency of ~ 2MHz and pulsed RF powers up to 70 kW to achieve plasma pulse widths of approximately 10-20 μs at repetition rates of up to 50 Hz.[46]

To achieve a long lifetime and cleaner operation of the small multicusp source, a 3-mm OD and 2-mm ID quartz tubing has been wound in the shape of the multi-turn induction coil as shown in Fig. 9.8. The size and the shape is adjusted so as to satisfy this particular application. Silver-coated copper wire strands are threaded inside the tubing to serve as a conductor. There are advantages of using several stranded wires instead of a single one. Typically, the resistive heating of a glass tube antenna will be higher than for conventional copper tube antennas of comparable outer diameter. Conventional copper coil antennas use copper tubing with an outer diameter typically greater than 5 mm. A glass tube antenna with the same outer diameter would have a smaller inner diameter.

Additionally, since space should preferably be preserved for the flow of coolant, the conductor size is further limited.

Moreover, at high RF frequencies, the effective cross-sectional area for electrical current flow is still further reduced. Classical electromagnetic theory teaches that at high frequency the current distribution in a wire decreases exponentially with a characteristic length δ, or skin depth, from the surface. The skin depth varies inversely as the square root of the frequency and the conductivity of a metal. For example, at a frequency of 1 MHz, the skin depth of copper decreases to 66 μm.

Due to the skin depth at the desired RF frequency, the ratio of the cross-sectional area available for RF conduction compared to the cross-sectional area of the individual wire is increased. The conductive cross-sectional area of a wire of outer radius, r, conducting in a thin outer annulus corresponding to the RF skin depth, δ, is:

$$\pi(r^2-(r-\delta)^2)=2\pi r\delta-\pi\delta^2 \qquad \text{(Eq. 9.1)}$$

Dividing this expression by the copper area, πr^2, gives the ratio of cross-sectional area available for RF conduction compared with the actual copper area, which is $2\ \delta/r\ -\delta^2/r^2$. This ratio rapidly increases when the radius of the wire is reduced in magnitude to approximately several times the skin depth. In the quartz antenna tested, 19 wires, each having an outer diameter of 0.0075" (190 microns) are used in a glass tube. At a frequency of 1 MHz the radius of the wire (96 microns) is approximately one and a half times the skin depth (66 microns) such that a large fraction of the copper acts as an RF conductor.
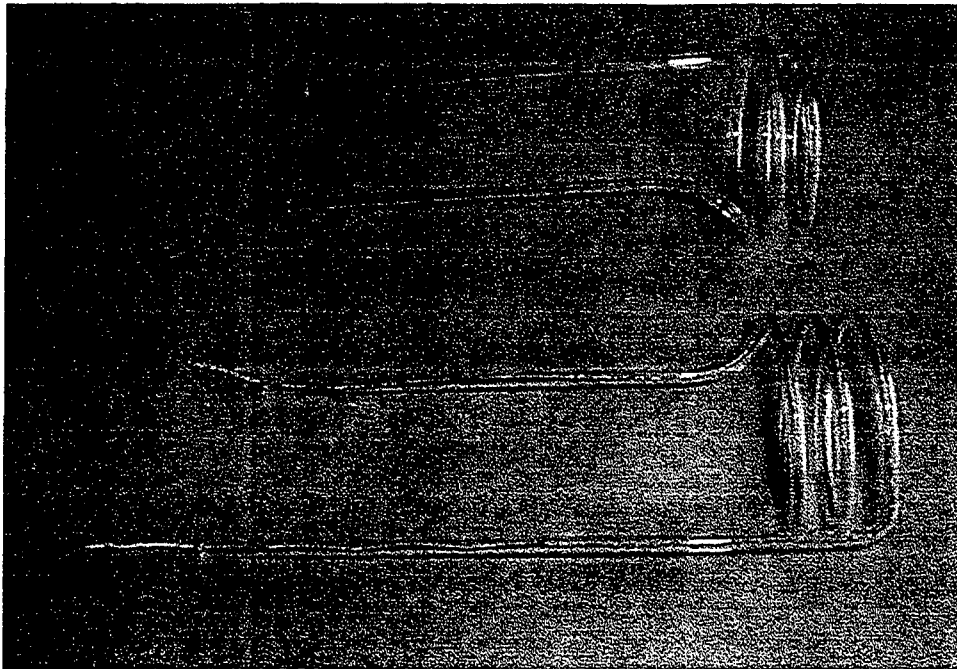
FIGURE 9.8 A silver coated copper wire strand is threaded inside the tube and will eventually be connected to the matching network.

Connection to the wires are made outside the vacuum. The quartz antenna is used as an RF coupler immersed in the source plasma in a compact ion source for neutron generation. Only the quartz is exposed to the vacuum or plasma. For short pulse and low duty factor source operation no cooling is needed. Connections to the wires are made outside the vacuum chamber leaving the inside of the tubing exposed to atmosphere.

With a standard "uncooled" porcelain coated antenna, half a dozen or more small black pits on the coating are observed after several tens of hours of operation. These pits are attributed to RF arcing. Undetected cracks in the porcelain coating create weak points from which this pitting can initiate. In the absence of a starter filament to aid in the discharge breakdown, large voltages (on the order of kilovolts) repeatedly develop across the antenna coating. This electrical stress, as well as thermal stress, when concentrated on

the micro-cracks can lead to pitting. As the number of pits increases, RF-power coupling to the plasma becomes unstable. Signal jumps are observed in reflected power readings.

Source operation without cooling of the-quartz antenna (under similar conditions as the porcelain-coated antenna) shows no sign of wear for several dozens of hours of discharge operation. The large insulation thickness compared to the porcelain (<0.5mm) prevents voltage arcing, and thus improving the lifetime and performance of the RF-driven source.

9.3.2 QUARTZ ANTENNA FOR LARGE ION SOURCES

RF-antennas have been tested in CW mode operations in a 10-cm-diameter by 10-cm-long multicusp ion source. In this 10-cm-diameter multicusp source, two antenna configurations, porcelain-coated and quartz tubing with conducting wires, have been employed. The copper RF-antenna has been fabricated out of a tubing 5-mm OD and 3-mm ID, with a thin porcelain layer on the outer surface. For the quartz RF-antenna, a 5-mm OD and 3-mm ID quartz tube has been wound to form a 2.5 loops of ~ 6-cm in diameter (same size as the porcelain-coated antenna). Silver-coated copper wire strands have been threaded in the tubing to serve as a conductor. Both types of antennas were water-cooled.

Further protection of the fragile portion of the system, mainly the quartz tubing, is provided by using plastic fittings as shown in Fig. 9.9. and Fig. 9.10. The RF supply is at a fixed frequency of 13.56 MHz with a maximum output power of 2.5 kW. The RF power is coupled into the plasma through the matching network which is also connected to the

antenna fitting. The antenna connections can be seen in Fig. 9.9. It shows how the external portion of the quartz antenna is protected for CW operation.
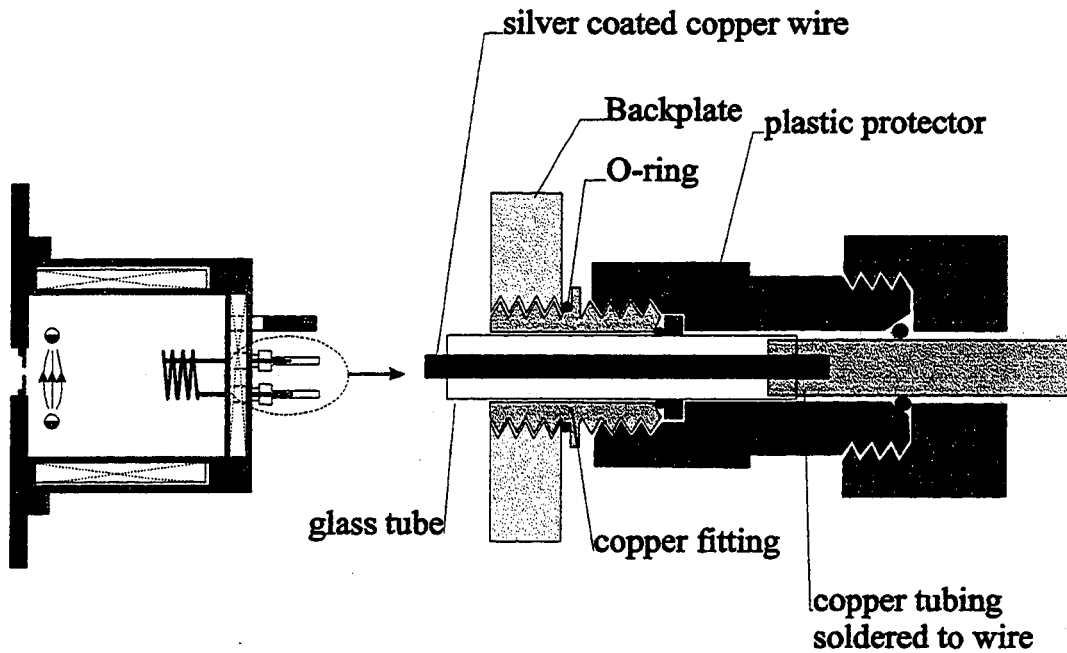
FIGURE 9.9 Further protection of the fragile portion of the system, mainly the quartz, is provided.
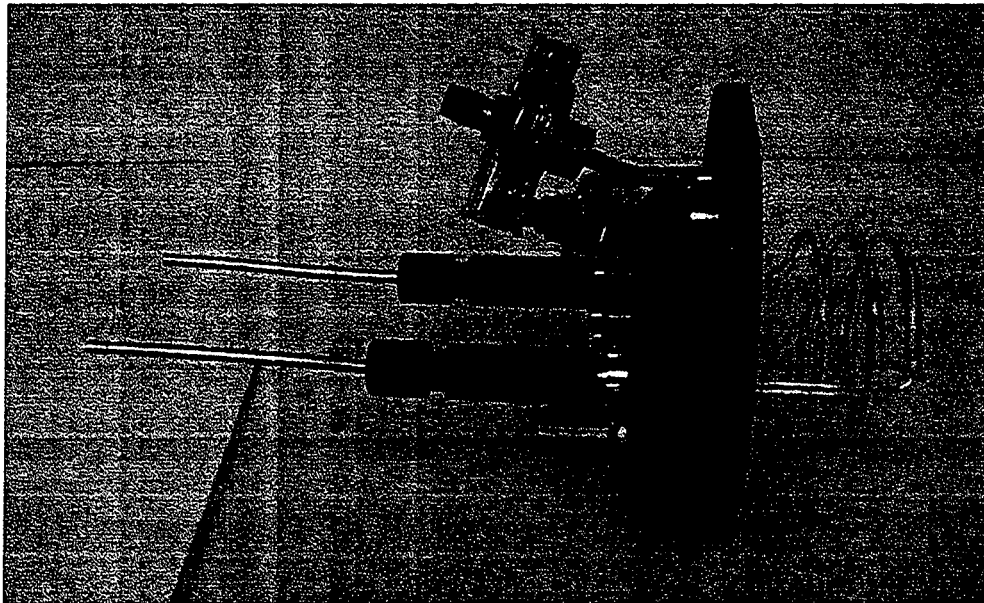
FIGURE 9.10 The antenna assembly is installed in the backflange of the multicusp source.

Extractable current measurements for the two antenna configurations have also been performed in the 10-cm-diameter source using the three electrode extraction system.

The water-cooled porcelain-coated antenna has been operated with oxygen in the 10-cm-diameter source chamber. An RF-power of approximately 2 kW was applied to the antenna. After approximately 10 hours of operation, unstable plasma conditions could be observed. Forward and reflected RF power readings became unstable. Portions of porcelain coating on the copper antenna had flaked away and burn marks were present. Furthermore, the chamber wall was coated with an insulating film.

The porcelain-coated copper antenna was then replaced with a quartz antenna, and it was tested under similar discharge conditions. Results showed that the lifetime performance of the quartz antenna was better than the porcelain-coated antenna. Initially, the quartz antenna was operated with argon as the feeding gas at 1.8 kW for over 85 hours. No visible physical change could be observed on the antenna surface. The stranded wire and the quartz tubing were in good condition. The inside of the source chamber wall was clean and no insulating film was detected.

The quartz antenna was subsequently operated with oxygen plasma for more than 15 hours (compared to the failure time of less than 10 hours for the porcelain coated antenna) at 1.8 kW. No physical change was seen on the antenna that could interfere with normal operating conditions. In addition, the same antenna has been operated with a molybdenum liner inside the wall to increase the surface temperature. No damage was seen after over 10 hours of CW operation.

For uncooled CW operation, concerns have been raised on the quartz breaking inside vacuum due to the absence of water cooling through the tube. However, this issue

can be dismissed because the conducting wire will break before the quartz tubing reaches a high temperature. The wire inside the tube will break in less than one minute of operation without cooling, and this can immediately be detected through the reflected power reading of the RF-power supply.

Current extraction measurements for the quartz and the porcelain coated antennas have been performed. Argon has been used to form the plasma at a source pressure of 10 mTorr. Under the same source discharge conditions, the quartz antenna is as efficient as the regular porcelain-coated antenna. Efficient discharge is improved with the new antenna coil because electrical short-circuit between the antenna legs is avoided. In this arrangement, the quartz tube wall is a more effective insulating layer than the thin porcelain layer.

9.3.3 COMPARISON OF QUARTZ AND PORCELAIN COATED ANTENNA IN PULSED-MODE OPERATION

The performance of both types of antenna has been compared in pulsed-mode operations. Several parameters were examined, including minimum starting pressure and the peak extractable current density. Other than antenna lifetime, the performance of both types of antenna was found to be similar. Fig. 9.11 shows a plot of the peak extractable hydrogen current density as a function of RF-driving power at a source pressure between 2.5 and 3 mTorr. From this figure, it can be seen that the peak extractable current densities, hence the plasma densities, vary less than 10% between the two types of

antenna. Similarly, the minimum starting pressure for the quartz and porcelain antennas was found to be approximately 1.5 mTorr.

Presently, the quartz antenna is being tested at Paul Scherrer Institute (PSI, Switzerland) for high power CW operation. If the results are successful, this new antenna arrangement can provide a long-life CW discharge operation for cyclotron applications.
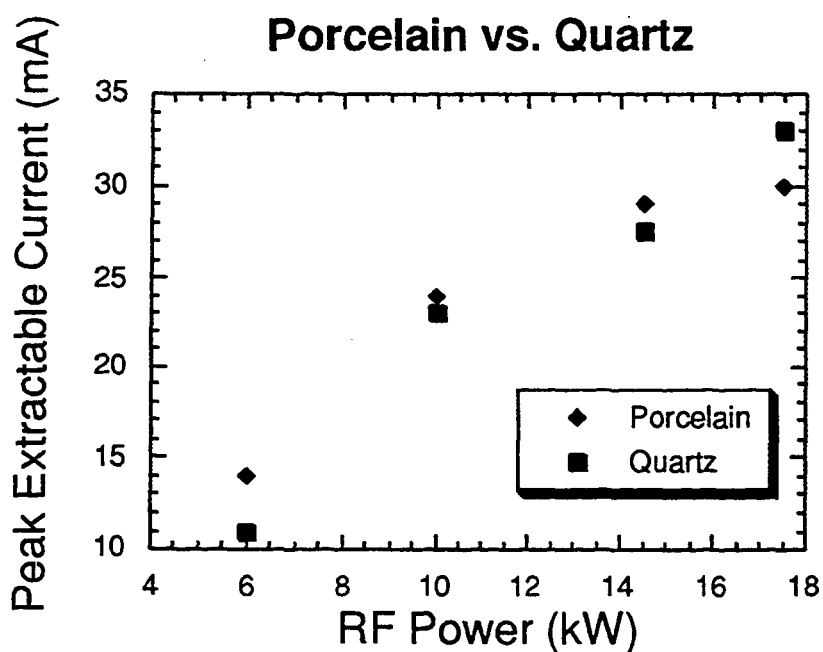
FIGURE 9.11 Comparison of the quartz and porcelain antennas' peak extractable current densities at different power levels in pulsed mode (p = 2.5 to 3 mTorr)

CHAPTER 10

SUMMARY

Multicusp ion sources are capable of producing ions with low axial energy spread, and therefore, are excellent candidates for applications such as ion projection lithography (IPL) and radioactive ion beam (RIB) production. Axial ion energy spread of the filament driven ion source has been reduced from approximately 6 eV to less than 2 eV by the use of a magnetic filter which controls the axial plasma potential distribution in the discharge region. Furthermore, it has been shown that energy spread less than 3 eV can be obtained for the rf-driven source with proper rf shielding.

Further reduction of the axial energy spread has been achieved in the new co-axial source. This source has been designed and constructed with a modified magnetic filter. Instead of a pair of magnets, a more complicated water-cooled filter cage (with 6 rows of permanent magnets) has been used. With this novel device, the axial energy spread has been reduced to a record low of 0.6 eV.

Plasma parameters inside the co-axial source have been measured. A Langmuir probe has been used to measure the plasma potential, the electron temperature and the density distribution. It has been found that the axial plasma potential distribution as well as the electron density in the discharge region for this source is quite uniform. Furthermore, the electron temperature in the extraction region of the source can be as low as 0.1 eV which adds a new dimension to the possible applications of the source. This electron temperature is lower than that of a tungsten cathode which normally operates at >3,000°C (~ 0.3 eV). The brightness of the electron beam can be improved if the electron

temperature is small. Thus, the co-axial source can also serve as a high brightness electron source for e-beam lithography. Instead of using thermal emission cathodes or laser induced photo-cathodes, high intensity electron beams can be extracted from the dense plasma inside the co-axial source.

A triode accelerator system has been designed and constructed in order to test the co-axial source's capability in improving the emittance. The radial plasma potential distribution can be adjusted by biasing the anode of the central region with respect to that of the annular region. The beam emittance is reduced when the plate is biased slightly positive ($\sim$1V).

Finally, the filter-equipped multicusp ion source (which has $\Delta E \sim$ 2eV) has been tested in an ion projection lithography system located at the Fraunhofer Institute in Berlin, Germany. The result showed that the projected image on the substrate is sharper than when a duoplasmatron source is used. Pattern feature size as small as 60 nm has been achieved. This result is a good indication of ion energy spread reduction. Improvements in pattern feature size are expected with the new co-axial source which is planned to be used for the next generation ion projection lithography system.

REFERENCE

[1]   Wolf, B. Handbook of Ion Sources, CRC Press; Boca Raton, Florida, 1995.

[2]   Leung, K.N., P. Herz, W.B. Kunkel, Y. Lee, L. Perkins, D. Pickard, M. Sarstedt, M. Weber, and M.D. Williams, *J. Vac. Sci. Technol.* **B13**(6), Nov/Dec 1995. 2600-2602

[3]   Finkelstein, W., and A. Mondelli, *Semiconductor International*, **6**, 107 (1995).

[4]   Mackenzie, G.H., M.Dombsky, W.R. Rawnsley, G. Stanford, Y. Yin, *Proc. of the 14th Int. Conf. on Cyclotron and its Apps.* (Oct. 8-13, 1995, Cape Town, South Africa).

[5]   Ueda, Y., T. Yoshikawa, Y. Ito, M. Nishikawa, and S. Goto, *Proc. of the 6th Int. Conf. on Ion Sources* (Sep. 10-16, 1995, Whistler, B.C., Canada).

[6]   Vilaithong, T., D. Boonyawan, W. Pairsuwan, S. Singkarat and D. Suwannakachorn, *12th Int. Conf. on the App. of Acc in Research & Industry*, (2-5 Nov., 1992, Denton, Texas)

[7]   Leung, K.N., Bachman, D.S., Herz, P.R., Kunkel, W.B., and McDonald, D.S., *Nucl. Instr. and Meth.* **B74** (1993) 291.

[8]   Lee, Y., Perkins, L.T., Gough, R.A., Hoffmann, M., Kunkel, W.B., Leung, K.N., Sarstedt, M., Vujic, J., Weber, M., Williams, M.D., *Nucl. Instr. and Meth. In Phys. Res. A* **374** (1996) 1-6.

[9]   Thompson, L.F., Willson, C.G., Bowden, M.J., Introduction to Microlithography, American Chemical Society, Washington, DC 1994.

[10]   Brown, W. L. *Microcir. Eng.* 1989, **9**, 269.

[11]   Bartelt, J. L., *Solid State Technol.* 1986, **29(5)**, 215.

[12]   Stengl, G.; Loschner, H.; Muray, J., *Solid State Technol.* 1986, **29(2)**, 119.

[13]   Mauger, E; Shimkunas, A.R.; Wolfe, J.C.: Sen, s.; Loschner, H.; Stengl, G., *J. Vac. Sci. Technol.* 1992, **B10(6)**, 2819.

[14]   Stengl, G.; Bosch, G.; Chalupka, A.; Fegerl, J.; Fischer, R.; Lammer, G.; Loschner, H.; Malek, L.; Nowak, R.; Traher, C.; Wolf, P.; Mauger, P.; Shimkunas, A.; Sen, S.; Wolfe, J.C., *J. Vac. Sci. Technol.* 1992, **B10(6)**, 2824.

[15]   Bruenger, W.H.; Buschbeck, H.; Cekan, E; Eder, S.; Fedynyshyn, T.H.; Hertlein, W.G.; Hudek, P.; Kostic, I; Loeschner, H.; Rangelow, I.W.; and Torkler, M., *Journal of Vac. Sci.* (soon to be published)

[16]   Prewett, P.D.; and Mair, G.L.R., Focused Ion Beams from Liquid Metal Ion Sources, John Wiley & Sons Inc., New York, 1991.

[17]   Forsterling, W.; Herrlander, C.J.; and Ryde, H., *Proceedings of the Lysekil Symposium,* 1966, session XII, Sweden (Almquist & Wiksell, Stockholm, 1967) p. 681.

[18]   Cheifetz, E.; et. al., *Phys. Rev. Lett.* **24**, 148 (1970)

[19]   Report on the science for an advanced ISOL facility, November 1997.

[20]   Nitschke, J.M., *Proceeding of the International School Seminar on Heavy Ion Physics*, May 10-15, 1993, Dubna, Russia.

[21]   Leung, K.N., D.S. Bachman, P.R. Herz, W.B. Kunkel, D.S. McDonald, *Nucl. Intrum. and Meth. in Phys. Research* **B74** (1993) 291-294.

[22]   Ueda, Y., Y. Sakashita, T. Yoshikawa, M. Isobe, M. Nishikawa, and S. Goto, *Rev. Sci. Instrum.* **65**(8), August 1994.

[23]   Ehlers, K.W., K.N. Leung, P.A. Pincosy, and M.C. Vella, *Appl. Phys. Lett.*, **41**, 517 (1982)

[24]   Huddlestone, R.H., S.L. Leonard, *Plasma Diagnostic Techniques*, Plasma Research Laboratory, Los Angeles, 1968.

[25]   Y. Lee, R.A. Gough, W.B. Kunkel, K.N. Leung, L.T. Perkins, D.S. Pickard, L. Sun, J. Vujic, M.D. Williams, D. Wutte, A.A. Mondelli, G. Stengl, *Nucl. Instr. and Meth. In Phys. Res. A* **385** (1997) 204-208

[26]   Leung, K.N., S.R. Walther, and W.B. Kunkel, Phys. Rev. Lett. **62**(7), 764 (1989).

[27]   Brown, I.G., The Physics and Technology of Ion Sources, John Wiley & Sons, INC, New York, 1989.

[28]   J. W. Staples, M.D. Hoff, Chun Fai Chan, *Proceeding of the XVIII International Linear Accelerator Conference*, Geneva, Switzerland, 26-30 August 1996, vol. 1, p 157-9.

[29]   Sarstedt, M, Y. Lee, K.N. Leung, L.T. Perkins, D.S. Pickard, M. Weber, M.D. Williams, *6th Int. Conf. On Ion Sources* (10 - 16 September 1995, Whistler, BC, Canada)

[30]   Y. Lee, R.A. Gough, W.B. Kunkel, K.N. Leung, L.T. Perkins, D.S. Pickard, L. Sun, J. Vujic, M.D. Williams, D. Wutte, A.A. Mondelli, G. Stengl, *Nucl. Instr. and Meth. In Phys. Res. A* **385** (1997) 204-208

[31]   S.G. Zakhary, *Rev. Sci. Instrum.*, **66** (12), Dec. 1995, p. 5419.

[32]   J.K. Olthoff, R.J. Van Brunt, and S.B. Radovanov, **67** (4), July 1995, p. 473.

[33]   Y. Lee, R.A. Gough, W.B. Kunkel, K.N. Leung, L.T. Perkins, D.S. Pickard, L. Sun, J. Vujic, M.D. Williams, D. Wutte, *Rev. Sci. Instrum.* **68**(3), March 1997 1398-1402

[34]   Lee, Y.; Gough, R.A.; Kunkel, W.B.; Leung, K.N.; Perkins, L.T.; Pickard, D.S.; Sun, L; Vujic, J; Williams, M.D; Wutte, D; *Nucl. Instr. and Meth. In Phys. Res. B* **119** (1996) 543 - 548.

[35]   M.D. Williams and K.N. Leung, *Rev. Sci. Instrum,* **61**, 475 (1990).

[36]   K.N. Leung, S.R. Walther, and W.B. Kunkel, *Phys. Rev. Lett.,* **62,** 764 (1989).

[37]   W.S. Cooper, K. Halbach, and S.B. Magyary, in *Proceedings of the 2nd Symposium on Ion Sources and Formation of Ion Beams,* Berkeley, October, 1974 (unpublished).

[38]   P. Allison, J.D. Sherman, and H.V. Smith, Report LA-8808-MS, Los Alamos Nat. Lab., 1981.

[39]   P.W. Allison, J.D. Sherman, and D.B. Holtkamp, *IEEE Trans. Nucl. Sci.* **NS-30,** 2204 (1983).

[40]   M. Sarstedt, Y. Lee, K.N. Leung, L.T. Perkins, D.S. Pickard, M. Weber, and M.D. Williams, *Rev. Sci. Instrum.,* **Vol. 67,** No. 3, March 1996, 1246.

[41]   K.W. Ehlers, K.N. Leung, P.A. Pincosy, M.C. Vella, *Appl. Phys. Lett.* **41** (1982) 517.

[42]   P.D. Prewett and G.L.R. Mair, <u>Focused Ion Beams from Liquid Metal Ion Sources,</u> Research Studies Press LTD., Taunton, Somerset, England, 1991, p. 169.

[43]   Lee, Y.; Gough, R.A.; Kunkel, W.B.; Leung, K.N.; Vujic, J; Williams, M.D; Wutte

D; and Yang, F.L.; (Presented to MNE '97, September), *Microelectronic*

Engineering, **41/42** (1998), 241-244.

[44]   S. T. Melnychuk, T.W. Debiak, and J.J. Sredniawski, *Rev. Sci. Instrum.* **67** (3),

March 1996.

[45]   D. Wutte, private communications.

[46]   Y. Lee, R.A. Gough, K.N. Leung, L.T. Perkins, D.S. Pickard, J. Vujic, L.K. Wu,

M. Olivo and H. Einenkel, *Rev. of Sci. Inst.,* **69** (2), February 1998, 1023 - 1025.